Aspects of Source-Term Modeling for Vortex-Generator Induced Flows

Florentie, Liesbeth

DOI
10.4233/uuid:704d764a-6803-4cad-991f-45dc4ea38f6d

Publication date
2018

Document Version
Final published version

Citation (APA)
Florentie, L. (2018). *Aspects of Source-Term Modeling for Vortex-Generator Induced Flows*. [Dissertation (TU Delft), Delft University of Technology]. https://doi.org/10.4233/uuid:704d764a-6803-4cad-991f-45dc4ea38f6d

ASPECTS OF SOURCE-TERM MODELING FOR VORTEX-GENERATOR INDUCED FLOWS

ASPECTS OF SOURCE-TERM MODELING FOR VORTEX-GENERATOR INDUCED FLOWS

Dissertation

for the purpose of obtaining the degree of doctor
at Delft University of Technology,
by the authority of the Rector Magnificus prof. dr. ir. T.H.J.J. van der Hagen,
chair of the Board for Doctorates,
to be defended publicly on
Wednesday 4 April 2018 at 12:30 o'clock

by

Liesbeth FLORENTIE

Master of Science in Aerospace Engineering,
Delft University of Technology, the Netherlands
born in Bonheiden, Belgium.

This dissertation has been approved by the promotors.

Composition of the doctoral committee:

Rector Magnificus,	chairperson
Prof. dr. ir. drs. H. Bijl,	Delft University of Technology, promotor
Dr. S.J. Hulshoff,	Delft University of Technology, copromotor
Dr. ir. A.H. van Zuijlen,	Delft University of Technology
Independent members:	
Prof. dr. S. Hickel,	Delft University of Technology
Prof. dr. C.B. Allen,	University of Bristol
Prof. dr. A.V. Johansson,	KTH Royal Institute of Technology
Prof. dr. N.N. Sørensen,	Technical University of Denmark
Prof. dr. F. Scarano,	Delft University of Technology, reserve member

This work has received funding from the European Union's Seventh Programme for research, technological development and demonstration under grant agreement No FP7-ENERGY-2013-1/no. 608396 Advanced Aerodynamic Tools for Large Rotors (AVATAR).

Front & Back: Simulation result which shows the vortex created by a vortex generator in a wall-bounded flow.

ISBN 978-94-6186-918-0

An electronic version of this dissertation is available at
http://repository.tudelft.nl/.

SUMMARY

Vortex generators (VGs) are a widespread means of passive flow control, capable of yielding significant performance improvements to lift-generating surfaces (e.g. wind-turbine blades and airplane wings), by delaying boundary-layer separation. These small vane-type structures, which are typically arranged in arrays, trigger the formation of small vortices in the boundary layer. The flow circulation induced by these vortices causes the near-wall flow to be re-energized, thereby reducing the susceptibility of the boundary layer to separate from the surface.

Predictions of the effect of a VG configuration on a flow are challenging, due to the small scale of VGs in combination with the complexity of the generated flow patterns and interactions. Partly-modeled/partly-resolved VG models trigger the formation of a suitable vortex in the flow by local addition of a source term to the governing equations. This type of models is considered a good trade-off between computational effort and accuracy. Such models do not account for the smallest-scale flow features induced by the presence of a VG, but the creation and propagation of the main vortex are resolved.

The goal of this thesis consisted of enhancing insight into the use and effectiveness of such source-term models for simulating VG effects in CFD codes. To this end this study focused in the first instance on the current industrial standard in this respect, being the BAY and jBAY models. The scope of the analysis was limited to steady RANS simulations of incompressible wall-bounded flows, using the boundary-layer's shape factor as primary quantity of interest. Body-fitted mesh (BFM) simulations were used as reference in order to isolate (as much as possible) the VG modeling error from the RANS errors.

Both the BAY and the jBAY model were implemented in the open-source CFD code OpenFOAM®, including several options to define the domain in which to apply the source term. The influence of the source-term domain Ω_{VG} was analyzed for different test cases, involving isolated VGs and VG arrays on both flat-plate and airfoil surfaces. Our analysis revealed that the results obtained with the BAY model depend strongly on the choice for Ω_{VG}, and that calibration is therefore essential in order to obtain a reasonably accurate flow field with a realistic amount of VG-induced circulation. In the absence of calibration data, the cell-selection approach proposed for the jBAY model, which consists of a region aligned with the actual VG orientation and a width of 2 cells in crossflow direction, was found to yield the best calibrated flow field.

Moreover, the effect of mesh refinement on the created flow field was studied by considering both flat-plate and airfoil simulations using 3 different mesh resolutions. The results of this study indicated the presence of a model error for the BAY and the jBAY model, in the sense that they both create erroneous shape-factor profiles and that they consistently under-predict the vortex strength, upon comparison with BFM simulations. Although the jBAY model is typically expected to show reduced mesh dependence compared to the BAY model (due to the involved interpolation and redistribution formulations), this was not observed in our results. Simulations with the BAY and jBAY mod-

els applied for the same Ω_{VG} showed that the effect of the differences in formulation between both models is limited, and mainly manifests as a small decrease in vorticity levels.

Subsequently, the impact of different aspects of the source-term field, that is added to the governing equations to represent the effect of VGs on the flow, was assessed by formulating several modified source-term formulations. Comparison of uniform and non-uniform source-term distributions, whether or not calibrated in magnitude and/or direction with respect to the corresponding VG surface force as obtained from a BFM simulation, allowed assessment of the source-term's distribution, magnitude and direction. This analysis revealed that the distribution of the source term over Ω_{VG} seems to have a lesser influence on the characteristics of the created vortex, and that the resultant source-term forcing dominates both the strength and shape of the created vortex. It was found that the magnitude of the resultant forcing is the main driver in this respect, as it directly governs the energy that is added to the system. Small variations in the direction of the imposed forcing were found to have only a limited effect on the created flow field.

The above mentioned analyses were mostly performed on high-resolution meshes. However, practical application of source-term VG models requires the use of coarse meshes. To answer the question whether it is possible to achieve sufficiently accurate flow fields when using a source-term model on a coarse mesh, an optimization framework was formulated. This framework allows calculation of the optimal source term for a given mesh, as well as the achievable accuracy. The goal functional was defined as the l^2-norm of the deviation between the velocity field obtained with a source-term simulation and a high-fidelity reference solution (in this case the projection of a BFM simulation result onto the coarse mesh of interest). By making use of the Lagrange-multiplier method a set of continuous adjoint equations was formulated which allows the direct calculation of the gradient of the goal functional with respect to the source-term distribution.

The obtained goal-functional gradient was successfully used in a trust-region optimization method to calculate the optimal source term for both an isolated VG and a VG array on flat-plate surfaces. Simulations were performed for different mesh resolutions and different source-term regions, where Ω_{VG} was either defined as a small region covering the physical VG location, or as a larger rectangular domain. It was found that with an optimized source term significantly more accurate flow-field results are possible, characterized by a decrease in goal functional of almost one order of magnitude, compared to the jBAY model. Even on very coarse meshes and for small Ω_{VG}, a source term could be obtained that yields excellent shape-factor profiles already closely downstream of the VG location. Inspection of the obtained optimized source terms revealed that a close resemblance with the actual VG reaction force on the flow does not necessarily yield the best flow-field result.

The concept of replacing a physical VG by a local source term, without mesh adaptations, was thus proven viable, thereby justifying continued research towards the improvement of current source-term VG models. The developed source-term optimization framework can serve as a useful tool in this endeavor.

SAMENVATTING

Wervel generatoren (VGs) zijn een wijd gebruikt middel voor passieve controle van stromingen. Het gebruik van VGs kan leiden tot aanzienlijke prestatieverbeteringen voor liftkracht-opwekkende oppervlakken (zoals bijvoorbeeld windturbinebladen en vliegtuigvleugels) door het uitstellen van loslating van de grenslaag. Deze kleine opstaande objecten, welke typisch met meerdere bij elkaar geplaatst worden, veroorzaken de vorming van kleine wervels in de grenslaag. De hierdoor ontstane stromingscirculatie zorgt ervoor dat het energieniveau dicht bij het oppervlak toeneemt, waardoor de gevoeligheid van de grenslaag voor loslating afneemt.

Door de kleine schaal van deze VGs, in combinatie met de complexe stromingsvormen en interacties, is het een uitdaging om het effect van een bepaalde VG configuratie op de stroming correct te voorspellen. Modellen die de vorming van een wervel in de grenslaag nabootsen door lokale toevoeging van een bronterm aan de stromingsvergelijkingen, en daarbij de wervel gedeeltelijk modeleren en gedeeltelijk oplossen, worden beschouwd als een goed compromis tussen benodigde rekenkracht en nauwkeurigheid. Deze modellen houden geen rekening met de kleinste schalen in de stroming die veroorzaakt worden door de aanwezigheid van de VG, maar lossen wel de vorming en evolutie van de hoofdwervel op.

In dit proefschrift worden het gebruik en de effectiviteit van dit soort brontermmodellen voor de simulatie van de effecten van VGs in numerieke stromingsleer (CFD) codes onderzocht. De focus ligt in eerste instantie op de huidige standaard, namelijk de BAY en jBAY modellen. De gepresenteerde analyse is beperkt tot RANS simulaties van onsamendrukbare stromingen over een oppervlak, waarbij de vormfactor van de grenslaag geldt als belangrijkste parameter. Simulaties met een aansluitend rekenrooster (BFM), welke de stroming om de VG volledig oplossen, zijn gebruikt als referentie om de fout door het gebruik van een VG brontermmodel te kunnen isoleren van de RANS fout.

Zowel het BAY als het jBAY model zijn geïmplementeerd in de CFD code OpenFOAM®, in combinatie met verschillende opties om het domein van de bronterm te bepalen. De invloed van dit domein Ω_{VG} is bestudeerd voor verschillende proefproblemen, waaronder een enkele VG en VG configuraties op zowel een vlakke plaat als een vleugelprofiel. Uit deze analyse volgt dat de resultaten die verkregen zijn met het BAY model sterk afhankelijk zijn van de keuze voor Ω_{VG}, en dat kalibratie daarom essentieel is voor het verkrijgen van een redelijk nauwkeurige stroming met een realistische hoeveelheid circulatie (opgewekt door de VG). Als geschikte kalibratiedata ontbreekt, lijkt gebruik van een domein zoals voorgesteld in het jBAY model (bestaande uit een regio in de richting van de VG van 2 cellen breed) tot het beste resultaat te leiden.

Het effect van roosterverfijning op de gecreëerde stroming is onderzocht door zowel de vlakke plaat als vleugelprofiel problemen te simuleren met 3 verschillende resoluties. De resultaten van deze studie duiden op de aanwezigheid van een modelfout in

zowel het BAY als het jBAY model, in die zin dat ze beiden tot foutieve vormfactoren leiden en de intensiteit van de gecreëerde wervel onderschatten (in vergelijking met de BFM simulaties). Van het jBAY model wordt over het algemeen een verminderde roosterafhankelijkheid verwacht in vergelijking met het BAY model (door de interpolatie en herverdeling van parameters tijdens de berekening). Dit is echter niet waargenomen in de resultaten. Simulaties met beide modellen voor hetzelfde domein Ω_{VG} tonen aan dat het effect van dit verschil in formulering minimaal is, en voornamelijk bestaat uit een kleine afname van de vorticiteit.

Om de invloed van verschillende aspecten van de bronterm op de stroming te onderzoeken zijn enkele alternatieve brontermen geformuleerd. Het effect van de brontermverdeling, -grootte en -richting is bestudeerd door resultaten te vergelijken welke verkregen zijn met zowel uniforme als niet-uniforme brontermen, al dan niet gekalibreerd voor grootte en/of richting aan de hand van BFM simulaties (waaruit de reactiekracht van de VG op de stroming afgeleid is). Hieruit volgt dat de verdeling van de bronterm over Ω_{VG} minder bepalend is dan de totaal toegevoegde brontermkracht. Deze laatste domineert zowel de intensiteit als de vorm van de ontstane wervel. De grootte van deze brontermkracht is de belangrijkste factor in dit opzicht, aangezien deze rechtstreeks de energie beïnvloed die wordt toegevoegd aan het systeem. Kleine variaties in de richting van de brontermkracht hebben slechts een miniem effect op de resulterende stroming.

Voor bovenstaande analyses is voornamelijk gebruik gemaakt van een rekenrooster met hoge resolutie. Praktische toepassingen van VG brontermmodellen vereisen echter typisch het gebruik van roosters met een lage resolutie. Om te onderzoeken of het mogelijk is om voldoende nauwkeurige resultaten te verkrijgen wanneer een brontermmodel gebruikt wordt op een grof rooster, is daarom een optimalisatiekader ontwikkeld. Met deze methode is het mogelijk om de optimale bronterm te berekenen voor een bepaald (grof) rooster, evenals de hoogst haalbare nauwkeurigheid. De doelfunctionaal voor deze optimalisatie is gedefinieerd als de l^2-norm van de afwijking in snelheidsveld tussen de brontermsimulatie en een referentieoplossing (in dit geval de projectie van een BFM resultaat op het grof rooster). Door middel van de Lagrangevermenigvuldigingsmethode is een stelsel van continue adjoint vergelijkingen afgeleid, welke de directe berekening van de gradiënt van de doelfunctionaal met betrekking tot de bronterm mogelijk maakt.

De op deze manier verkregen gradiënt is succesvol gebruikt in combinatie met een 'trust-region' methode om de optimale bronterm te berekenen voor zowel een enkele VG als voor een VG configuratie op een vlakke plaat. Deze simulaties zijn uitgevoerd voor verschillende resoluties en brontermdomeinen, waarbij Ω_{VG} gedefinieerd is als ofwel een smal domein in de richting van de VG, of als een groter rechthoekig domein. De verkregen resultaten tonen aan dat het gebruik van een geoptimaliseerde bronterm kan leiden tot een aanzienlijk nauwkeuriger stromingsresultaat (gekenmerkt door een afname in de doelfunctionaal van bijna een ordegrootte), in vergelijking met het jBAY model. Zelfs op een zeer grof rooster en voor kleine Ω_{VG} is een bronterm verkregen welke tot uitstekende vormfactorprofielen leidt op korte afstand stroomafwaarts van de VG. Hieruit volgt dat een goede benadering van de daadwerkelijke reactiekrachtverdeling van de VG op de stroming niet per se leidt tot het meest nauwkeurige resultaat.

Het concept om een VG te vervangen door een lokale bronterm, zonder roosterwij-

zigingen t.o.v. de situatie zonder VG, is dus bewezen, en voortgezet onderzoek naar een verbetering van bestaande VG brontermmodellen is hierom gewenst. Het in dit werk ontwikkelde optimalisatiekader kan hierbij dienen als een nuttig hulpmiddel.

CONTENTS

1

INTRODUCTION

1.1. MOTIVATION

Engineers actively aim to manipulate flows in such a way as to yield maximum benefits. Be it the lift force generated over aircraft wings, the energy conversion in a gas turbine, or the power extracted by a wind turbine, performance largely depends on the specific characteristics of the flows involved. Prandtl's famous notion that the effects of friction are only experienced very near an object moving through a fluid, thereby introducing the concept of a boundary layer, has proven key to many developments in this area.

One of the most simple, yet effective, means to influence a local flow field consists of the use of passive vortex generators (VGs). These are small vane-type obstacles that can be mounted on a lift-generating surface, like an airplane wing. Because the fluid (air, in the case of an airplane) now has to flow around this obstacle, a vortex is created close to the surface. Due to the swirling motion of this vortex, the fluid particles in the boundary layer behind the VG are mixed in such a way that energy is added to the region closest to the surface. This has several potential benefits, one of them being that the susceptibility of the boundary layer to separate from the surface is reduced. By ensuring an attached flow over a larger region of the lift-generating surface, the addition of VG arrays has the ability to improve the design's overall performance.

To illustrate the impact of this effect, let us consider the case of a wind turbine. For maximal power output reduction of flow separation is essential, as those parts of the blade where the flow is separated from the surface adversely affect the power generation. In 1996 the NREL research institute performed a full-scale test in order to investigate the effectiveness of VGs in this respect [32]. It was found that an array of VGs, distributed along the root section of the blades (using a configuration similar as illustrated in figures 1.1 and 1.2), effectively increased the power output at moderate wind speeds with almost 5%. However, the experiment also revealed that the presence of the VGs caused drag penalties, resulting in a loss in power output at low wind speeds.

From this example, it becomes clear that for the flow alteration to have an overall beneficial effect, appropriate design and positioning of the VGs is crucial. Therefore it is

important to have a good understanding of how the addition of VGs influences the flow. Depending on the external conditions (for a wind turbine, this can be the wind speed or the blade pitch angle, for example) a certain VG shape and position can be beneficial in one case, but disadvantageous in another. Simulation tools that allow this effect to be studied for different configurations are therefore indispensable when creating effective designs that include VGs. However, making reliable performance predictions for objects equipped with this type of flow-control device is not straightforward, as it requires the ability to predict the effects of detailed flow patterns induced by individual VGs, as well as the combined effects produced by VG arrays.

Computational fluid dynamics (CFD) simulations can be extremely helpful in this context. Typically these require the construction of a numerical mesh, consisting of cells with a resolution determined by the fluid motion to be studied. To resolve the flow over small objects like a VG, the use of very fine meshes is required. However, the overall structure of interest is typically of a much larger scale. This combination of scales imposes an excessive computational cost, both with respect to the overall number of cells required and the complexity related to the generation of a good quality mesh. This usually precludes the direct inclusion of small objects like VGs into numerical meshes used for design purposes, which prevents the accurate simulation of VG induced flows.

A possible solution to this problem consists of not actually including the VG geometry into the simulation, but rather replacing the VG by a model which mimics its effect on the flow. This might be done, for example, by the addition of a source term to the governing equations. Hence, with respect to the situation without VGs, the equations governing the flow are thus adapted in an attempt to obtain the same effect obtained when including the VG structure into the numerical mesh. Ideally, this would allow the flow to be simulated at levels of mesh refinement set only by the larger scales of interest, resulting in large savings in computational cost. Of course, the formulation of the modified flow equations for this purpose is far from trivial. Several approaches have been proposed in literature, an overview of which is included in chapter 3. Of these, the BAY model [11] and its successor the jBAY model [41] are the most commonly used. Both models locally add a source term to the governing equations which is based on an estimation of the

Figure 1.1: Installation of vortex generators on a wind turbine (©Robert Bergqvist)

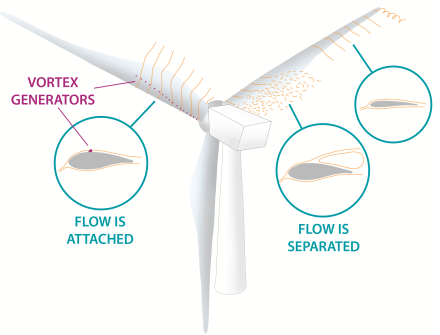

Figure 1.2: Vortex generators can prevent flow separation on wind turbine blades.

fluid force acting on the VG surface.

Despite their widespread use, many essential questions related to the accuracy of the BAY and jBAY model still remain unanswered. These include the required mesh resolution, and the range of reliable operating conditions. For example, it has been observed that for airfoil angles of attack close to the stall point, both the BAY and jBAY models are unreliable in their prediction of the effects of VGs on the generated aerodynamic forces [8]. This of course undermines the trustworthiness of the obtained results, and hence the effectiveness of new VG configuration designs. A better understanding of the principles governing the results obtained with such source-term models is therefore a prerequisite for their further use. Only when reliable simulation results, and knowledge of their limitations, are available, can the addition of VGs be expected to yield large efficiency gains.

1.2. OBJECTIVE

Considering the widespread use of VGs, and of source-term models like the BAY model to simulate their effect, an urgent need exists for a better understanding of the use of VG models in CFD simulations. This dissertation therefore aims to unravel some of these mysteries, by exploring both the strengths and limitations of existing source-term VG models, and the effects of general source term characteristics. For this study we limit our scope to incompressible wall-bounded flows, representative of, for example, wind-turbine applications. The central research question of this work can be formulated as:

> *How do source-term model formulation and simulation parameters affect the accuracy of the vortex generator induced flow field obtained when performing CFD simulations of incompressible wall-bounded flows?*

To answer this question, it is first of all important to identify the essential flow quantities when studying the effects of a VG on a boundary layer. A question which then immediately arises is to what level of accuracy these quantities should be reproducible by a source term model for the solution to be reliable. The answer to this question allows assessment of the performance of current source-term models, for example, by evaluating how well the BAY and jBAY model predict these key quantities.

Moreover, in order to allow for the formulation of improved source-term VG models, a fundamental insight into how specific parameters influence the created flow field is vital. Therefore the current research also investigates the general potential of source-term models in this respect. For simulations constrained to suboptimal meshes, the question arises what is the highest accuracy one can expect to achieve when making use of a source term to reproduce VG induced flow effects. In this work, an inverse approach is considered in order to identify those source-term formulations. By starting from a reference high-fidelity flow field, the source term that allows this flow field to be mimicked most effectively is calculated and studied.

The created body of knowledge presented in this dissertation consists of a synthesis of information related to the use of source-term models for simulating VG effects on wall-bounded flows, and serves as a useful addition to the insights already present in literature. The new approach taken here towards perturbing current source-term models and optimizing their formulation will hopefully serve as an inspiration towards improved VG models for CFD simulations.

1

1.3. OUTLINE

This dissertation begins by revising some fundamental concepts related to wall-bounded flows and boundary-layer separation. This can be found in chapter 2, which also provides an overview of VG working principles and configurations. An overview of the current state of the art with respect to the simulation of VG-induced flow fields is contained in chapter 3.

Chapter 4 then continues by laying out the scope of the research, including the definition of quantities of interest and the approaches taken to answer the central research question. Furthermore, chapter 4 also contains an overview of the test cases that are considered in this study.

Chapter 5 is concerned with the analysis of the BAY and jBAY models. In particular, the effects of mesh resolution and the region where the model is applied are given attention. In order to obtain a better understanding of the factors that influence the results obtained, chapter 6 elaborates on the importance of several source-term parameters, including the distribution, total magnitude and direction.

After that, a novel inverse framework, based on a continuous adjoint method, that allows the calculation of "optimal" source terms is presented in chapter 7. This includes both derivation and implementation details. A discussion of the obtained results for our test problems, and comparison with current VG models, follows in chapter 8.

Finally, chapter 9 presents the findings of this research, focusing on the various aspects of source-term VG models and how they influence the obtained flow field. The key parameters arising from the current work are identified, resulting in recommendations for further research towards the development of improved VG models.

2

VORTEX GENERATOR INDUCED FLOWS: BACKGROUND

This chapter provides some essential background information for the remainder of this dissertation. It starts by an historical overview, in which fundamental concepts related to the description and analysis of fluid flows are revised. This is followed in section 2.2 by a description of boundary-layer separation for wall-bounded flows. Afterwards, in section 2.3, the concept of flow control is introduced. Here, special attention is given to vortex generators, including an overview of common configurations and the related physical principles.

2.1. A BRIEF HISTORY OF FLUID FLOW ANALYSIS

Long before the first scientific theories of fluid flows, people have striven to use the power of fluids to their advantage. Examples date back to ancient civilizations, using the wind as power source for sailing ships. Mentions of wind-powered machines start around the first century, evolving to widespread use of windmills in the early middle ages, when they were primarily used for pumping water or for milling purposes. Efforts to understand the main fluid-dynamic principles were however limited, the only contributions of impact being due to two Greek philosophers. Around the 4^{th} century B.C., Aristotle introduced the concept of a continuum, and even an initial notion of fluid dynamic drag. These important ideas were soon followed by Archimedes' reflections on the pressure in a fluid.

It took several centuries before these fundamental initial thoughts were further developed. During the Renaissance, the rapid rise in importance of naval architecture triggered a renewed interest in fluid dynamics. In order to design more efficient ships, it became clear that a better understanding of the principles governing fluid flows and power generation was indispensable. An important contribution was made by Leonardo Da Vinci in the 15^{th} century, who studied the basic characteristics of fluid flow by means of several experiments. His endeavors led to the important principle of conservation

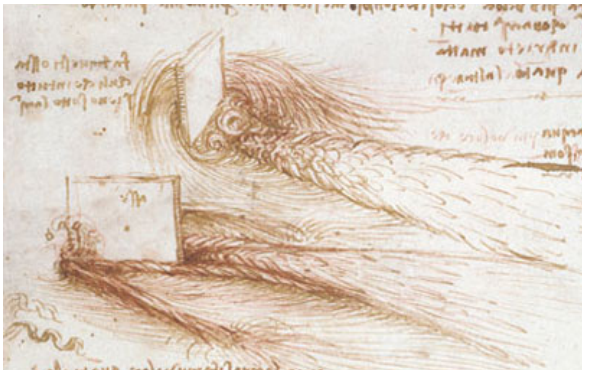

Figure 2.1: Sketch from Leonardo Da Vinci depicting the (water) flow around flat plates, showing the created pair of counter-rotating vortices.

of mass for the specific situation of low speed flows. This principle, in its later developed general form, evolved to become one of the most fundamental equations of fluid dynamic theory. Furthermore, Leonardo Da Vinci pioneered the field of flow visualization with his many sketches. Apart from his famous ideas about the eddying motions of water, thereby introducing the concept of turbulence, this also resulted in the first reference to the importance of vortices in fluid motion. In his study about the flow of water around a flat plate, shown in figure 2.1, Da Vinci accurately described the observed fluid-dynamical phenomena, including the region with recirculating, separated flow at the back of the plate and the creation of an extensive wake trailing downstream. Note that this flow field bears a large resemblance with the flow fields typically observed in the study of vortex generators.

In the years following Leonardo da Vinci's work, several advancements in the study of fluid dynamics were made. Probably the biggest leap forward is attributable to Isaac Newton, who developed a mathematical foundation for the study of mechanics in his famous work *Principia*. Moreover, the importance of his laws of motion and law of viscosity, the latter holding true for gases and water in ordinary situations, cannot be overstated. Newton's work marked the starting point for rapid advancements in the pursuit of a scientific theory for fluid flows. One of the contributors to this theory was Daniel Bernoulli, who was the first to examine the relation between pressure and velocity in a fluid flow. Although not stated as such by himself, his work eventually resulted in the famous Bernoulli equation which allows changes in pressure and velocity to be quantified for inviscid, incompressible flow. It was Leonhard Euler who actually formulated the aforementioned equation, based on Bernoulli's observations. Euler's biggest contribution to fluid-dynamic theory, however, probably consists of the mathematical formulation of the governing equations for general inviscid flow in the mid-18^{th} century. The significance of this work is immense, as it opened to door for quantitative analyses of fluid flows where the effects of friction can be ignored. Today, the Euler equations are still used for a large number of aerodynamic analyses.

However, the inviscid assumption is insufficient in many areas, as in practice the effects of friction are often too big to be neglected. D'Alembert's paradox forms a nice

illustration of this. Upon calculation of the flow over a closed 2D body using the above inviscid, incompressible theory, d'Alembert obtained the result of zero drag. This is obviously incorrect, and thus highlights the importance of including friction in the governing fluid-flow equations. At the time, the phenomenon of friction was already appreciated by scientists, but it was not sufficiently understood to be included in theoretical analysis.

This changed in the 19$^{\text{th}}$ century, when both Louis Navier (with an important contribution of Jean-Claude Barré de Saint-Venant) and George Stokes independently succeeded in incorporating the internal shear stresses into the description of fluids. In doing so, they managed to derive the governing equations for viscous flow, known widely as the Navier-Stokes equations. The importance of these equations cannot be overstated: they provide an excellent description of a wide variety of fluid flows, and belong to the most fundamental fluid-dynamic equations to date. The Navier-Stokes equations account for conservation of mass and momentum and can be formulated in conservative form as

$$\frac{\partial(\rho\mathbf{u})}{\partial t} + \nabla\cdot(\rho\mathbf{u}) = 0 \tag{2.1}$$

$$\frac{\partial(\rho\mathbf{u})}{\partial t} + \nabla\cdot(\rho\mathbf{u}\mathbf{u}) = -\nabla p + \rho\mathbf{f} + \nabla\cdot\boldsymbol{\tau} \tag{2.2}$$

where $\mathbf{u}$, p and ρ represent the primary flow variables, being the (vector) velocity, (scalar) pressure and (scalar) density fields respectively. Viscous effects are included through the stress tensor $\boldsymbol{\tau}$, whose formulation depends on the type of fluid considered, and $\mathbf{f}$ accounts for external accelerations due to for example gravity. Note that in order to account for compressible (high-speed) flows, the above set of equations needs to be extended with the later formulated energy equation, which is essentially the first law of thermodynamics.

Despite the fact that the Navier-Stokes equations were formulated more than a century ago, to date it still remains a challenge to analyze and solve them for arbitrary flows. The nonlinear, coupled, elliptic nature of these partial differential equations does not lend to a general analytical solution. In order to obtain solutions for specific situations, the above equations are therefore often simplified, for example based on particular geometric properties or by assuming some terms to be negligible. For some rare and very specific cases exact analytical solutions can be obtained. In general though, engineers rely on numerical methods to obtain solutions of the Navier-Stokes equations for practical situations of interest. In spite of the rapid rise in computing power, which excessed over the last few decades, obtaining numerical solutions for (2.1) and (2.2) remains a demanding task. Luckily, the burden can often be eased by making use of Prandtl's famous boundary-layer concept, which revolutionized the analysis of viscous flows and is the topic of the next section.

In addition to this very brief overview, more information about the historic evolution of fluid dynamic research can be found in [3], and the first chapter of [44]. For a more in-depth discussion of the fundamental theory of fluid dynamics, the reader is referred to [4] and [44].

2.2. ON THE BOUNDARY LAYER AND FLOW SEPARATION

In 1904, the field of computational fluid dynamics (CFD) was not yet established and therefore engineers lacked the tools to solve the Navier-Stokes equations for practical flow problems. This was a frustrating problem, especially since at that time the first airplanes were being built, of which the lift and drag can be greatly affected by unforeseen flow situations, for example separation. The concepts introduced by Prandtl in that year therefore were indispensable for future developments. On a conference in Heidelberg, Ludwig Prandtl was the first to discuss both the boundary layer around a solid body, and the mechanics governing the phenomenon of flow separation [43, 81].

As defined in [4], "the boundary layer is the region of flow adjacent to a surface, where the flow is retarded by the influence of friction between a solid surface and the fluid". This essentially implies that viscous effects are contained within this layer, and that friction can be neglected outside this region, where the assumption of inviscid flow is therefore justified. Moreover, Prandtl realized that within the boundary layer and for a sufficiently high Reynolds number, the governing equations can be simplified to the so-called boundary-layer equations, which are parabolic of nature and therefore much easier to solve. His pioneering work therefore allowed for reliable, quantitative fluid flow analyses.

The Reynolds number mentioned above is a dimensionless number which represents the ratio between the characteristic inertial (ρU_∞^2) and viscous ($\mu U_\infty / L$) stresses, given by

$$Re = \frac{\rho U_\infty L}{\mu}, \tag{2.3}$$

where L represents some characteristic length scale and μ is the dynamic viscosity. For high Re the viscous effects are relatively limited, yielding a thin boundary layer. As Re decreases, the viscous effects become relatively large and therefore the thickness of the boundary layer increases. Moreover, when Re is small (for example for low-speed flows or fluids with a high viscosity), the large viscous effects cause instabilities to be effectively suppressed, such that the streamlines remain aligned and smooth. Hence, laminar flows are characterized by low Re. On the other hand, a high Re typically indicates turbulent flow as these instabilities can no longer be suppressed.

A boundary layer arises in viscous wall-bounded flows, as in such cases friction causes the flow immediately at the surface to stick to the surface such that the local flow velocity needs to be zero. This is the so-called no-slip condition. When moving away from the surface, the local flow velocity gradually increases until at a certain point it (almost) equals the freestream velocity U_∞. This point marks the edge of the boundary layer, and the distance from the surface at which this happens is called the (velocity) boundary-layer thickness, denoted as δ. When the flow moves over a surface, more and more of the flow is affected by friction and therefore δ increases.

The gradual increase in velocity when moving from the surface towards the edge of the boundary layer defines the boundary-layer's velocity profile, an illustration of which is shown on the left in figure 2.2. In some situations, for example on the suction (upper) side of an airfoil at a positive angle of attack, the pressure in the boundary layer increases as the flow moves along the surface, thereby creating a so-called adverse pressure gradient ($\partial p / \partial x > 0$). This situation is called adverse, because the flow has to overcome an

increasingly strong opposing pressure force, which tends to retard the flow. The velocity profile therefore becomes thinner, as shown by profile (b) in figure 2.2. However, a thin velocity profile (characterized by a low velocity and therefore low kinetic energy) has a further reduced ability to withstand the adverse pressure gradient, such that eventually the direction of the flow close to the surface will reverse. At the point where this happens (point (c) in figure 2.2) a region of reversed flow is thus created close to the surface, and the boundary layer is said to be separated.

Note that fluid flows characterized by a high Re are typically less prone to flow separation, because the limited viscous effects allow for a rapid increase in flow velocity when moving away from the wall. Such flows therefore have a fuller velocity profile, containing more kinetic energy, than flows with a low Re. This enables them to withstand stronger adverse pressure gradients such that flow separation only occurs in more extreme situations.

Instead of an attached boundary layer, beyond the point of separation a wake is formed above the surface. This region of recirculating flow (shown in figure 2.3) drastically reduces the aerodynamic lift forces, whereas at the same time the (pressure) drag increases. For most applications, including airplane wings and wind-turbine blades, this is an undesired situation which greatly reduces the intended performance. For example, current wind turbines typically exhibit thick airfoils near the root section of the blade in order to ensure structural stability. However, due to the strong curvature of the local airfoil, a strong adverse pressure gradient arises in that area, giving rise to a large region

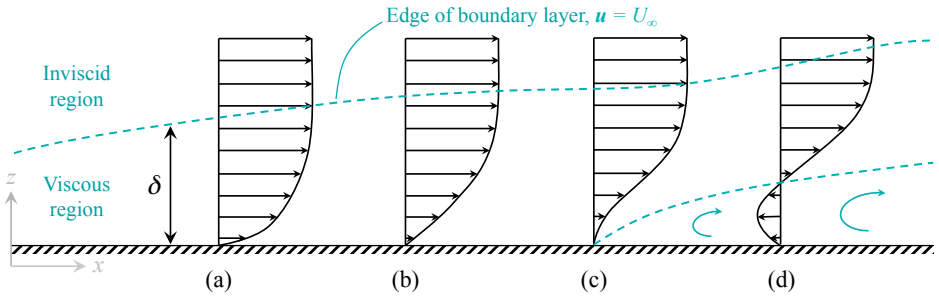

Figure 2.2: Typical velocity profiles in an adverse pressure-gradient flow, resulting in boundary-layer separation and the creation of a reversed-flow region (starting at (c)).

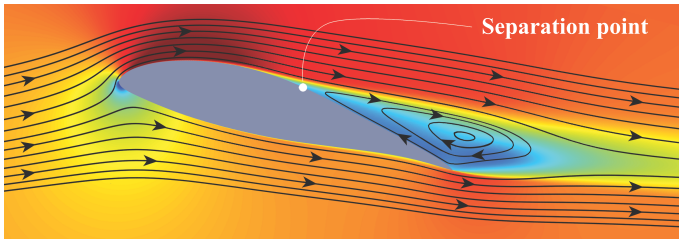

Figure 2.3: Streamlines around an airfoil at positive angle of attack, including the region with recirculating flow behind the separation point.

of separated flow (see figure 1.2). This part of the blade does not generate any useful power (due to the strongly reduced lift force), but on the contrary causes an additional resistance which must be overcome, thereby strongly reducing the efficiency of the turbine. It is clear that in such cases flow separation is highly undesirable and should be prevented as much as possible.

2.3. VORTEX GENERATORS AS MEANS OF PASSIVE FLOW CONTROL

Flow control consists of the act of manipulating a flow field in such a way as to obtain a desired change. This can be done through a wide variety of means, either actively or passively, in order to obtain an even wider variety in objectives. An excellent and extensive overview of both is given by Gad-El-Hak [27]. Below, we give a brief introduction to the field of flow control, followed by a more extensive elaboration on vortex generators.

2.3.1. TYPES OF FLOW CONTROL

Flow control is an area of research hotly pursued by both scientists and engineers. It finds its origin in the work of Prandtl, as a good understanding of flow physics is essential when aiming to favorably alter the character of a flow field. However, Prandtl's contribution extents beyond his work on boundary-layer theory, as he also was the first to actively control a flow. In [81] he describes the successful use of suction in order to delay boundary-layer separation from the surface of a cylinder.

Nowadays, flow control is used in many areas involving fluids, for the purpose of either drag reduction, lift enhancement, mixing augmentation, noise suppression or a combination hereof. In order to reach these goals, flow separation may be prevented or provoked, laminar-to-turbulent transition delayed or advanced, or turbulence levels enhanced or suppressed. Usually an effective strategy requires compromises to be made, as flow-control goals are strongly interrelated and often adversely effect each other. For example, to enhance lift generation it might be wise to trigger transition from a laminar to a turbulent boundary layer, as the latter is less susceptible to flow separation, but doing so has the side effect of increased skin-friction drag.

Flow control in its most basic form consists of an optimal shaping of the geometry of interest. However, a wide variety of additional flow-control strategies is available. These are typically classified according to their energy expenditure as being either passive or active. Passive flow-control devices are usually the simplest, requiring no auxiliary power to operate. Vortex generators are probably the most well-known and widely applied means of passive flow control. Other examples in this category include boundary-layer tripping to advance the transition to turbulent flow, winglets placed at the tip of airplane wings to effectively increase the lift-generating surface [105], and the use of a serrated trailing edge for noise reduction by the attenuation of vortex shedding [66]. In general, passive flow-control devices have the advantage of being both simple and reliable. However, their constant presence induces a drag contribution that can strongly limit the performance in off-design conditions.

Active flow-control techniques, on the other hand, do require energy expenditure for their operation, thereby having the advantageous ability of being active only when re-

quired. However, this makes them also more complex and thereby less reliable. Within the category of active flow control, further distinction can be made between predetermined techniques and reactive control based on a control loop. The latter category makes use of a closed feedback in which the control can be continuously adapted based on real-time measurements. The suction used by Prandtl [81] is an example of active control, where a pump is used to remove the low-momentum fluid close to the surface, either through a porous surface or a series of slots. Present synthetic jet actuators [2] use periodic suction and injection to achieve this goal. Furthermore, heating and cooling of a surface can influence the flow via its effect on viscosity and density [60]. Plasma actuators form another promising type of active flow control [69]. Retractable vortex generators also fall within this category.

2.3.2. PHYSICAL PRINCIPLES OF VORTEX GENERATORS

In this thesis we focus our attention to passive vane-type vortex generators (VGs), which are widely used to postpone, or even completely prevent, flow separation. Although in some instances it can be beneficial to provoke separation, generally prevention of separation is desired to reduce form drag, delay stall, enhance lift generation and improve pressure recovery. Since Taylor first proposed the use of VGs in 1948 [102] to achieve this goal, VGs have found wide application on aircraft wings, compressor and wind turbine blades, and diffusers. An illustration of their possible benefits is included in figure 2.4, which shows the enhanced lift-generating capability of an airfoil when equipped with VGs. Effective application of VGs therefore bears a large economical importance.

VGs are passive flow-mixing devices that essentially consist of small-aspect-ratio airfoils (or just thin plates) that are mounted normal to a surface, as visualized in figure 2.5. As they are typically mounted at an angle to the incoming flow, VGs act as small lifting surfaces that generate an accelerating force in the crossflow direction. Similar to an airfoil at an angle of attack, a low-pressure region is created at the back side of the VG, called the suction side. Due to the difference in pressure with respect to the front side, this suction region causes the incoming flow to curl over the top of the VG, thereby generating a (streamwise) tip vortex that trails downstream.

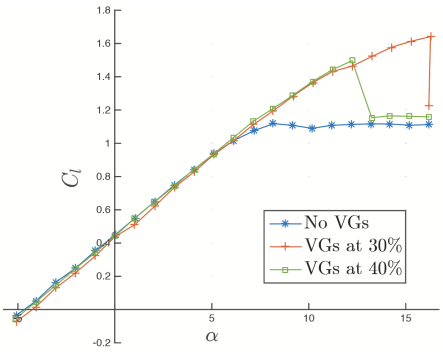

Figure 2.4: Effect of VGs on the lift curve of an airfoil. Data from [62].

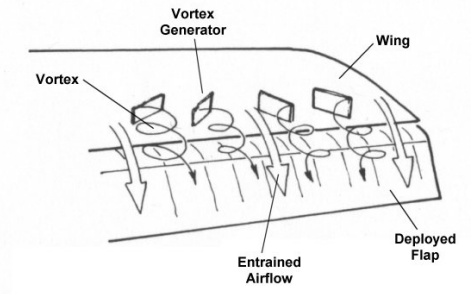

Figure 2.5: Generation of streamwise vortices by VGs on a wing (©Aerospaceweb.org).

The details of the vortex structures that emerge due to the flow around a VG, and their interactions with the (usually turbulent) boundary layer, are complex and have been the subject of several (experimental) studies, including [18, 19, 35, 59, 88, 109, 116, 119]. The swirling motion discussed above is dominated by a primary trailing vortex shed from the tip of the VG. However, its shape, strength and path are influenced by other minor vortex structures that arise around the VG. These include the vortex that arises at the junction between the surface and the VG and the horseshoe vortices near the VG leading edge, which trail downstream at each side of the vane [109]. These vortices are weaker than the main tip vortex and usually dissipate rather quickly under the action of viscosity, however, they still cause perturbations and deformations of the primary trailing vortex. The primary vortex structures are illustrated and indicated in black in figure 2.6.

Moreover, secondary vortices can be created by the interaction between a primary vortex and the boundary layer. Close to a surface, the motion of a primary vortex results in the creation of a thin stress-induced layer of low-momentum flow with opposing vorticity [35, 88]. This region is thickest near the upflow side of the vortex, where the crossflow basically experiences an adverse pressure gradient which may induce a minor separation region. If this happens, a bubble can be created containing vorticity of a sense opposite to that of the primary vortex, resulting in the presence of a secondary vortex that influences the evolution of the primary vortex. If the created secondary vortex is strong, it might even induce the creation of a tertiary vortex according to the same principle [109]. Secondary vortices can arise both on the VG surface and on the main surface of interest, and typically disappear quickly as distinct structures due to their interaction with the much stronger primary vortex. The layer with opposing vorticity between the main vortex and the surface, however, remains clearly present as the vortex evolves downstream of the VG. It should be noted that the created vortex structures de-

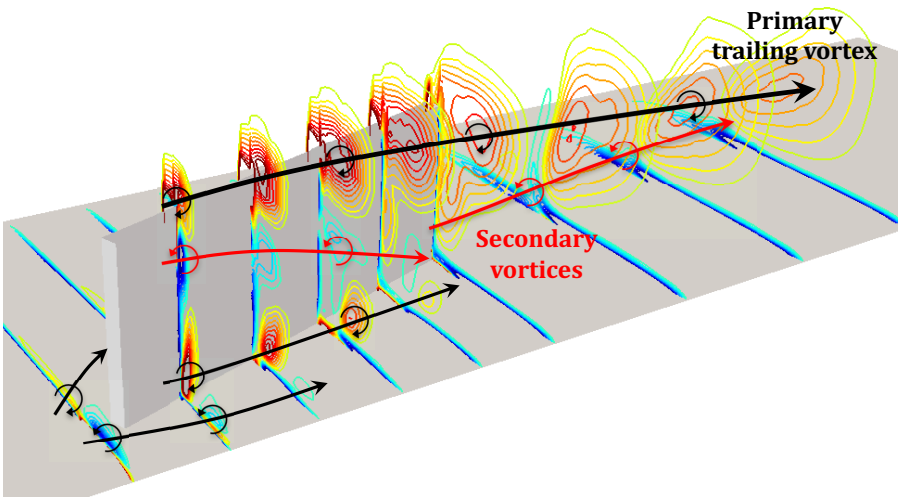

Figure 2.6: Vorticity contours with an illustration of the primary and secondary vortices arising around a vane-type VG.

pend strongly on the VG's geometry and the characteristics of the incoming flow. This will be further elaborated on in the next section.

The overall effect of the created vortical structures is to overturn the near-wall flow via macro motions, where the primary tip vortex is the main contributor. High-momentum fluid particles in the outer part (or outside) of the boundary layer are swept along a helical path towards the surface, where they mix with the low-momentum (retarded) fluid particles near the wall. This way additional energy is effectively added to the near-wall region, thereby re-energizing the retarded fluid particles such that they can overcome stronger adverse pressure gradients [5, 78, 86]. The presence of a VG thus modifies the shape of the local velocity profiles, making them more full. In the sense of separation prevention, the effect of such flow mixing is thus equivalent to a decrease in pressure gradient [86]. As the created vortices evolve downstream, they grow in size and decay in strength due to viscous and turbulent dissipation. Hence, the effect of VGs varies with location and only extends a limited distance downstream.

Unfortunately, the favorable flow-mixing properties of VGs come at the cost of a drag penalty. This is partly due to the skin friction of the VG surface and its induced drag, but the largest contribution is the form drag caused by the separated flow region on the rear part of the VG suction side [88]. This drag penalty reduces the efficiency gains obtained by the use of VGs, and therefore should be kept minimal.

One solution to reduce the drag penalty consists of reducing the size of the VG, and in particularly its height [55, 83]. Whereas conventional VG designs have a height approximately equal to the boundary layer thickness δ, so-called submerged VGs typically have a height of only $\delta/3$ or less. This size reduction significantly diminishes parasitic drag. Furthermore, it is observed that the tip vortex created over a submerged VG can stretch such that it covers nearly the entire device vertically, thereby preventing flow separation over the VG's suction side [119] and having a favorable effect on the amount of form drag.

Given similar situations, a submerged VG creates a primary tip vortex that is smaller, less circular, situated closer to the surface, and weaker [119], compared to a conventional VG. The latter is attributed to the fact that the VG now operates in the lower layers of the boundary layer, where the velocity profile is less full and therefore fluid particles are less energetic. Apart from being weaker upon formation, the streamwise vortex created by a submerged VG also displays a higher decay rate of vorticity due to its proximity to the surface, as the resulting higher shear flow enhances the vortex dissipation process.

Over the last decades, research has shown that submerged VGs can be just as effective in postponing flow separation as conventional VGs [56]. However, due to the lower strength and higher decay rate, submerged VGs need to be positioned closer to the nominal separation point (i.e. in absence of a VG) to generate the same effect as a conventional VG. Moreover, the range in which they are effective is smaller and therefore their use is less suitable for situations with a large uncertainty related to the location of the separation point. Their practical use thus requires accurate information about the position of the nominal separation point, and that this separation point is more or less fixed.

2.3.3. TYPES AND LAY-OUTS OF VORTEX GENERATORS

For a given nominal flow situation, the created vortex structures depend to a large extent on the VG configuration, including geometry and positioning. Generally VGs are combined in large arrays in order to influence the boundary layer in a wide area. The arrangement of the individual VGs in such an array has of course a large impact on the downstream evolution of the streamwise vortices due to interaction effects. Optimal design of VG arrays is therefore not straightforward, as geometry, positioning and flow conditions are strongly interrelated. Several studies have been performed in this respect, see for example [31, 57, 59, 77, 78, 86, 115]. An early design guide for VGs is presented by Pearcey [78], who studied several lay-outs for vane-type VGs. There it is argued that the success of a VG configuration depends critically on the strength and position of the vortices in the region near the adverse pressure gradient, and hence on the paths of the vortices as they are convected downstream.

When considering an individual (vane-type) VG, relative height (with respect to δ), aspect ratio, angle with respect to the incoming flow, and the planform area, can be identified as the characteristic geometric parameters. As already discussed in the previous section, lowering the VG height h has a favorable effect on the drag penalty, but comes at the cost of reduced vortex strength and increased decay rate. Still, submerged VGs are shown to be more effective than VGs with a conventional height of order δ [31, 57]. Apart from strength and decay rate, the VG height also determines the size and distance from the wall of the vortex core. Furthermore, it is observed that the incidence angle β directly influences the strength of the main vortex, with the vortex strength increasing more or less linearly with β [77, 78]. The aspect ratio, defined as the ratio between the VG's length and height l/h, on the other hand only has minor influence on the VG's effectiveness. A ratio of $l/h = 2$ is found to be the minimum requirement [31, 78], with larger values mainly adding to the drag penalty.

Various VG shapes have been proposed in literature, but the ones most commonly used in practice consist of straight vane-type VGs with either a rectangular or triangular planform. Typical shapes are illustrated in figure 2.7, where it should be noted that there are more possibilities than shown. The use of a triangular VG over a rectangular VG is attractive, since the smaller planform area has a beneficial effect on the drag penalty. Indeed, it was shown by Godard [31], among others, that triangular vanes are more effective than rectangular ones. Although the flow structures around the vane are very similar, a stronger vortex is created resulting in a stronger re-energizing effect of the vortex. However, a study performed by Velte [107] for a high-Re boundary layer indicated no notable difference between both shapes. In the same study straight VGs were compared with cambered VGs, where the vortices created by the latter shape were observed to be smaller and weaker. Aerodynamically shaped VGs, consisting of an airfoil shape instead of a flat plate, on the other hand do effectively improve the VG's efficiency [33]. The choice of a suitable airfoil profile allows the reduction of the separated region on the suction side of the VG, thereby reducing the form drag.

Probably the most critical design consideration, and the least straightforward to assess, is the placement of the individual VGs within an array. The interaction with the vortices created by neighboring VGs determines the location and strength of the vortex cores in the region of interest (i.e. near the nominal separation point). Essentially,

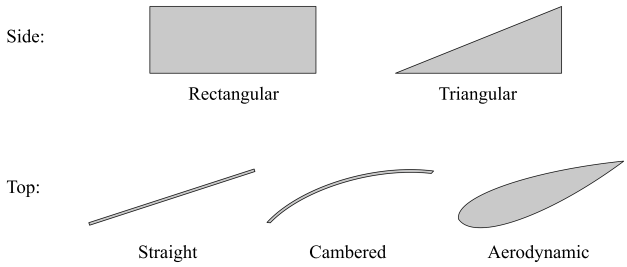

Figure 2.7: Side and top views, illustrating typical VG shape options.

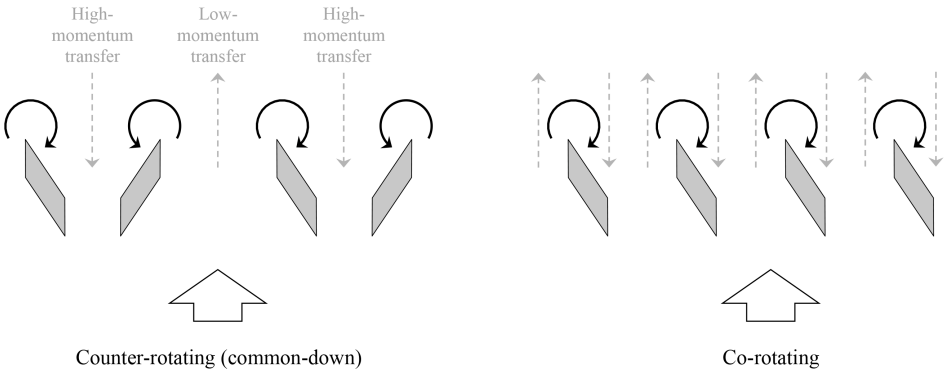

Figure 2.8: VG-array configurations.

distinction can be made between two configuration types: a V-shaped counter-rotating configuration, or a parallel co-rotating configuration, as illustrated in figure 2.8. For a counter-rotating configuration, one can further distinguish between common-up or common-down lay-outs, depending on the direction of momentum transfer between both VGs of a VG pair.

A first extensive study towards optimal VG-array configurations was performed by Pearcey in 1961 [78], who concluded that a co-rotating configuration is favorable, provided that the VG spacing is sufficient. A sufficient spacing is in his work quantified as being larger than three times the VG height. This is required to prevent cancellation of momentum transfer (and corresponding vortex damping), which occurs when the upflow of one vortex interferes with the downflow of another. Co-rotating VG arrays are typically equally spaced, yielding the favorable property of relatively straight vortex paths. Because the effects of neighboring vortices are equal and opposite in this case, the vortex array remains undisturbed as the vortices trail downstream. Only some overall lateral movement will occur, due to the induced velocities of the so-called image vortices (i.e. the ground effect). These properties make the path of a co-rotating vortex array relatively straightforward to predict.

Later research [31, 77, 114], however, indicated that counter-rotating VG configurations have the potential of being up to twice as effective as co-rotating configura-

tions. For counter-rotating configurations the wall normal velocity components are reinforced by the effect of the neighboring VGs, thereby increasing the transfer of momentum across the boundary layer. A drawback of counter-rotating configurations, though, is that the interaction effects cause vortices to move substantially as they evolve downstream [78]. Especially the tendency of the centers to move away from the surface limits the range of effectiveness. However, proper configuration design can eliminate this problem. In this sense, common-down configurations are generally favored as they force the vortex cores to stay close to the wall [77]. In general, the vortices created by a common-down VG array are non-equidistant, with the spacing between the vortices from a VG pair being smaller than the spacing between neighboring VG pairs. This causes the vortices created by a VG pair to initially move away from each other and towards the wall. Only when the vortices in the array become equidistant, they will start moving away from the wall again. The spacing between the VGs in a VG pair (d), and between the different pairs in a VG array (D), are therefore important design parameters.

Overall, the optimal VG configuration depends heavily on the situation of interest, and the requirements for maximum effectiveness, range of effectiveness and a low drag penalty are often conflicting. Optimal designs ideally take into account the complex dynamics of the flow, with possible interactions and mergers of vortices. An attempt to find an optimal VG configuration while considering some of these requirements was made by Godard and Stanislas [31], who performed an optimization study for VGs on the suction side of an airfoil, considering incompressible flow and yielding a good representation for several blade and wing applications. They found that the most effective configuration consists of counter-rotating, common-down triangular submerged vanes, positioned at an angle of 18° with respect to the incoming flow. Furthermore, the vanes ideally have a height of 37% of the boundary layer thickness and an aspect ratio of $l/h = 2$. Optimal spacing distances are identified to be $d = 2.5h$ between the VG trailing edges of a pair, and $D = 6h$ between neighboring VG pairs.

2.4. CONCLUSION

Passive VGs constitute a simple, yet effective, means to favorably alter the flow field over a lift-generating surface, for example by delaying boundary-layer separation. They therefore are capable of yielding significant performance improvements by enhancing lift generation and reducing form drag, causing them to have found widespread application. Large variations with respect to their shape and arrangement are therefore observed.

VGs typically consist of small vane-type structures, with a height in the order of the boundary-layer thickness, that are mounted in wall-normal direction and at an angle to the incoming flow on a surface of interest. When a flow encounters a VG, complex small-scale flow structures are formed that eventually evolve to a streamwise vortex, the characteristics of which largely depend on both the inflow conditions and the VG geometry. The flow circulation induced by this vortex causes the near-wall energy levels to increase, such that the tendency of the boundary-layer to separate from the surface reduces. To maximize the region where the flow is effected, VGs are typically arranged in arrays, thus generating a pattern of several interacting streamwise vortices.

Hence, the addition of VG arrays to a surface largely alters the local flow field. Effi-

cient designs therefore require the ability to make reliable predictions regarding the effect a VG configuration has on the flow. The small scale of VGs in combination with the complex flow patterns and interactions, however, poses great challenges in this respect. Moreover, the wide variation in applications precludes the formulation of generally applicable design guidelines. Affordable and accurate analysis techniques are therefore required in order to solve these high-dimensional design problems.

3

SIMULATING VORTEX GENERATOR INDUCED FLOWS: STATE OF THE ART

As discussed in chapter 2, the addition of VGs to a boundary layer fundamentally alters the flow field, locally as well as far downstream. For optimal designs these effects can therefore not be ignored and need to be carefully considered, from an early design stage on. However, due to the small size of a VG, inclusion of VG arrays in detailed analyses is complex, computationally expensive and time consuming. Even though their influence was known to be large, for this reason VGs were neglected in early-stage analyses for many years. They were only included in later design stages, for example during experimental testing. Only with the rise of CFD could the effects of VGs on the flow field be taken into account with sufficient accuracy.

In this chapter the state of the art with respect to the simulation of VG effects on a flow field is discussed. We start with an overview of analytical methods in section 3.1, which can be used to obtain initial predictions with respect to the strength and shape of the generated vortices. This is followed by a more elaborate overview of numerical approaches, which in general yield results with improved accuracy due to their consideration of the entire flow field. Within this category, distinction is made between fully resolved (section 3.2), fully modeled (section 3.3) and partly resolved / partly modeled (section 3.4) approaches (according to [100]).

3.1. ANALYTICAL METHODS

A key concept in the theoretical analysis of the effects of VGs on wall-bounded flows is the lifting-line theory. This was another major contribution from Ludwig Prandtl to fluid dynamical theory and the first practical method for predicting aerodynamic properties of finite wings. This theory predicts the lift and induced drag generated by a three-dimensional wing by replacing the wing by an infinite number of horseshoe vortices,

and using the Kutta-Joukowski theorem to relate the sectional lift to the circulation of the bound vortex around each airfoil section. This theory, however, is limited to incompressible, inviscid flow, and does not account for swept wings, low aspect ratio wings and unsteady effects.

Still, when applied to a VG, which resembles a low-aspect ratio wing protruding the boundary layer, lifting-line theory can be used to obtain a reasonable estimate for the strength of the vortex shed at the VG tip, as for example done by Jones in 1957 [45]. In this first extensive approach to analyze the (counter-rotating) vortex system created by a VG array, Jones developed an analytical model based on potential flow theory. This method assumed two-dimensional inviscid flow, thereby not accounting for the viscous vortex core and variations in the streamwise velocity. The effect of the wall was taken into account by addition of mirror image vortices, causing the surface to become a streamline of the vortex field. Although qualitatively useful insights were gained, for example with respect to the path of the vortices, the predicted minimum height of the created vortices from the wall was found to be in considerable excess of experimental values. These quantitative deviations limited the practical use of this early analytical model, and clearly indicated that 3D and viscous effects cannot be neglected when studying the flow downstream of a VG array.

The theory of Jones [45] can be enhanced by considering the swirling velocity and vorticity distribution in the viscous vortex core. Several theoretical descriptions of a single free vortex have been proposed in literature, see for example [12, 13]. One of the simplest is due to Rankine [82], who approximates a free vortex as a solid-body like rotation within the core, exhibiting a linear increase in swirl velocity from the center to the point of maximum swirl velocity, and uses potential theory (similar to Jones [45]) outside this core region. A more sophisticated model is proposed by Lamb [50] and Oseen [74], which overcomes the discontinuity at the core boundary in the Rankine description, and originates from the one-dimensional (axisymmetric) laminar Navier-Stokes equations. This Lamb-Oseen vortex model assumes zero axial and radial velocity and yields a Gaussian distribution for the swirl velocity. Moreover, this theoretical model contains a time-dependent decay, and thereby allows prediction of both the decay in strength and the vortex growth over time (in the 2D context).

For a trailing vortex, however, the axial velocity is not zero. Squire [97] therefore proposed an addition to the Lamb-Oseen model that accounts for this non-zero axial velocity. In addition, he also included a viscosity term to account for enhanced diffusion of vorticity due to the effects of turbulence generation. An alternative consists of the Batchelor vortex model [10], which uses a non-uniform axisymmetrical axial velocity and thereby accounts for the axial momentum deficit caused by the vortex. For the case of vortices generated by a VG in a turbulent wall-bounded flow, the latter model was later extended by Velte et al. [108] based on the observation of helical symmetry, yielding an improved description of the axial velocity profile.

The above theoretical single-vortex models can yield a good representation of the total velocity field of a vortex system generated by a VG array, when using mirror image vortices to simulate the wall, and making use of superposition to include the effects of neighboring vortices. However, several drawbacks are related to these models, limiting their use for accurate flow predictions. Firstly, they only describe the vortex system

at a crossplane immediately downstream of the VG, but do not account for the downstream propagation. Additionally, these vortex descriptions rely on several input quantities which are usually unknown. These typically are circulation (and/or peak vorticity) and the vortex core size. For the model of Velte [108] even the helical pitch is a required input parameter. This makes these vortex-profile models by themselves impractical for use, and additional relations are therefore required.

Probably the simplest estimate for the vortex's circulation consists of (by Helmholtz's theorem) equating it to the VG's bound vortex circulation, which can be approximated using the Kutta-Joukowski condition, as done in [34], among others. Furthermore, improvements of lifting-line theory by means of empirical relations have been proposed to enhance the dependence of the shed vortex's characteristics on the VG geometry and impinging flow conditions. Wendt and Reichert [113, 115], for example, performed an experimental study towards the initial vortex circulation and crossplane peak vorticity for airfoil shaped VGs, assuming that at one VG chord downstream of the VG's trailing edge the vortex is fully developed. Circulation in their work was modeled based on Prandtl's lifting-line formula, whereas a correlation for the peak vorticity was derived by equating the moment at the airfoil tip to the rate of angular-momentum production of the vortex. Bray [13] used a similar approach to model the vortices shed by vane-type VGs, however, he modified the lifting-line expression for circulation to obtain a quadratic variation with the incidence angle, in an attempt to account for stall over the VG's suction side. Additionally, in [13] the peak vorticity was expressed as function of the vortex radius, which was modeled by a purely empirical relation.

Recently, Poole et al. [79] proposed a theoretically extended version of lifting-line theory that accounts for the low aspect ratio of a VG and takes into account the varying velocity profile of the boundary layer. Moreover, they added a vortex-lift component based on Polhamus' suction theory for delta wings, to include the addition of lift generated due to vortex roll-up along the length of the VG. By including these additional physics, they managed to derive an expression for circulation that exhibits a significantly reduced error compared to the empirical model of Wendt.

However, the evolution of the vortex resulting from the above-mentioned theoretical vortex-profile models is hard to predict analytically, as this requires consideration of viscous effects. In contrast to the inviscid potential approach used by Jones [45], Bray [13] attempted to formulate an empirical relation for the viscous decay of vortex strength. Although the latter also yields a reasonable estimate for the growth of the vortex core, it cannot be used to make predictions with respect to interaction effects on the paths of the vortices. An analytical viscous analysis has been attempted by Smith [91], but his approach only applies to the very specific situation of low-profile triangular vanes not extending beyond the logarithmic layer of the boundary layer. In general, useful results with respect to vortex evolution require the use of numerical tools rather than analytic methods.

Despite their limitations, analytical approaches are particularly suited for getting a rough idea about appropriate VG configurations in an early design phase, due to their low complexity and low computational cost. Research toward an improved analytical prediction of the (initial) vortex strength and shape is therefore ongoing, including both theoretical developments like [79] and enhancements based on (semi-) empirical rela-

tions [13, 115]. Moreover, these results can be of value as input for numerical simulations, as will be discussed in section 3.3.

3.2. FULLY-RESOLVED SIMULATIONS

When viscous and 3D flow effects are to be taken into account, analytical methods are limited and numerical approaches are required. CFD simulations are therefore the preferred method for the study of VG effects, as they can in principle accurately model the physics associated with the flow patterns induced by individual VGs and their combined effects when operating in arrays. When using a finite-volume CFD approach, the region occupied by the fluid is divided into discrete cells, constituting the numerical mesh. In every cell, the governing flow equations (e.g. (2.1) and (2.2)) are implemented in discrete form, and their residuals used to evolve the flow variables throughout the domain.

A conventional CFD approach to resolving VG-induced flow fields consists of constructing a body-fitted mesh (BFM) around all solid surfaces, including the surface of interest (e.g. a wind-turbine blade) and the VG. Such a fully-resolved approach theoretically possesses the highest achievable accuracy, depending on the choices made for the governing equations to be solved, and the related discretization schemes.

3.2.1. TIME-RESOLVED VG SIMULATIONS

Direct numerical simulations (DNS) provide a time-resolved solution of the full Navier-Stokes equations, including the smallest scales in the flow, and are thus capable of yielding highly-accurate VG-induced flow simulations. This has, for example, been done by Spalart et al. [94] for a periodic array of co-rotating VGs in a supersonic flat-plate boundary layer, in the context of an academic study. However, the high accuracy of DNS comes at an enormous computational cost, thereby restricting their use to low Reynolds numbers and making them unsuitable for typical VG applications.

Large eddy simulations (LES) offer a more affordable alternative for DNS, enabling the calculation of time-resolved flow fields by modeling instead of resolving the smallest turbulent scales, thereby allowing for less refined meshes outside the boundary layer. This approach has also been used to simulate VG-induced flow fields, yielding highly accurate results [14, 106]. Still, the cost of LES is prohibitively expensive for high Reynolds number wall-bounded flows, thereby limiting its applicability for general industrial purposes.

3.2.2. RANS SIMULATIONS OF FLOWS AROUND VGS

Numerical solution of the Reynolds-averaged Navier-Stokes (RANS) equations is currently the preferred method for resolving the flow over a VG configuration, combining a good accuracy with a reasonable computational cost (see, among others, [1, 24, 47, 117]).

THE REYNOLDS AVERAGED NAVIER STOKES EQUATIONS

The main idea behind the RANS equations consists of using statistical quantities to describe a turbulent flow field, rather than the instantaneous quantities used in (2.1) and (2.2). At the high *Re* that govern turbulent flows, the evolution of the flow field is extremely sensitive to small changes in, for example, initial and boundary conditions and

inhomogeneities, yielding a seemingly random behavior of the flow. At the end of the 19th century, Osborne Reynolds therefore proposed to describe the flow field in terms of its mean and fluctuating parts using the decompositions

$$\mathbf{u} = \overline{\mathbf{u}} + \mathbf{u}' \tag{3.1}$$

$$p = \overline{p} + p' \tag{3.2}$$

where, typically, the mean velocity and pressure fields ($\overline{\mathbf{u}}$ and $\overline{p}$ respectively) are defined as the time-averaged instantaneous fields. By considering the limiting case of averaging over a period much longer than the largest time scale of the turbulent motion, the mean quantities become time independent. Alternatively, unsteady RANS (URANS) methods can be used, which consider the ensemble rather than the temporal average in order to take into account some of the large-scale unsteadiness in the flow.

Upon substitution of the above decompositions into the Navier Stokes equations, which describe the instantaneous flow field and account for all turbulence effects up to the smallest (Kolmogorov) scales, equations for the (steady) mean flow and for the fluctuating parts can be obtained, see for example [53, 80]. The mean flow RANS equations can be written in component form, when neglecting external body forces, as

$$\frac{\partial \rho \overline{u}_j}{\partial x_j} = 0, \tag{3.3}$$

$$\frac{\partial \rho \overline{u}_i \overline{u}_j}{\partial x_j} = -\frac{\partial \overline{p}}{\partial x_i} + \frac{\partial}{\partial x_j}\left[\mu\left(\frac{\partial \overline{u}_i}{\partial x_j} + \frac{\partial \overline{u}_j}{\partial x_i}\right) - \rho\overline{u_i' u_j'}\right], \tag{3.4}$$

where μ denotes the dynamic viscosity. Compared to the steady Navier-Stokes equations, the above RANS equations for the mean flow are very similar, apart from the addition of an apparent stress term $\rho\overline{u_i' u_j'}$, called the (turbulent) Reynolds stress. The Reynolds stress tensor stems from momentum transfer by the fluctuating velocity field, and accounts for the effect of the velocity fluctuations on the mean flow, thereby being crucial in the description of the turbulent flow field.

For a statistically steady 3D flow, the RANS equations consist of four independent governing equations, whereas the number of unknowns is larger: in addition to the three velocity components and the pressure, the additional Reynolds stress tensor, which is symmetric, introduces 6 additional unknowns. This closure problem prevents a direct solution of (3.3) and (3.4). The Reynolds stresses therefore need to be specified somehow to obtain a solution for the turbulent mean flow.

If an exact representation of the Reynolds stresses would be available, equations (3.3) and (3.4) would yield an exact representation of the turbulent flow field. Unfortunately, such a representation is unavailable, and hence a model must be used. Depending on the selected model and flow situation, major errors might be introduced to the overall solution. A significant number of models has been proposed in literature, ranging from simple algebraic relations to the solution of full differential transport models. In general, two main groups of models for the Reynolds stresses can be identified, being either based on the turbulent-viscosity assumption, or on the solution of a modeled transport equation for the stress components.

TURBULENT-VISCOSITY MODELS

The turbulent-viscosity hypothesis was formulated by Boussinesq in 1877 (hence it is also known as the Boussinesq hypothesis) and it states that the deviatoric part of the Reynolds stress is proportional to the mean rate of strain S_{ij}. Moreover, it specifies this relationship to be linear and determined by a scalar constant, called the turbulent viscosity or the eddy viscosity μ_t, as

$$a_{ij} = -\rho\overline{u_i' u_j'} + \frac{2}{3}\rho k\delta_{ij} = 2\mu_t S_{ij} = \mu_t\left(\frac{\partial \overline{u}_i}{\partial x_j} + \frac{\partial \overline{u}_j}{\partial x_i}\right), \tag{3.5}$$

with the turbulent kinetic energy

$$k = \frac{1}{2}\overline{u_i' u_i'}. \tag{3.6}$$

This hypothesis reduces the burden significantly, as now only the scalar quantity μ_t is left to be determined in order to obtain closure for the RANS equations. A wide variety of so-called linear eddy-viscosity models is available, typically classified according to the number of equations that need to be solved. A comprehensive overview can be found in [53].

The simplest class of linear eddy-viscosity models consists of the algebraic models, which do not require the solution of an additional equation. However, these are typically too simple for use in general situations. In the class of one-equation models, the Spalart-Allmaras model [92] is by far most popular. Despite its simplicity, requiring the solution of a single transport equation for the kinematic eddy viscosity ν_t, this model is widely and successfully used in the study of external aerodynamics.

Within the category of linear eddy-viscosity models, the use of two-equation models is most widespread, providing an estimate for ν_t in combination with a description of the turbulent scales by solving transport equations for the turbulent kinetic energy k and the rate of dissipation ϵ (e.g. [46, 52]), or for k and the specific dissipation ω (e.g. [118]). A very successful model is Menter's $k-\omega$ shear-stress transport (SST) model [64], which combines the best of two worlds by blending the $k-\omega$ model close to the wall, with the $k-\epsilon$ model in the freestream. Moreover, by also including Bradshaw's assumption (i.e. that the principal shear stress is linearly related to the turbulent kinetic energy) the effect of the transport of principal turbulent shear stress is partly accounted for. This way, the limited performance of $k-\epsilon$ models for large mean pressure gradients, and the excessive sensitivity to the inlet freestream turbulence properties of $k-\omega$ models, are both overcome, yielding improved results for flows exhibiting adverse pressure gradients and/or separation.

Unfortunately, in its simplicity the Boussinesq hypothesis overlooks the spatial coherence of turbulent structures. This assumption is reasonable for simple shear flows, where the turbulent characteristics change slowly following the mean flow and therefore the Reynolds-stress balance is dominated by local processes. This is for example the case in channel flows and undisturbed boundary layers. However, for more complex flows governed by high strain rates, like strongly swirling flows or flows with significant streamline curvature, the hypothesis fails significantly, regardless of the closure approximation made to determine the turbulent viscosity [53, 80]. Moreover, the above mentioned eddy-viscosity models rely heavily on empirical constants, causing additional errors for flow situations that fall outside their calibrated range.

Corrections have been proposed to develop improved eddy-viscosity models, for example by accounting for streamline curvature [90, 93]. Additionally, a class of nonlinear eddy-viscosity models emerged, which no longer assume a linear relation between the turbulent stresses and the mean rate of strain. Instead, a polynomial expansion is constructed, with the expansion coefficients being based on calibration with experimental or numerical data [17, 95]. However, none of the above extensions yield generally improved flow-field results, as they are all based on empirical functions that are optimized for specific flow situations.

REYNOLDS-STRESS MODELS

To overcome the defects of the turbulent-viscosity assumption, closure relations have been formulated that determine the Reynolds-stress components directly from the exact governing equations. Such Reynolds-stress models typically require the solution of 7 coupled nonlinear partial differential equations, in addition to the mean-flow equations, to account for all stress components and the (specific) dissipation. Despite retaining some exact terms, the resulting transport equations still require models to account for the turbulent dissipation and diffusion, and the pressure-velocity interaction (accounting for the normal-stress redistribution) [53, 80]. By introducing these models, inaccuracies inevitably enter the solution of the turbulent flow field.

As with the turbulent-viscosity models, many different variants to model these additional unknowns can be found in literature. Widely used examples include the LRR model by Launder, Reece and Rodi [51] and the SSG model by Speziale, Sarkar and Gatski [96]. The most important difference between these models consists of the way in which the pressure-velocity correlations are approximated. This is the most challenging part to model, as this interaction is highly non-local. Elliptical relaxation allows for non-local effects to be included [22], thereby offering a higher level of description. However, these models come at the cost of an increased complexity and are strongly affected by the boundary conditions imposed at the wall.

Reynolds-stress models can in general be successfully applied (opposed to turbulent-viscosity models) for flows with significant mean streamline curvature and flows with strong swirl or mean rotation. However, for very complex flows, for example 3D separated flow over a curved surface, Reynolds-stress models may give solutions that are no better than, or even worse than, turbulent-viscosity models [53]. Moreover, apart from the complexity of creating accurate Reynolds-stress models, this approach poses an increased computational challenge. The nature of these equations is such that the numerical stability of the discretized RANS system is reduced, especially compared to the use of turbulent-viscosity models.

In order to enhance stability and reduce the numerical cost, an additional class of algebraic stress models has arisen. Initially implicit relations were extracted based on the differential Reynolds-stress models discussed above [84]. However, these implicit relations were found to be lacking computational robustness, resulting in the formulation of explicit relations instead. These explicit algebraic stress models are functionally equivalent to the previously mentioned nonlinear eddy-viscosity models, but differ fundamentally in the determination of the expansion coefficients, which are now based on the Reynolds-stress transport equations rather than a calibration process. An overview of such models can be found in [28].

FULLY-RESOLVED RANS SIMULATIONS OF VGS

The RANS equations enable computation of the time-averaged VG-induced flow field, by decomposing the flow into its mean (time-averaged) and fluctuating components. The requirements on the numerical mesh are such that the mean-flow variations can be resolved, thus posing looser requirements on the mesh resolution than LES and DNS approaches. By considering steady instead of transient flow, the computational cost is further reduced. However, the accuracy of the method depends on the choice for the turbulence model that is used to take into account the influence of the fluctuating components, corresponding to the small turbulent eddies.

Research indicates that conventional turbulent-viscosity models are able to yield satisfactory estimates for the mean-flow features of a single vortex [24, 54], but show reduced accuracy when vortex interactions are considered [6, 117]. The main observed deficiencies are underprediction of the streamwise vorticity and deviations with respect to the vortex's trajectory, where it should be mentioned that strong variations in accuracy are observed depending on the particular turbulent-viscosity model used. For example, the two-equation $k-\omega$ SST model has been reported to perform significantly better than the one-equation Spalart Allmaras model [1, 14, 117], which shows high diffusion and typically underestimates the vorticity and therefore the effect of the VG. Especially for flat-plate cases, and depending on the purpose, the $k-\omega$ SST model can yield sufficiently accurate results [14, 24], similar to those obtained when using an algebraic stress model [14]. However, for more complex situations, for example airfoil flows, the latter category clearly outperforms standard turbulent-viscosity models. Reliable pressure distributions can be obtained with turbulent-viscosity RANS simulations, however, the prediction of aerodynamic coefficients for high angles of attack (especially near stall) is prone to errors [14, 47, 61]. Moreover, comparison with (full) Reynolds-stress models highlights the inherent weakness of conventional turbulent-viscosity models for boundary-layer flows containing vortical structures [117].

In [94], Spalart et al. state that in general, flow situations involving vortex interactions are too complex for RANS methods. However, the formation of the vortex itself is largely an inviscid process, and therefore RANS errors only become apparent when the vortices start aging and interacting. Hence, body-fitted RANS simulations offer a good reliability for studying the vortex-formation process. For highly-accurate results concerning the downstream evolution, the choice of turbulence model is of large importance.

Effectively capturing and convecting downstream the vortices created by VGs requires very high mesh resolutions both around the VG and in its wake. As discussed in section 2.3.2, the physics involved in the vortex-formation process around a VG are complex, and studies of grid requirements thus reveal that it is necessary to adequately resolve the VG's boundary layer in order to obtain accurate flow representations [117]. Difficulties in the mesh-generation process typically arise due to the combination of these high mesh requirements, and the large difference in scale between a VG and the surface of interest. Inclusion of VGs in body-fitted meshes therefore typically causes a large increase in the overall mesh size, and hence the related numerical cost. Moreover, creation of a high-quality mesh becomes cumbersome and time-consuming (although the effort can be reduced by making use of the Chimera or overset grid approach, as for example done in [30]). For these reasons, body-fitted mesh simulations are rarely used

for configurations other than those involving a single VG or VG pair.

3.2.3. IMMERSED-BOUNDARY METHODS

In an attempt to reduce the burden of mesh generation, immersed-boundary methods for VG simulations are gaining popularity [29, 89, 120]. These methods do not explicitly include the VG geometry into the numerical mesh, but rather simulate the presence of a physical boundary though the addition of forcing (source) terms in the cells corresponding to the VG location. The mesh therefore no longer needs to be locally aligned with the VG surface, thus simplifying the mesh-generation process. However, the same requirements with respect to mesh resolution still apply, as these simulations still aim to resolve the full vortex-formation process. An overview of the immersed-boundary method and the different approaches used to simulate the presence of a solid boundary is given in [65].

Although immersed-boundary methods are typically insufficient when a detailed study of the boundary layer is required, You et al. [120] demonstrated the efficacy of LES in combination with this approach to examine both the temporal and spatial evolution of longitudinal vortex pairs embedded in a turbulent boundary layer. This result was confirmed by Shan et al. [89], who successfully used an immersed-boundary method to study the flow-separation control with VGs for a NACA0012 airfoil. Moreover, Ghosh et al. [29] used the immersed-boundary technique to simulate the presence of submerged VGs in a compressible RANS study of oblique-shock / turbulent boundary-layer interactions. Their study, however, shows that deviations from the body-fitted mesh result occur due to insufficient resolution of the VG boundary layer, mainly resulting in an overprediction of the momentum sink effect of the VGs. The immersed-boundary method does thus not avoid the requirement for high mesh resolution close to the VG surface.

3.3. FULLY-MODELED SIMULATIONS

Fully-resolved simulations including VG arrays can deliver the desired accuracy, but at a computational cost too high to be practical. The analytical methods discussed in section 3.1, on the other hand, are computationally cheap but lack the required accuracy. A combination of these two approaches therefore constitutes a logical alternative. As defined in [101], these so-called fully-modeled approaches "model the generated structures or the influence of the modeled VGs".

3.3.1. THREE-DIMENSIONAL APPROACHES

Direct inclusion of a fully-developed vortex into an undisturbed flow field can be a solution to overcome the excessive computational cost related to high-fidelity, fully-resolved, CFD simulations, thereby making VG-induced flow-field information more practical to obtain. These fully-modeled, low-fidelity, approaches do not attempt to resolve all the physics related to the vortex-formation process. Rather, an analytical model is used to predict the strength and shape of the main vortex created by a VG, and only the downstream evolution of this vortex is resolved by the numerical method (illustrated in figure 3.1). Doing so mitigates the requirements posed on the numerical mesh, as the VG geometry no longer needs to be included into the mesh, and the small-scale flow motions

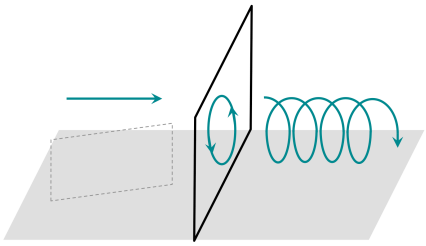

Figure 3.1: Illustration of the fully-modeled simulation concept.

related to vortex formation no longer need to be resolved. Several approaches for these fully-modeled VG simulations have been proposed in literature, differing with respect to both the analytical vortex description and the approach to include the fully-developed vortex into the numerical simulation.

Probably the most intuitive approach consists of directly including a description of the secondary velocity, or vorticity, distribution of the generated vortex to a clean simulation. An early example in this respect is the work performed by Kunik [49] in 1986, who formulated the governing equations in stream-function vorticity form. A vorticity source term, based on the vortex description of Squire [97], was added in the crossplane downstream of the VG. The obtained simulation results were reported to show good qualitative agreement with experimental data.

In later work, the velocity profiles obtained from analytical vortex models were translated to body forces that can be directly added to the momentum (and energy) equations, for example using the approaches proposed by Liu et al. [58] or May [63]. In [58] a Lamb-Oseen viscous vortex profile was added to a LES simulation, using an error-function distribution of the body forces in streamwise direction. Moreover, the model was extended with a streamwise body-force component exhibiting a Gaussian distribution to account for the wake of the VG. Similarly, May [63] imposed a Lamb-Oseen vortex profile onto a clean RANS simulation, making use of Bray's correlation [13] to predict the circulation. However, he did not account for the VG wake and assumed a large value for the peak vorticity, reasoning that a typical RANS mesh has insufficient resolution to resolve this quantity.

As an alternative to the use of a source term, the secondary velocities of a fully-developed vortex can be added as a velocity-jump boundary condition specified at an artificial interface downstream of the VG, as was done by Dudek [20]. She made use of Wendt's empirical vortex description, hence also assuming a Lamb-Oseen vortex profile, but ignored the image vortices, reasoning that viscous wall effects were inherently accounted for by the used RANS code. The grid study performed in [20] indicates that mesh resolutions as coarse as 30% of the VG chord length can be sufficient to obtain reasonable results.

Apart from the intuitive approach of directly altering the flow field, indirect inclusion of a modeled vortex profile through the turbulence model has been proposed. Hansen and Westergaard [34] attempted to model the separation-delay effects of VGs by an increase of the turbulence intensity, thereby simulating the enhanced mixing of the bound-

ary layer and yielding fuller streamwise velocity profiles. Using the Kutta-Joukowsky theorem to obtain an estimate for the circulation, the kinetic energy of the vortex was calculated and translated into an empirically-calibrated turbulence production source term. This model was applied to study the 3D effect of VGs on the separation line for a wind-turbine blade in [34], but the accuracy of the model for this purpose was not assessed.

3.3.2. TWO-DIMENSIONAL APPROACHES

Whereas the above approaches were all applied to 3D simulations, further reduction of the computational cost is possible by considering the vortex evolution in only two dimensions (the wall-normal and streamwise directions). This gain of course comes at the cost of reduced accuracy, as it is clear that 3D effects cannot be neglected in the evolution of the vortex system generated by a VG array. However, depending on the objective, the obtained results can still be useful.

Fully-modeled 2D simulation approaches include for example the above described model of Hansen and Westergaard [34], which can be applied both in 3D and 2D. Due to the limited physics included in the model, it is probably most useful in 2D simulations, as done in [42] for the purpose of obtaining fast estimates for the effect of VGs on the lift and drag polars of airfoils.

Another 2D approach to mimic the increased mixing by adaptation of the turbulence model was developed by Törnblom and Johansson [103]. Assuming a Lamb-Oseen vortex profile, with the circulation calibrated using classical lifting-line theory, they calculated the corresponding wall-normal Reynolds stress contributions and added these to the flow indirectly through forcing functions in the Reynolds stress transport equations. This was done in combination with a drag source term in the momentum equations to account for the velocity deficit in the VG wake. This model was later extended by Von Stillfried et al. [110], who included the strain-rate tensor in the Reynolds-stress descriptions and added statistical forcing terms to previously unforced components of the Reynolds-stress tensor. An observed drawback of both models, however, arises due to the fact that the vortical structures generated by VGs are more stable and therefore persist longer than turbulent structures with the same statistics.

Two-dimensional models that directly include the assumed vortex velocity profile have also been developed. Nikolaou et al. [70] used spanwise averaging of the governing equations (3D RANS) to obtain a set of equivalent 2D equations, that included source terms to take into account some of the 3D flow effects and vortex-induced velocities. The latter were modeled based on a Rankine vortex profile, with their circulation estimated using delta-wing theory.

The computational cost of 2D fully-modeled approaches can be even further reduced when making use of viscous-inviscid simulation methods instead of RANS simulations. Such methods are typically used in the preliminary design study of airfoil geometries, and couple a 2D inviscid panel method with the solution of the boundary-layer equations to include viscous effects. VG effects have been included in the XFOIL [48] and Q^3UIC [25] codes by modification of the integral boundary-layer formulations in order to enhance the turbulence production, similar to the idea of Hansen and Westergaard [34]. This approach allows prediction of the change in pressure distribution over airfoils, and hence aerodynamic forces, but cannot be used to study the evolution of vortex

systems.

The above fully-modeled approaches are in general capable of yielding qualitatively good results, making them suitable for (early) qualitative studies of VG configurations. However, they rely on the inherent assumption that the created vortices satisfy an a priori determined analytical profile, usually in combination with empirical relations that require calibration to obtain quantitatively useful flow-field results. This makes these models less reliable in later design stages when detailed flow information is required. Moreover, as these models fail to take into account the specifics of particular VG geometries and/or flow conditions for the situation of interest, they are less suitable for the study of new, unconventional designs.

3.3.3. AN ANALYSIS OF 3D FULLY-MODELED APPROACHES

Fully-modeled approaches have the potential to greatly reduce the numerical cost related to flow simulations involving VGs, however, little information is available regarding their general performance. They are typically validated for specific cases which fall within the parameter range used to derive their included empirical relations. To date no studies have been found that yield a conclusive comparative analysis of different fully-modeled approaches.

To provide further insight, a study performed in collaboration with Ana Sofia Moreira Ribeiro is presented here, in which a fully-modeled approach is applied to a test case that falls outside its validated range. This case is selected such as to be representative for a typical VG configuration as used for flow control of external aerodynamics applications. It considers the subsonic flow over a counter-rotating common-down VG array attached to a flat plate, corresponding to the experimental set-up of Baldacchino et al. [9] and in line with the VG configuration design guidelines formulated by Godard and Stanislas [31]. A detailed discussion of this test case, as well as the body-fitted mesh simulations that are used as reference, appears in section 4.4.2.

A 3D fully-modeled approach is used in order to include the necessary physics to expect a sufficiently accurate representation of the vortex paths. Moreover, we desired to include the effect of the vortex as a mean-flow feature (supported by the evidence of [103]) within a RANS simulation. The fully-modeled approaches proposed by Liu et al. [58], May [63] and Dudek [20] all satisfy these requirements. In this work, it was chosen to represent the vortex profile as an artificial boundary condition using the approach of Dudek.

APPLICATION OF DUDEK'S VG-MODELING APPROACH FOR A SAMPLE CASE

The VG-modeling method proposed by Dudek [20] was implemented in the open-source CFD code OpenFOAM®. This method makes use of Wendt's semi-empirical vortex description, describing the secondary velocity profile induced by the presence of a VG as a Lamb (ideal viscous) vortex, as function of the vortex's total circulation (Γ) and peak vorticity ($\omega_{x,\max}$). The model assumes the center of the vortex that is imposed to the undisturbed flow field to be located at the same coordinate in wall-normal and cross-flow direction as the VG tip, but at one VG chord length downstream of the VG's trailing edge. Our implementation has been verified against the pipe-flow case discussed in [20] (see [67] for more information).

The chosen VG-flow case of [9] falls partly within and partly outside the parametric range considered by Wendt; the freestream velocity is significantly lower and the VG incidence angle slightly larger than the validated range of the model. For our assessment, Dudek's modeling approach is compared to both experimental data and a body-fitted mesh (BFM) RANS simulation. Details of the latter can be found in section 4.4.2. In order to eliminate mesh-related differences the mesh for the fully-modeled simulation, downstream of the VG location, was equal to that of the body-fitted mesh. Also the same numerical schemes were used for both simulation approaches.

Our results indicate that the considered fully-modeled approach yields unreliable results in the sense that the initial circulation and decay rate are underestimated, while the vortex shape and position show large deviations. Figure 3.2 shows the total circulation levels downstream of the VG (with $\Delta x/h = 2.5$ corresponding to $\Delta x = l$, the location where the vortex profile is imposed). The Q-criterion was used to identify the vortex domain, as in [9]. Peak vorticity levels are shown in figure 3.3, and vorticity-contour plots at three locations downstream of the VGs in figure 3.4.

It is observed that Wendt's circulation approximation yields a significant underestimation for our test case, thereby suggesting that use of this model outside its calibrated range is not advised. The same figure also indicates that, contrary to both experimental and BFM results, the created vortices only start decaying after approximately 15 VG heights. This can be attributed to their large distance from the wall and small size (figure 3.4), both of which minimize the interactions with the viscous layer near the wall. Sufficiently far downstream, the total circulation level and decay rate agree well with the reference data. The underestimated vortex circulation is thus likely counteracted by errors with respect to size and location.

Furthermore, our results indicate a rather good result for the peak vorticity, and hence the intensity of the created vortices. Although initially being overestimated with respect to the BFM result, good agreement with the experimental data is obtained downstream. The peak vorticity displays a rapid decay, in combination with fast growth of the vortex core, thereby again approaching the BFM results further downstream. However, despite good results with respect to circulation and peak vorticity far downstream, the deviations with respect to the shape and location of the vortices make predictions of the boundary-layer state questionable, as both the vortex-vortex and vortex-boundary layer interactions can be expected to be erroneous. Moreover, it cannot be relied upon that for all applications the initial errors of the model will be reduced with the convection of the vortices.

EFFECT OF PARAMETER CALIBRATION

To explore the effect of parameter errors on the accuracy of Dudek's fully-modeled approach, simulations were performed with calibrated values for the circulation, peak vorticity and location of the vortex center. Due to the large error with respect to the initial total circulation, the effect of improving this parameter is of key interest. In Wendt's model, however, peak vorticity scales with the circulation cubed. Since in the original model underestimated circulation corresponds to an overestimation of the peak vorticity, it was expected that an increase of Γ would yield an unrealistic value for $\omega_{x,\max}$. Therefore the initial peak vorticity was calibrated simultaneously with the circulation.

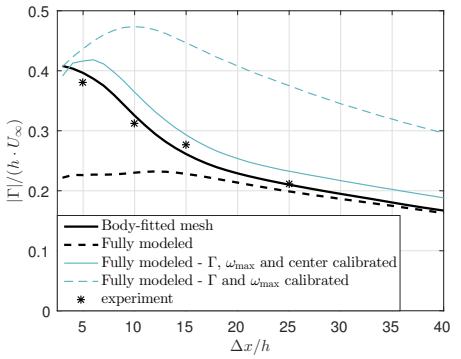

Figure 3.2: Total circulation levels corresponding to one of the vortices created by a counter-rotating VG pair on a flat plate, using a.o. Dudek's fully-modeled simulation method.

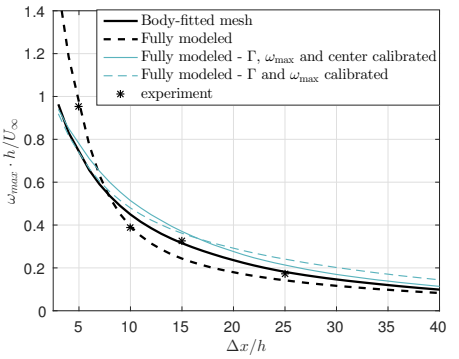

Figure 3.3: Peak vorticity values downstream of a counter-rotating VG pair on a flat plate, using a.o. Dudek's fully-modeled simulation method.

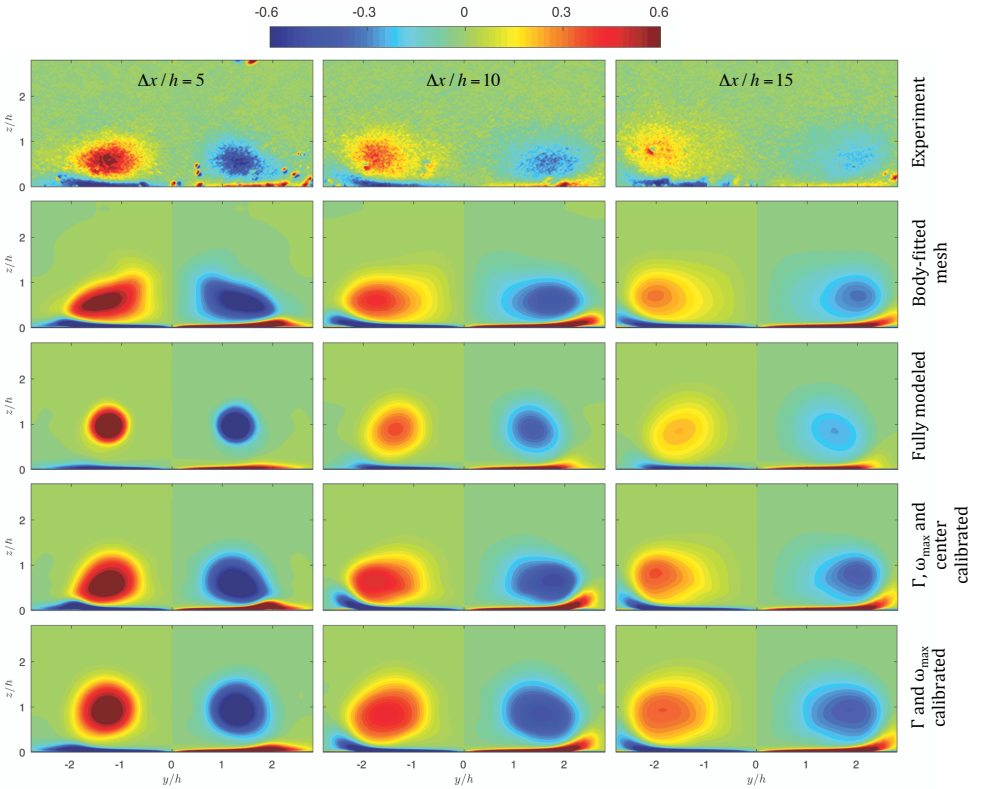

Figure 3.4: Streamwise vorticity ($\omega_x \cdot h/U_\infty$) contours at three locations downstream of a counter-rotating VG pair on a flat plate

This was done by using the values for Γ and $\omega_{x,\max}$ at $\Delta x = l$ as obtained from the BFM simulation, instead of Wendt's semi-empirical relations.

The results in figures 3.2, 3.3 and 3.4 indicate that improved estimates for the shed vortex's circulation and peak vorticity are not in themselves sufficient to improve the reliability of the simulation result. The simulated vortex remains too circular and too far from the wall compared to the reference results. This yields an initial increase in total circulation, until the vortex has grown sufficiently for the viscous interaction to start the vortex decay. As a result, the total circulation, and therefore the mixing caused by the vortex, is overestimated for the entire downstream range, despite the initial calibration.

The above observations suggest that an improvement of the initial location of the vortex center would have a large beneficial effect on the obtained simulation result. Dudek's approach implicitly assumes that the center of the created vortex does not move until at least one VG chord length downstream, the distance after which the vortex is assumed to be fully developed. However, research by, for example, Lögdberg et al. [59] indicates that this is not the case, and that for a counter-rotating common-down VG pair the vortices immediately start moving apart and towards the wall.

Indeed, additional calibration of the vortex center location based on the BFM result induces an improved simulation result. Due to the close proximity of the wall, the initial vortex is no longer circular and interaction with the viscous layer causes immediate vortex decay. The resulting total circulation and peak vorticity levels are therefore in close agreement with the BFM result, as are the location and (to a lesser extent) the shape of the generated vortices.

Overall, this test of Dudek's fully-modeled approach indicates that problems can be expected with this type of fully-modeled approach due to its sensitivity to input parameters. Our results show that great care should be taken when using semi-empirical models outside their calibrated range, and that detailed knowledge of the vortex location at the position where the vortex profile is imposed is crucial for a realistic downstream evolution. The latter is hard to achieve without a detailed viscous analysis, and thus appears to limit the usefulness of this type of approach.

3.4. PARTLY-MODELED / PARTLY-RESOLVED SIMULATIONS

3.4.1. OVERVIEW

In an attempt to enhance the connection between the vortex and the situation of interest, an intermediate approach can be used that relies on simplified physics in order to partly model the vortex-formation process. In this case a vortex is created within the simulation, making no prior assumptions on its characteristics, but without fully resolving the complex flow around a VG. Instead, an external forcing is locally added to the simulation which triggers the formation of a streamwise vortex similar to the main vortex created by the VG. Because in this case the vortex is formed within the simulation, a finer mesh is required compared to the fully-modeled approaches. However, since no attempt is made to resolve the VG's boundary layer, and because secondary vortices are neglected, the mesh is relatively coarse compared to the fully-resolved simulation approach.

This medium-fidelity, partly-modeled/partly-resolved, approach was pioneered by

Bender et al. [11], who developed the popular BAY model. This model in essence replaces the VG by the reaction force its presence would impose on the flow, thereby introducing an acceleration in crossflow direction which evolves into a streamwise vortex. This model, either in its original form or using the modification proposed by Jirasek (the so-called jBAY model) [41], is often used in industry [21, 30, 47], allowing for reported mesh-size reductions of 60% - 70% relative to fully-resolved RANS simulations [21, 41]. A more detailed discussion of these models follows in section 3.4.2.

The flow-tangency model proposed by Wallin and Eriksson [112] constitutes another example of this simulation approach. In this model, volume forces are applied such that upon steady-state convergence, flow tangency is satisfied at the virtual VG surface. To accomplish this, flow tangency at the virtual VG is linked to the rate of change of the local normal body forces, yielding a body force equation that is to be solved simultaneously with the RANS equations.

More recently, Poole et al. [79] used a partly-modeled/partly-resolved approach based on the same philosophy as the BAY model. An estimate for the VG's resultant force was added to the momentum equation in the form of an acceleration, enforcing the creation of a streamwise vortex. Their estimate for this resultant force was based on the circulation as calculated using the modified lifting-line method presented in the same work. Moreover, the induced drag component was also explicitly taken into account.

3.4.2. THE BAY AND JBAY MODELS

As both the BAY-model and its successor the jBAY-model have been widely adopted by industry, here a closer look is taken at the details of their performance.

MODEL DETAILS

The BAY model was proposed by Bender et al.[11] in 1999, and since then has been widely implemented in CFD codes, see for example [21, 111]. The model mimics the effect of VGs on the flow by substituting the VG geometry by a volume force, which is representative for the side force (lift force) generated by the VG being modeled. This lift force is locally approximated as

$$\mathbf{f}_i = cA\frac{V_i}{V_{tot}}\beta\rho|\mathbf{u}_i|^2\mathbf{l}, \tag{3.7}$$

where A is the VG planform area, V_i/V_{tot} is the ratio of the cell volume to the total volume of cells where the source term is applied, ρ is the fluid density and $\mathbf{u}_i$ the local flow velocity. The local lift force is assumed to be normal to both the local flow and the span of the VG, hence the direction $\mathbf{l}$ is

$$\mathbf{l} = \frac{\mathbf{u}_i}{|\mathbf{u}_i|} \times \mathbf{b}. \tag{3.8}$$

Moreover, the angle of incidence of the VG with respect to the incoming flow is assumed small, such that

$$\beta \approx \sin\beta = \cos\left(\frac{\pi}{2} - \beta\right)\frac{\mathbf{u}_i}{|\mathbf{u}_i|} \cdot \mathbf{n}. \tag{3.9}$$

Additionally, a factor

$$\frac{\mathbf{u}_i}{|\mathbf{u}_i|} \cdot \mathbf{t} \tag{3.10}$$

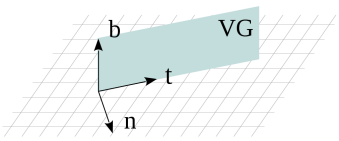

Figure 3.5: VG orientation vectors.

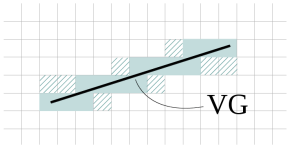

Figure 3.6: Typical cells where the source term can be applied. For the jBAY model, both fully colored and striped cells are used.

is included to account for the loss of side force at high incidence angles. In the above, **n**, **b**, and **t** are unit vectors defining the direction (respectively normal, spanwise and tangential) relative to the VG, as indicated in figure 3.5. When combining expressions 3.7 to 3.10, the BAY-model formulation

$$\mathbf{f}_i = cA\frac{V_i}{V_{tot}}\rho\left(\mathbf{u}_i\cdot\mathbf{n}\right)\left(\mathbf{u}_i\times\mathbf{b}\right)\left(\frac{\mathbf{u}_i}{|\mathbf{u}_i|}\cdot\mathbf{t}\right) \tag{3.11}$$

is obtained. Local addition of the side force formulation (3.11) to the discretized governing equations results in a source-term distribution similar to the force distribution over an airfoil, with the applied forcing being strongest near the leading-edge location of the VG.

Note that (3.11) also contains a constant c which to some extent can be used to calibrate the strength of the source term. In [11] it was suggested to calibrate this value based on the desired integrated crossflow kinetic energy at a chosen location. For large values of c, the model operates in an asymptotic mode, where the flow becomes independent of this constant [11, 47, 111]. If this happens, the VG source term becomes the dominant term in the governing equations and the flow aligns itself with the orientation of the VG, thus enforcing flow tangency to the virtual VG and thereby allowing the momentum equation to maintain equilibrium. To ensure this behavior, in general a value of $c > 10$ is advised independent of the volume the model is applied to.

Furthermore, the BAY model depends on the volume of the cells where the source term is applied (V_{tot}). Originally, Bender et al. [11] proposed defining the region where to apply the source term (Ω_{VG}), and hence V_{tot}, by selecting several rows of cells near the VG, the amount of which could be used for additional calibration of the model. In [11], it was proposed to perform this calibration based on the crossflow kinetic energy. This of course requires the availability of suitable calibration data, and it should be done for every mesh considered. Due to the inconvenience of this approach, later methods have proposed selecting the cells which overlap the geometry of the VG, and distributing the source term based on the distance between the cell center and a virtual zero-thickness VG plane[41, 104]. Another reported modification of the BAY model consists of replacing the volume-scaling term in (3.11) by the VG surface fraction that is actually contained within the particular cell [104].

Of the reported BAY-model modifications, the jBAY model proposed by Jirasek [41] is the most widely used. This model reduces the dependence on c and V_{tot}, thereby simplifying the use of the model and the selection of cells where to apply it. Jirasek proposed selecting the cells aligned with the virtual VG plane, such that there is always one cell

center positioned at each side of the VG mean surface (see figure 3.6). Instead of using the velocities at the cell centers, the jBAY model calculates the body force using the interpolated velocity at the intersections of the (virtual) VG surface with the grid edges. The resulting local source term is then distributed over the surrounding cells. This interpolation process keeps the location where flow tangency is enforced consistent, such that the jBAY model can be expected to have improved accuracy and reduced grid dependence compared to the original BAY model.

REPORTED PERFORMANCE

The BAY and jBAY models have been adopted and implemented in several CFD codes, see for example [21, 25, 47, 111]. This widespread use allows for a good overview of the performance of this partly-modeled/partly-resolved simulation approach to be obtained from literature.

Most fundamental studies so far have been performed for a single VG on a flat plate in a zero-pressure-gradient (ZPG) flow [14, 21, 61, 111]. Overall, the obtained results show a consensus in the observation that both models underestimate the streamwise peak vorticity, and thereby the intensity, of the created vortex, when compared with both body-fitted mesh simulations or experimental data. This behavior is reported for varying mesh resolutions and regions of application, thereby identifying this underprediction as a weakness inherent to the model. This may be partly due to the absence of VG friction forces in the BAY and jBAY models, as it was shown in [21] that body-fitted mesh simulations with the VG walls modeled as being inviscid produce similar velocity contour plots as the BAY model.

Less agreement is found between the results with respect to the comparison of the vortex's shape, trajectory, total circulation and decay rate with reference data. Waithe [111] used the original BAY model and calibrated the model based on experimental data by varying the number of selected rows of cells where the model is applied. For a single VG on a flat plate, the results seem to indicate a reasonably good agreement in shape, lateral trajectory and total circulation of the modeled vortex. Deviations were observed for the vortex's decay rate (which was lower) and the wall-normal location of the vortex center (which was further away of the wall). For a pair of counter-rotating VGs, on the other hand, the results obtained with the BAY model by Brunet et al. [14] indicated that it created vortices that were not only less intense, but also more diffuse than those of the body-fitted and experimental references. Moreover, discrepancies in both shape and lateral trajectory were observed, with the modeled vortices being closer together than the reference.

For airfoil applications, analysis of BAY/jBAY-model results shows that in general reasonable agreement in the pressure distribution can be obtained [41, 61]. However, for airfoils at an angle of attack close to stall, the predictive capabilities of the model fail, as large spreads in the aerodynamic coefficients are obtained [8, 47, 61]. This results in a large uncertainty with respect to both the stall angle and the maximum performance that can be expected upon application of a BAY-like model to a particular VG configuration.

Overall, the results from literature seem to indicate that the reliability of BAY-model results heavily depends on both mesh resolution and calibration. With respect to mesh resolution, however, no conclusive studies can be found that analyze the mesh require-

ments for specific objectives. In [21], a lateral mesh resolution corresponding to approximately $0.2h$ is used, however, it is unclear whether this resolution is generally sufficient, regardless of the specific objective of the simulation.

As mentioned in the original work of Bender et al. [11], calibration seems to be essential in order to obtain the correct amount of flow mixing. To a certain extent this can be done through the constant c, however, the total cell volume V_{tot} in which the model is applied has an equal or even larger influence on the total circulation [11]. In practice, calibration is often not possible due to a lack of available reference data. Therefore the BAY model is usually used without calibration, for example by simply selecting the cells that correspond to the actual VG position [14], or by selecting a rectangular domain that encloses the VG [21]. Use of the jBAY model should eliminate the need for calibration [41], however, studies that identify the impact of cell selection (and hence V_{tot}) are lacking. The influence of a certain cell-selection approach on the reliability of the simulation result has thus not been demonstrated, nor has it been shown that the jBAY model does indeed not require calibration.

This literature survey indicates that there seems to be insufficient knowledge with respect to the performance of BAY-like models in order to predict the reliability of simulation results for specific objectives. It remains unclear how a specific source term affects the downstream flow field. Moreover, an understanding of the impact of mesh resolution and the cell-selection approach on the obtained flow field is required to obtain reliable results. Further research comparing the original BAY model and the jBAY model, thereby assessing the expected performance improvements of the jBAY model, is also desired.

3.5. CONCLUSION

In this chapter the results of a literature survey towards different prediction methods with various levels of fidelity were presented. From an accuracy point of view, fully-resolved (body-fitted mesh) CFD simulations are the method of choice. Unfortunately, time-resolved simulations, like DNS or LES, come at a computational cost that normally prohibits their use for industrial applications. For high Re-number flows, body-fitted mesh RANS simulations are therefore the standard when high-fidelity results are required. When using RANS, however, care should be taken in choosing the turbulence model and interpreting the obtained results, as not all models are able to accurately represent the interactions between the created vortex and the turbulent eddies. Moreover, body-fitted mesh simulations impose a large computational cost since locally very dense meshes are required to fully resolve the VG's boundary layer and the associated small-scale flow structures. Apart from the large computational effort involved, the creation of a suitable mesh can be a complex task. As an alternative to body-fitted mesh simulations, the immersed-boundary method can be an option, as it eliminates the tedious task of mesh generation. However, the same limitations with respect to mesh resolution (and therefore computational cost) are still present.

On the other end of the spectrum, low-fidelity analytical methods have been proposed that, due to their low computational cost, can be of use as a quick assessment tool in initial design phases. These methods mainly attempt to approximate the properties of the initial shed vortex. However, their low complexity implies that some fundamental physics, like 3D and viscous effects, are neglected. These methods are therefore unreli-

able for predictions with respect to the subsequent evolution of the vortices, i.e. their decay and interactions. Moreover, the assumptions made during the formulation of these models strongly limit their range of applicability.

Fully-modeled CFD approaches basically attempt to extend an analytical initial vortex description with the ability of CFD codes to simulate the downstream convection. Both 2D and 3D approaches have been proposed, typically imposing the analytical vortex profile as a source term in either the mean flow or turbulence equations. In general, qualitatively good results are reported for these type of approaches, however, quantitative accuracy is less reliable and usually requires calibration. The application of a fully-modeled approach shown in this work, illustrated the sensitivity of this modeling approach to its input parameters. Limitations with respect to the range of applicability therefore also apply here. Moreover, our sample test case suggested that accuracy with respect to the location of the vortex center is especially important, the accurate prediction of which requires 3D and viscous effects to be taken into account.

The category of partly-modeled/partly-resolved simulation methods has the potential of being an effective intermediate solution between the expensive fully-resolved and the very specific fully-modeled approaches. These simulation methods make use of a model in the form of a local source term to trigger the formation of a suitable vortex. Hence, the smallest-scale flow features are not accounted for, but the creation and propagation of the primary vortex is resolved. By eliminating assumptions with respect to the shape, location and strength of the created vortex, these methods are in theory applicable to a wide variety of flow situations. A literature survey has, however, revealed a lack of validation for currently available methods. The effects of mesh resolution and model parameters on the quantities of interest, are insufficiently understood at this moment.

There thus seems to be a need for a study towards the strengths and limitations of partly-modeled/partly-resolved simulation methods, and for the identification of key parameters that determine their performance. This is of importance for an optimal use of these methods, and the correct interpretation of their results. Moreover, only when the effect of specific parameters is clear, can one aim towards the development of model adaptations which achieve improved accuracy-to-cost ratios. Performing such a study is the objective of this thesis. The present study focuses in the first instance on the current industrial standard in this respect, the BAY and jBAY models. Afterwards, we move on to a more general study of the partly-modeled/partly-resolved modeling concept, and perform a first exploration towards the improvement of these methods.

4

DESCRIPTION OF STUDY

Following the overview of the current state of the art in the field of VG design and simulation methods (chapters 2 and 3), this chapter lays the foundation for our study towards effective partly-modeled/partly-resolved source-term models which include the effect of VGs in CFD simulations. To allow for an effective study, the chapter starts with the identification of the quantities that are of interest when performing simulations of VG-induced flow fields. This is then followed by the outline of our research approach, where the applied methodology in section 4.3 is preceded by the definition of our scope (section 4.2), including an overview of the errors related to source-term CFD simulations. The current chapter concludes with an overview of the test cases that are considered for the assessment of VG source-term modeling approaches, as presented in the following chapters, including the presentation of the body-fitted mesh simulation results that will be used for reference.

4.1. QUANTITIES OF INTEREST IN THE STUDY OF VG-INDUCED FLOWS

Before assessing the quality of models for simulating VG-induced flow fields, one must determine suitable measures and physical quantities that allow insightful analysis. In general, distinction can be made between (i) a study of the main vortex generated by a VG, and its downstream evolution, and (ii) an analysis of the effect mixing, due to this vortex, has on the mean flow and the state of the boundary layer.

In both cases, snapshots of the flow field allow for a quick visual, qualitative analysis. Here the primary and secondary mean-velocity components and the streamwise vorticity are of interest, as they show the disturbance of the boundary layer and the topology of the vortex that causes it.

Vorticity is defined as the curl of the velocity field,

$$\boldsymbol{\omega} = \nabla \times \mathbf{u}, \tag{4.1}$$

and can be interpreted as a measure of the level of rotation of the fluid particles. The streamwise component of the vorticity vector,

$$\omega_x = \frac{\partial w}{\partial y} - \frac{\partial v}{\partial z}, \tag{4.2}$$

therefore indicates the rotation in the crossplane (thus perpendicular to the propagation direction of the vortex) due to the secondary-velocity components induced by the presence of the VG.

Even though a visual analysis of the flow field can provide insight, a thorough quantitative assessment remains indispensable. The quantities used for this purpose are described below.

4.1.1. SCALAR DESCRIPTORS OF VORTEX PROPERTIES

In their study of the interaction between a vortex and a turbulent boundary layer, Westphal et al. [116] identified the main descriptors that allow for a quantitative characterization of vortex properties as being the strength, position, and size of the vortex. These parameters originate from the secondary-velocity field and are generally used in the study of VG effects [7], although their definition and calculation can change between studies.

Both the absolute value of the overall circulation and peak vorticity are measures typically used to quantify the vortex strength. The peak vorticity $\omega_{x,\max}$ is the peak value of the streamwise vorticity field created by the vortex in a plane downstream of the VG, and is attained in the core of the vortex. This quantity gives an indication for the intensity of the vortex and rapidly attenuates downstream of the VG. Determination of $\omega_{x,\max}$ is straightforward, but mesh dependent. If the mesh resolution is insufficient near the vortex core, the peak cannot be resolved and $\omega_{x,\max}$ will be underestimated. In the current work, $\omega_{x,\max}$ is therefore determined as the peak value after performing a spline surface fit.

The absolute value of the total circulation $|\Gamma|$ is best suited to assess the overall flow circulation created by the vortex, and therefore the amount of mixing in the flow. Circulation is a scalar integral quantity that is a measure for the rotation in a domain of the fluid, typically calculated as the surface integral of the vorticity field,

$$\Gamma = \oint_{\mathbf{l}} \mathbf{u} \cdot \mathrm{d}\mathbf{l} = \int_S (\nabla \times \mathbf{u}) \cdot \mathrm{d}S = \int_S \omega \cdot \mathrm{d}S. \tag{4.3}$$

Circulation is defined in this work as the integral of only the positive streamwise vorticity due to the primary vortex, thus including only a single vortex and excluding the layer of negative vorticity occurring close to the wall in these flows. Determination of the domain over which to perform the integration is not straightforward, as a vortex is typically smeared out and therefore no clear boundary can be defined. Several approaches to determine S have therefore been proposed in literature. In [116] the vortex domain S consists of the region where $\omega_x > 0.1\,\omega_{x,\max}$, thus neglecting the region with lowest vorticity where the uncertainty of the results is largest. This filtering is not applied in [1, 119], where the entire positive streamwise vorticity field is considered. Other options for identifying coherent vortex structures can be found in [40], where the λ_2- and Q-criteria were found to be the most accurate. The λ_2-method bases the detection of the vortex core on

the eigenvalues of the velocity gradient tensor, whereas the Q-criterion defines the vortex core as the connected fluid region with a positive second invariant of the velocity gradient tensor, and is for example used in [9]. Still, a vortex-core definition based on a cut-off vorticity level is encountered most often in literature, e.g. [47, 62, 115]. In this work we therefore chose to use the ω_x approach of [116].

A final measure related to the vortex strength consists of the rate with which it decays as the vortex convects downstream. Due to the nature of the decay process, this can be visualized as $\ln(|\Gamma|/|\Gamma_{\text{ref}}|)$, the natural logarithm of the ratio between the circulation and a reference value, the latter typically corresponding to the maximum circulation that is achieved closely downstream of the VG's trailing edge.

Another important measure used to characterize the vortex created by a VG is the position of its core, which allows the study of the trajectory of the vortex as it propagates in the flow and hence to assess whether or not the vortex remains sufficiently close to the wall. Determination of the position of the vortex core is typically based on the vorticity field. In [116] it was determined as the geometric center of the concentric vorticity contours. However, as vortex cores approach a surface they rarely remain concentric. Considering that the peak vorticity is attained in the vortex core, a more practical approach consists of defining the vortex center as

$$(y_c, z_c) = \arg\max_{y,z} \omega_x(y,z), \tag{4.4}$$

with for ω_x the spline surface fit, hence as the location where the peak vorticity is found.

Finally, a length scale can be determined to quantify the size of a vortex. Often the edge of the vortex within a cross plane is considered to be the half-life contour, determining the location where the streamwise vorticity has halved compared to its peak value. As in general vortex cores are not circular, due to the interactions with each other and the wall, this measure is ambiguous and different length scales have been proposed in literature. For example, Yao et al. [119] defined the vortex radius as the average of the half-life distances in lateral and wall-normal direction. Westphal et al. [116] reported the vortex radius in both these directions separately and, based on this, also defined an ellipticity ratio as $e = R_y/R_z$ to indicate the level of flattening of the core. Another approach was proposed by Ashill et al. [7], who quantified the scale of the vortex by calculating the radius of an equivalent (circular) Rankine vortex based on the vortex strength parameters.

In this work we suggest the use of an alternative quantification of the vortex size, which is based on the area A_S of the region S in (4.3), used for the overall circulation calculation. To prevent a quadratic growth of this parameter with vortex size, we define a vortex radius R as

$$R = \sqrt{\frac{A_S}{\pi}}, \tag{4.5}$$

the radius of an equivalent circular vortex with the same area.

4.1.2. QUANTIFYING THE EFFECT OF MIXING ON THE BOUNDARY LAYER

The analytical, fully-modeled and partly-modeled/partly-resolved approaches discussed in section 3 do not attempt to accurately reproduce the physics related to vortex formation around a VG. Therefore assessing their performance based on the vortex descriptors

identified above may not be the optimal approach. Since the goal of these models consists of reproducing the effect the VG has on the mean flow, it is desirable to quantify the effect of mixing on the boundary layer. A study of integral boundary layer parameters, for example δ^*, θ and H, is suitable for this purpose [48, 86].

The displacement thickness δ^* is defined based upon the boundary-layer's velocity profile as

$$\delta^* = \int_0^\delta \left(1 - \frac{\rho U(z)}{\rho_\infty U_\infty}\right) \mathrm{d}z, \tag{4.6}$$

with z the wall normal coordinate, and is a length parameter which reflects the distance through which the external inviscid flow is displaced by the presence of a boundary layer [4]. Enhanced mixing, for example by the presence of a streamwise vortex, causes the momentum loss being more evenly distributed throughout the boundary layer, resulting in a reduction of δ^*.

In addition, the momentum thickness θ is a measure of the amount of momentum lost by the flow due to the presence of a viscous boundary layer [86]. This quantity is defined as

$$\theta = \int_0^\delta \frac{\rho U(z)}{\rho_\infty U_\infty} \left(1 - \frac{U(z)}{U_\infty}\right) \mathrm{d}z. \tag{4.7}$$

Enhanced flow mixing in this case thus yields an increase in θ, since fluid particles with a higher momentum are transported toward the wall.

The analysis of both above measures can be combined by considering the shape factor H. The shape factor serves as an important indicator for the boundary-layer's susceptibility to separation and is defined as the ratio between the boundary-layer displacement and momentum thicknesses,

$$H = \frac{\delta^*}{\theta}. \tag{4.8}$$

The introduction of a streamwise vortex into the flow causes a decrease in δ^* and an increase in θ, thus reflecting in a reduced value for H. Low values for H therefore typically indicate an attached boundary layer, whereas (in general) for $H > 4$, the flow is separated from the surface. As H thus is a primary indicator for the tendency of a boundary layer to separate, and delay of boundary-layer separation is the primal role of VGs, H is considered a key parameter when analyzing the performance of VG models.

4.2. RESEARCH SCOPE

4.2.1. FLOW CONDITIONS

VG's are found in a variety of applications, ranging from engine inlets to wind-turbine blades, thereby spanning a wide range of possible flow conditions. To limit the range of flow situations that require consideration in our study, this work is focused on external aerodynamics applications, where VGs are used as a passive flow-control mechanism to delay boundary-layer separation. Moreover, we limit our scope to incompressible and fully-turbulent flows. These are representative of wind-turbine applications, which constitutes the main driver for our research.

In this work the (steady) RANS equations in combination with a turbulent-viscosity model are used for the numerical simulation of the flows considered. This choice is

mainly supported by the moderate computational cost of RANS for the high-Re flow situations typically encountered when studying wind-turbine applications.

The steady-state assumption is justified by considering the large time-scale separation between the vortex motions and the overall motion of the structure on which the VGs are applied. For wind turbines, this difference is approximately 3 orders of magnitude. Quasi-steady inflow conditions are therefore realistic. This time-scale separation implies that consideration of only local mean-flow statistics suffices for studying the effect of VGs on the boundary layer.

4.2.2. SCOPE OF THE ANALYSIS

Several possible errors can be encountered when performing numerical simulations of VG-induced flow fields using a RANS approach in combination with a VG model. A reliable analysis of the results obtained with such simulations therefore requires a thorough understanding of the involved errors and their impact. Only this way the influence of a single component, in our study the VG model, on the accuracy of the simulation can be assessed. The main errors related to different simulation approaches are therefore visualized in the overview contained in figure 4.1, and discussed briefly below.

When translating real-life situations towards a numerical or experimental environment, approximations are inevitable. Examples include deviations due to truncation of the domain and statistical uncertainties in the inflow conditions. The former can in general be effectively minimized, by considering appropriate boundary conditions. However, it should be noticed that for simulations of VG arrays, considering only a single pair in combination with symmetry boundary conditions can result in the absence of some modes which could occur when a stall cell is present [61]. The effect of inflow uncertainties on the simulation, for example due to atmospheric-turbulence effects or

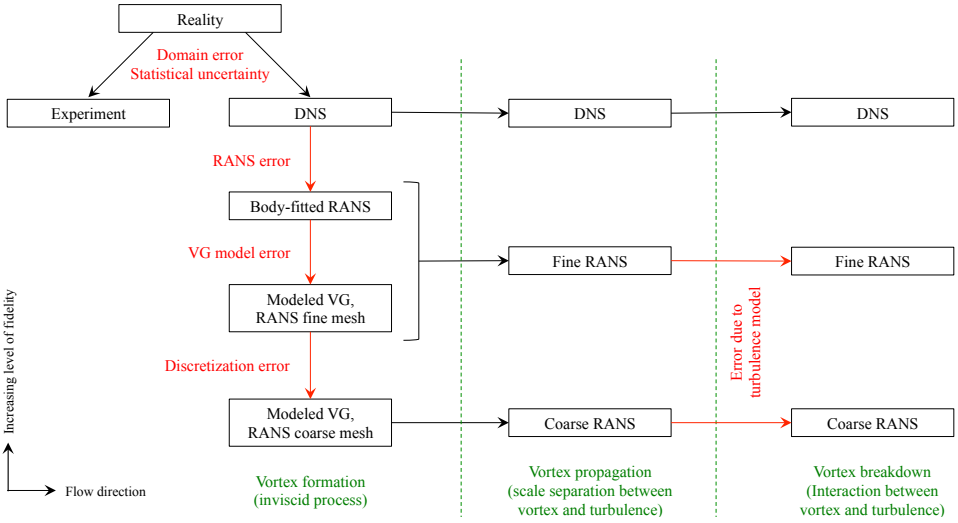

Figure 4.1: Overview of error sources (in red) related to the RANS simulation of wall-bounded flows over VGs. Black arrows indicate a theoretical lack of error.

variations in the fluid composition, falls within the research field of uncertainty quantification. These uncertainties are neglected in the current study.

The choice to use RANS instead of a fully-resolved transient CFD approach, like DNS, inevitably introduces an error in the boundary-layer development, and therefore in the initial condition of the vortex-development process. The significance of this error strongly depends upon the choice of turbulence model for the situation of interest. For example, in [16] a comparative study of 11 eddy-viscosity models showed that, even for simple flat-plate flow, deviations in skin friction coefficient ranging from −9% to 11% with respect to the experimental result can be expected. Furthermore, visibly large variations in the recirculation zone were observed for separated airfoil flow.

Moreover, the use of a model instead of a body-fitted mesh to represent the VG adds an error related to the vortex formation. This VG-model error is usually combined with a discretization error due to the use of an under-resolved mesh. Upon downstream convection of the vortex, another error source consists of the interaction between the created vortex and the turbulence model, since the latter is in general uncalibrated for such flow situations.

The aim of the current thesis is to study errors introduced to a steady incompressible RANS simulation when using a source-term model for simulating wall-bounded flows over VGs. Errors due to the choice of turbulence model are expected to have a considerable effect on the result but are outside our scope. Research by Spalart et al. [94] indicated that RANS errors are not dominant until a vortex starts aging. Our analysis therefore focuses on the flow profiles during the vortex formation and early propagation phase when there is still some separation between the vortex and the turbulence length scales. The evolution further downstream is considered to be outside the scope of this work, because it is governed by the interaction between the initial vortex and the turbulence model, and is thus dependent on the choice of turbulence model rather than the VG model.

4.3. METHODOLOGY

With our assessment of the partly-modeled/partly-resolved VG simulation approach we aim to improve both source-term model-specific and concept-related insights. To this end, we start from the study of a specific model, and by subsequently replacing part of the model by its calibrated equivalent, we move toward a general study of the hypothesis that a source term on a coarse mesh can yield sufficiently accurate results.

In the analysis of the BAY- and jBAY-model formulations, it is observed that errors of the model are expected to originate from two sources: from the selection of cells where the source term is applied (i.e., the geometry defining V_{tot}), and from the formulation used to compute the source term. Furthermore, practical use of these models generally

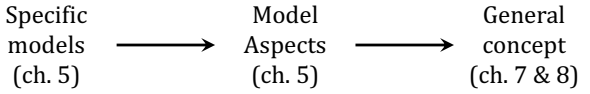

Figure 4.2: Research approach for our study of partly-modeled/partly-resolved source-term simulations.

happens in combination with a low-resolution mesh, thus also introducing a discretization error. The analysis of these models therefore includes (i) an assessment of the influence of the selected cells and the selected cell volume V_{tot}, (ii) a study of the sensitivity on different mesh-refinement levels in the neighborhood of the VG for the quantities of interest, and (iii) comparison of the BAY- and jBAY-model results against BFM data using identical numerical settings and a similar grid resolution, in order to minimize sources of error between both simulation types, other than the VG-model error.

To enhance the general understanding of the impact of a source term on the flow, this is then followed by an investigation of source-term characteristics with respect to their potential in altering the obtained flow field. In particular, the influence of the source term's total magnitude, direction and distribution are considered. In order to perform this assessment, several modified and/or calibrated source-term descriptions are formulated based on both the BAY model and the actual reaction force of the VG on the flow field (obtained from the BFM simulations). This study of the source term is performed on a fine mesh such as to minimize discretization errors.

As a final step it is investigated to what extent the general low-computational-cost combination of a low-resolution mesh with a source-term model has the ability to reproduce important flow-field characteristics. To this end, all physical considerations related to the source-term formulation are dropped, and an inverse approach is used to calculate the specific source term that, on a given mesh, represents best the objective flow field. This analysis allows to investigate both the highest accuracy achievable when using a source-term approach, and the characteristics of the 'ideal' source term.

The combination of these three analysis parts is expected to allow the formulation of recommendations regarding the use of partly-modeled/partly-resolved source-term approaches, and identifying promising directions for future developments.

Throughout this work, the quantities of interest obtained with a source-term VG model are compared against body-fitted mesh (BFM) simulation results obtained using the same numerical settings. Validation of the BFM results with respect to experimental data is included in order to ensure that the numerical results are in line with the physical flow field. Due to the presence of RANS turbulence-model errors, the experimental data are, however, not used to study the errors related to the VG model.

For the above presented analysis we focus, to a large extent, on the qualitative comparison of the flow topology close behind the VG, in the region where RANS errors are not yet dominant. Although there exists no formal definition of this region, based on results that are shown in the following sections (e.g. figures 4.9(b) and 4.9(c), which indicate excellent agreement between the BFM and experimental results in the considered domain), we believe that up to a distance of at least $15h$ downstream of the VG trailing edge, only a weak interaction between the vortex core and the largest turbulent length scales can be assumed. This is further supported by the observed scale separation of approximately one order of magnitude between the vortex radius and the turbulent mixing length. Flow-field snapshots and shape-factor (H) profiles are therefore studied in this region. Although the ultimate objective of the use of VGs is to delay flow separation, results concerning separation locations are not considered in this work, as these would include RANS turbulence-model errors, thereby making statements about the performance of VG models ambiguous.

All numerical results presented in this research are obtained with the open-source CFD package OpenFOAM®, which is a segregated finite-volume code able to solve both compressible and incompressible flows using either structured or unstructured grids. For the considered cases, the steady, incompressible RANS equations are solved using the SIMPLE algorithm, and the governing equations are solved on structured hexahedral grids using either first-order (the isolated VG test case, section 4.4.1) or second-order (the VG pair and airfoil test cases, sections 4.4.2 and 4.4.3) upwind discretization schemes for the convective terms. The linear systems arising from the equation discretization are solved using the preconditioned (bi-) conjugate gradient method with diagonal incomplete Cholesky and lower upper (LU) preconditioners for the symmetric and asymmetric systems, respectively. Closure of the RANS equations is provided by Menters $k-\omega$ SST turbulence model [64], ensuring dense near-wall meshes with the dimensionless wall distance $y^+ < 1$ to allow the viscous sublayer to be resolved.

4.4. TEST CASES

Our analysis is performed for three test cases, all simulating (rectangular) vane-type VGs, and considering both an isolated VG and counter-rotating pairs. The majority of the assessment is performed for a zero-pressure-gradient flow over a flat plate, after which, some findings are verified for a VG on an airfoil section. Below, an overview of the considered cases is presented. This includes the physical parameters, details about the used numerical meshes, and a presentation of the BFM simulation results that will be used as reference data for the remainder of this study.

Table 4.1: Configuration parameters (as defined in figure 4.3) defining the considered test cases as discussed in sections 4.4.1, 4.4.2 and 4.4.3.

Parameter	Symbol	Value		
		Single VG	VG pair	Airfoil
Freestream velocity	U_∞	34 m/s	15 m/s	24 m/s
Turbulence intensity	TI	1%	0.1%	0.2%
Boundary-layer thickness	δ	35 mm	15 mm	6 mm
Orientation	-	-	common down	common up
VG height	h	7 mm	5 mm	6 mm
VG (chord) length	l	$7h$	$2.5h$	$3h$
Inflow angle	β	16°	18°	20°
VG TE distance	d	-	$2.5h$	$3.7h$
Pair distance	D	-	$6h$	$11.7h$
Domain length	L	600 mm	600 mm	$100c$
Domain width	W	150 mm	30 mm	70.2 mm
Domain height	H	105 mm	75 mm	$100c$
Streamwise location VG	-	$14.5h$	$14.6h$	$0.3c$

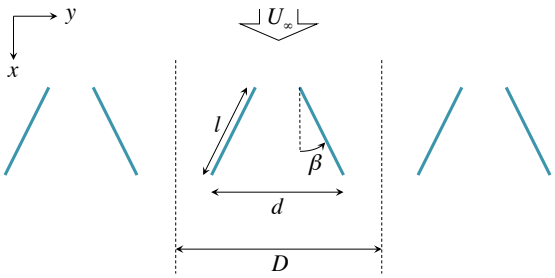

Figure 4.3: Illustration of a counter-rotating common-down VG-array layout and the corresponding parameters.

4.4.1. SINGLE VG ON A FLAT PLATE

DESCRIPTION

First the flat-plate experimental set-up as studied by Yao et al. [119] is considered, as it contains only a single VG and therefore excludes complex vortex-interaction effects. The aim of the work in [119] consisted of gaining a better understanding of the flow physics associated with VG-induced vortices within a turbulent boundary layer. For this purpose, stereo digital particle image velocimetry measurements were performed to provide an experimental database that contains flow-field data of embedded streamwise vortices downstream of an isolated VG on a flat plate. The database includes measurements for both submerged VGs, with $h = \delta/5$, and conventional VGs, with $h = \delta$, at different inflow angles.

For the current study, a submerged single VG was considered, using an inflow angle $\beta = 16^\circ$. The freestream velocity was 34 m/s, yielding a Reynolds number based on the momentum thickness of approximately $Re_\theta = 8160$. Moreover, as the flow field was tripped in the experiments, a fully-turbulent boundary layer (using a turbulence intensity of 1%) was assumed with a thickness $\delta = 35$ mm at the VG location. An overview of the VG configuration parameters is contained in table 4.1.

The dimensions of the numerical domain considered for the simulations in this work were chosen such as to be sufficiently far away from the embedded vortex to render insignificant effects due to the truncation of the domain. This was established by comparison of the shape-factor profiles downstream of the VG with the profiles as obtained on a twice as large domain, i.e. doubling the distance between the inflow boundary and the VG leading edge, between the VG trailing edge and the outflow boundary, between the VG trailing edge and the sides of the domain, and between the flat plate and the top boundary of the domain. An average variation in shape-factor profile of 0.2% was found, supporting the conclusion that the domain size as included in table 4.1 is sufficient.

For both the body-fitted and the uniform (used for the source-term simulations) meshes, a fully-turbulent inflow profile was specified to yield a boundary-layer thickness of $\delta = 35$ mm at the trailing edge of the VG. This inflow profile was obtained from a separate simulation for a clean boundary layer, using freestream values for the turbulent kinetic energy and specific dissipation rate of $k = 0.1734\text{m}^2/\text{s}^2$ and $\omega = 54.08/\text{s}$ respectively. Symmetry boundary conditions were specified for the side boundaries of the do-

main. At the top and outflow boundaries homogeneous Neumann boundary conditions were applied for the velocity and turbulence quantities, whereas for the pressure a Neumann condition was used at the top boundary and a Dirichlet condition at the outflow boundary. A no-slip boundary condition was applied at the wall surfaces, where a small wall-normal mesh spacing was used, ensuring $y^+ < 1$ for meshes M3 and M4 for both the flat plate and the VG surfaces. Mesh details are provided in table 4.2, and snapshots of the medium-density meshes are shown in figure 4.4. The meshes were constructed using the openFOAM® mesh-generation functionality blockMesh.

BODY-FITTED MESH SIMULATION RESULTS

BFM-simulation results are used as reference data for the analysis of source-term models, presented in the following chapters. To ensure the accuracy and mesh independence of this reference data, a mesh-convergence study was performed by varying the mesh size in the streamwise, crossflow and wall-normal directions. Four meshes were constructed this way (labeled M1 to M4 with increasing mesh resolution), using factor $r = \sqrt{2}$ refinements in each direction. More details with respect to these meshes can be found in table 4.2.

Richardson's extrapolation method [15, 85] was used to obtain a numerical approximation for the discretization errors, in order to verify mesh independence of the BFM solution. For a specific quantity of interest, in our case the shape factor H, the discretiza-

Table 4.2: Mesh details for the single VG on a flat plate test case, with N the total number of cells, N_s the number of cells in streamwise direction, N_c the number of cells in crossflow direction, N_n the number of cells in wall-normal direction and r_n the cell growth rate in wall-normal direction for the considered domain.

	BFM				Uniform		
	M1	M2	M3	M4	M1	M2	M3
N	0.5×10^6	1.2×10^6	3.3×10^6	8.9×10^6	0.3×10^6	1.2×10^6	4.9×10^6
N_s	228	323	456	644	150	300	600
N_c	60	85	120	170	38	75	150
N_n	27	38	54	76	54	54	54
r_n	1.40	1.26	1.17	1.12	1.17	1.17	1.17
y^+	2.07	1.04	0.50	0.25	0.50	0.50	0.50

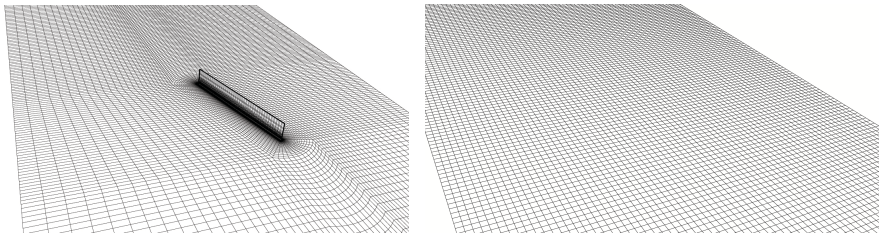

(a) BFM - M2 (b) uniform - M2

Figure 4.4: Snapshots of the meshes used for the BFM and source-term simulations for the submerged single VG case.

tion error for a discrete solution H_d can be estimated as

$$\epsilon_H = H_e - H_d, \tag{4.9}$$

with the unknown exact solution H_e estimated based on H_d as

$$H_e = H_{d1} + \frac{H_{d1} - H_{d2}}{r^{p_o} - 1}. \tag{4.10}$$

In the above, the subscripts $d1$ and $d2$ indicate discrete solutions obtained on a fine and coarse mesh respectively, and r represents the ratio of mesh spacings, $r = \Delta_{d2}/\Delta_{d1}$. In the presence of a third discrete solution, and if the mesh-spacing ratios between solutions $d1$ and $d2$, and between $d2$ and $d3$ are equal, the observed order of convergence can be deduced using

$$p_o = \frac{\ln\left(\frac{H_{d3} - H_{d2}}{H_{d2} - H_{d1}}\right)}{\ln(r)}. \tag{4.11}$$

The above method requires the used meshes to be in the asymptotic region of convergence, which can be assumed if the observed order of convergence is close to the expected value.

The observed order of convergence and discretization error estimates for H are presented in table 4.3, based on the numerical meshes specified above. These results were obtained by considering the domain downstream of the VG, from $\Delta x = 0$ to $\Delta x = 50h$, and subsequent averaging of the observed order of convergence and the error estimates in both crossflow and streamwise direction. Inspection of the observed order of convergence indicates a good agreement with the expected value of 1 (since a first-order upwind discretization is used). For meshes M2, M3 and M4 a small discretization error of less than 1% is observed.

Moreover, the circulation, streamwise peak vorticity and shape-factor profiles downstream of the VG are shown in figure 4.5. In these figures, four meshes are considered, M1 being characterized by the coarsest mesh resolution and M4 by the finest. Visual inspection of these results indicates flow-field convergence with increasing mesh resolution for all three quantities. From these results it is clear that the circulation result varies only very little with mesh refinement (0.9% between M3 and M4), whereas, as expected, the streamwise peak vorticity is much harder to resolve and thus varies visibly between the considered meshes (9.1% between M3 and M4).

All simulations presented in this work were converged up to (scaled) residuals of 1×10^{-4} for the velocity and turbulence quantities, and up to 5×10^{-4} for the pressure. A plot of the iterative convergence is included in figure 4.7. It was found that a reduction of the pressure residual by 5×10^{-4} corresponds to an average change in shape factor of only

Table 4.3: Observed order of convergence and shape-factor discretization errors for the BFM simulations of the single VG on a flat plate case, according to equations (4.9), (4.10) and (4.11).

	p_o	M2	M3	M4
ϵ_H	0.92	0.74%	0.57%	0.42%

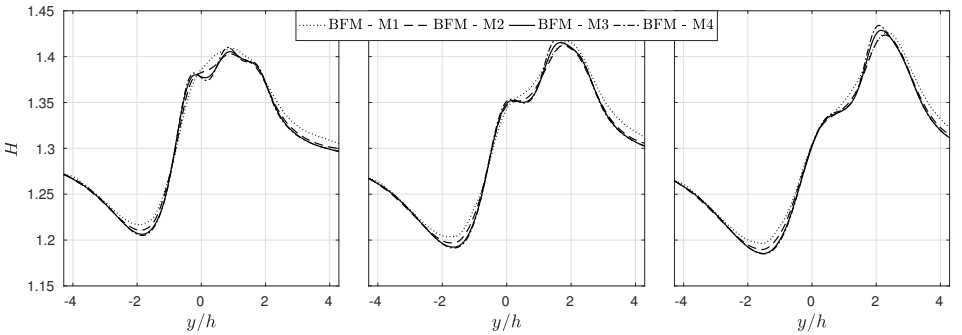

(a) Shape-factor profiles at $\Delta x = 5h$ (left), $\Delta x = 10h$ (middle) and $\Delta x = 15h$ (right) downstream of the VG.

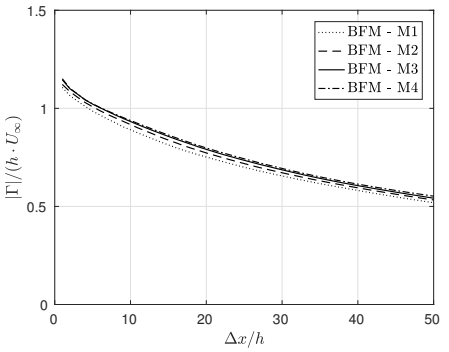

(b) Circulation

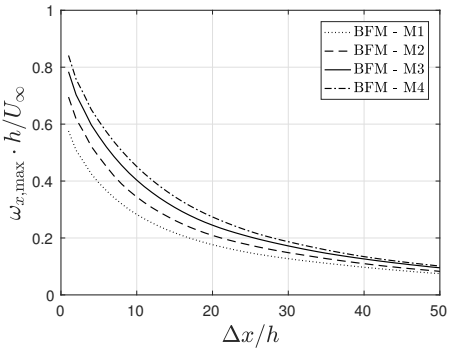

(c) Streamwise peak vorticity

Figure 4.5: Mesh convergence for the submerged single VG BFM simulations.

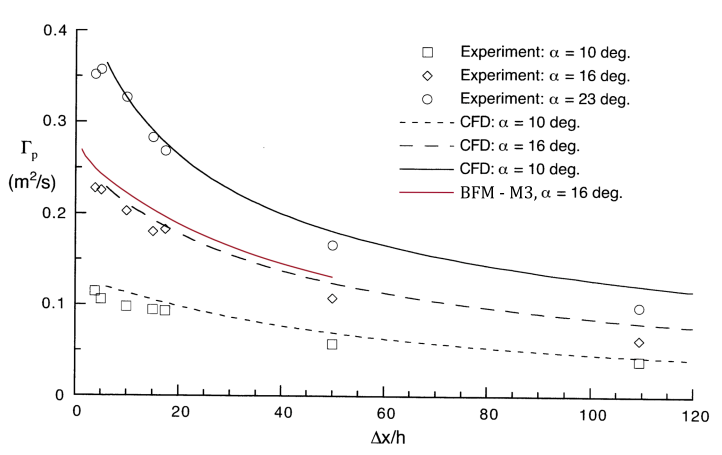

Figure 4.6: Comparison of circulation result (in red) with experimental and numerical results of [119], for the submerged single VG case.

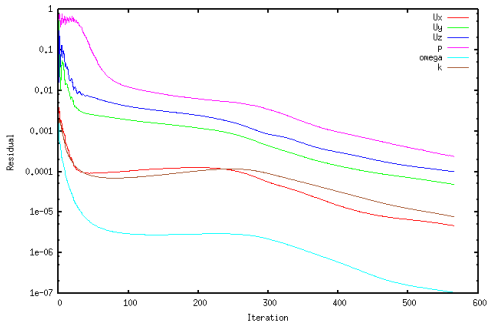

Figure 4.7: Iterative convergence for the BFM simulation of a single VG on a plat plate, for mesh M3.

0.01%. It was therefore believed that the used level of iterative convergence is sufficient to minimize the effect of iterative errors on the solution.

As a final validation, the flow circulation obtained using the BFM simulation on mesh M3 is compared with the experimental and numerical reference data presented in [119]. From figure 4.6 it follows that our result is in good agreement with the reference data, thus indicating the obtained flow field to be physical.

Based on these results it was concluded that mesh M3 is sufficiently fine to yield an accurate reference solution for the flow field downstream of the VG. The constructed uniform meshes, included in table 4.2 and visualized in figure 4.4(b), vary with respect to mesh resolution in streamwise and crossflow direction only. In wall-normal direction the same mesh resolution and growth rate as for the body-fitted mesh M3 were used, based on the notion that the required wall-normal mesh resolution is rather determined by the flat-plate's boundary layer than by the presence of the VG.

4.4.2. FLAT PLATE WITH SUBMERGED COMMON-DOWN VG PAIRS

DESCRIPTION

For a more advanced test case, which includes the interaction of multiple vortices, the flow over a flat plate with an array of counter-rotating, common-down, vane-type rectangular VG pairs is considered, corresponding to the experimental setup reported by Baldacchino et al. [9]. The experimental data were obtained for submerged VGs with a height of approximately $h = \delta/3$, in a flow characterized by a Re_θ of 2600. This configuration was designed based on the VG study of Godard and Stanislas [31]. An overview of the relevant numerical parameters is included in table 4.1, with an illustration of the parameters included in figure 4.3.

The numerical simulations were performed for one VG pair only, bounded by the dotted lines in figure 4.3, using symmetry boundary conditions in order to account for the effect of neighboring VG pairs. The applied boundary conditions are similar to the single VG case described in section 4.4.1. A fully-turbulent profile is specified at the inflow boundary, which is located at a distance of $14.6h$ before the VG's leading edges, to yield a boundary-layer thickness of $\delta = 15$mm at the trailing edges of the VGs. Freestream values of $U_\infty = 15$m/s, $k = 7.6 \times 10^{-4}\text{m}^2/\text{s}^2$, $\omega = 72.3$/s and a turbulence intensity of 0.1% were assumed.

The numerical domain size is defined in crossflow direction by the considered VG configuration. In streamwise and wall-normal direction the size of the numerical domain was based on the findings with respect to domain size for the single VG case in section 4.4.1, for which the dimensions were found to be sufficiently large to render insignificant effects due to the truncation of the domaim.

As for the previously discussed test case, body-fitted and uniform meshes were created using the openFOAM® mesh generator blockMesh. Meshes with varying resolution were used, all ensuring $y^+ < 1$ on the wall surfaces. For the flat plate surface, inflation layers are created in wall-normal direction using a cell growth rate of 16%. For this case the different body-fitted meshes were refined by a factor 2 in crossflow and streamwise direction only, as the used wall-normal resolution is widely accepted as sufficiently dense for 2nd order schemes. In the streamwise and crossflow directions the mesh resolution varies from $N_c = 16$ cells in crossflow direction per VG pair (corresponding to a mesh spacing of $\Delta \approx 0.4h$) for the coarsest uniform mesh (M0) to $N_c = 176$ cells for the finest body-fitted mesh (M3, see table 4.4). Snapshots of the BFM and uniform meshes are included in figure 4.8.

Table 4.4: Mesh details for the VG pair on a flat plate test case, with N the total number of cells, N_s the number of cells in streamwise direction, N_c the number of cells in crossflow direction, N_n the number of cells in wall-normal direction and r_n the cell growth rate in wall-normal direction for the considered domain of one VG pair (the distance D).

	BFM			Uniform			
	M1	M2	M3	M0	M1	M2	M3
N	0.4×10^6	1.6×10^6	6.4×10^6	0.3×10^6	1.2×10^6	4.6×10^6	18.4×10^6
N_s	278	556	1112	300	600	1200	2400
N_c	44	88	176	16	32	64	128
N_n	60	60	60	60	60	60	60
r_n	1.16	1.16	1.16	1.16	1.16	1.16	1.16
y^+	0.34	0.34	0.34	0.34	0.34	0.34	0.34

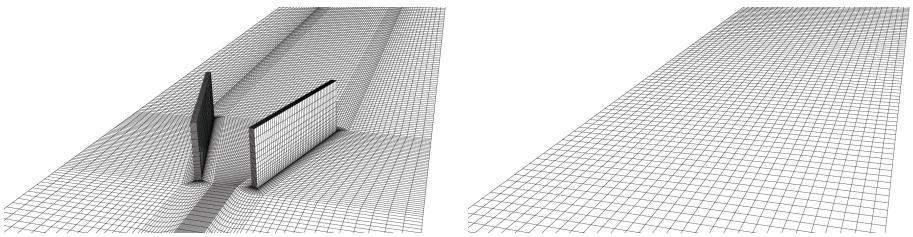

(a) BFM - M2 (b) uniform - M1

Figure 4.8: Snapshots of the meshes used for the BFM and source-term simulations for the VG pair test case.

BODY-FITTED MESH SIMULATION RESULTS

Mesh independence of the BFM solution that is used for reference in the remainder of this study was verified by performing simulations for varying streamwise and crossflow mesh resolutions. The BFM results were also validated using the experimental data from Baldacchino et al. [9].

Shape-factor results obtained with a BFM simulation with varying mesh resolution, as well as the total circulation and streamwise peak vorticity, are shown in figure 4.9. Visual inspection of these results indicates that a solution obtained on the finest mesh (M3) can be expected to be mesh independent, as the results on M2 and M3 are almost identical.

Table 4.5: Observed order of convergence and shape-factor discretization errors for the BFM simulations of the VG pair on a flat plate test case, according to equations (4.9), (4.10) and (4.11). ϵ_H represents the average in both crossflow (y) and streamwise (x) direction.

	p_o	M1	M2	M3
ϵ_H	2.0	0.8%	0.4%	0.3%

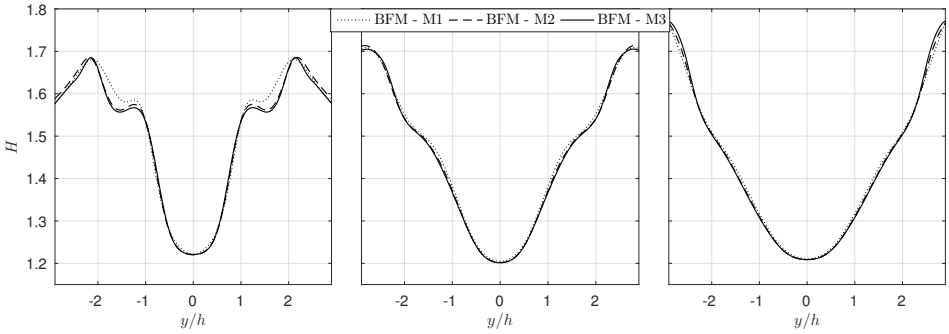

(a) Shape-factor profiles at $\Delta x = 5h$ (left), $\Delta x = 10h$ (middle) and $\Delta x = 15h$ (right) downstream of the VGs.

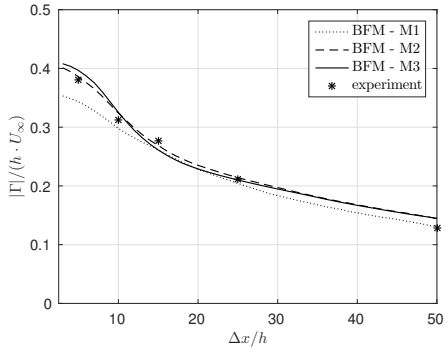

(b) Circulation

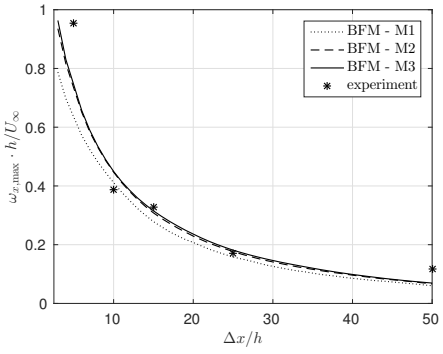

(c) Streamwise peak vorticity

Figure 4.9: Mesh convergence for the VG pair on a flat plate BFM simulations.

Still, mesh independence is numerically verified by calculating the observed order of convergence and an estimate for the discretization errors using Richardson extrapolation, for the shape-factor as quantity of interest, included in table 4.5. It is found that the observed order of convergence corresponds to the expected value of 2 (since a second-order upwind discretization scheme is used), indicating that Richardson extrapolation is valid. The obtained discretization errors confirm that mesh M3 is dense enough to yield a mesh-independent BFM solution, as the error is found to be well below 1%.

The simulations were considered sufficiently converged, as the mean difference in shape factor corresponding to a drop in pressure residual of 7×10^{-4} was observed to be below 0.1%. Moreover, the BFM streamwise velocity and vorticity contours presented in figure 4.10 show a good agreement with the experimental data. This is also observed from the measurement points contained in figures 4.9(b) and 4.9(c), which confirm that the obtained BFM solution is representative of the actual flow field.

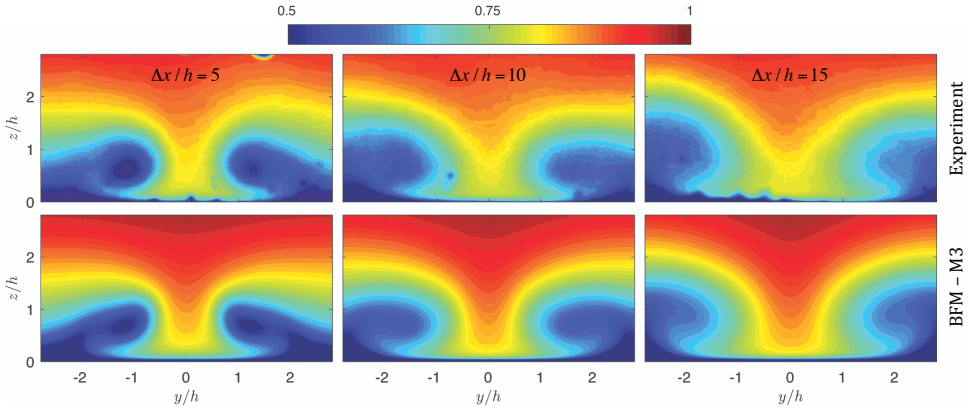

(a) Streamwise velocity (U_x/U_∞)

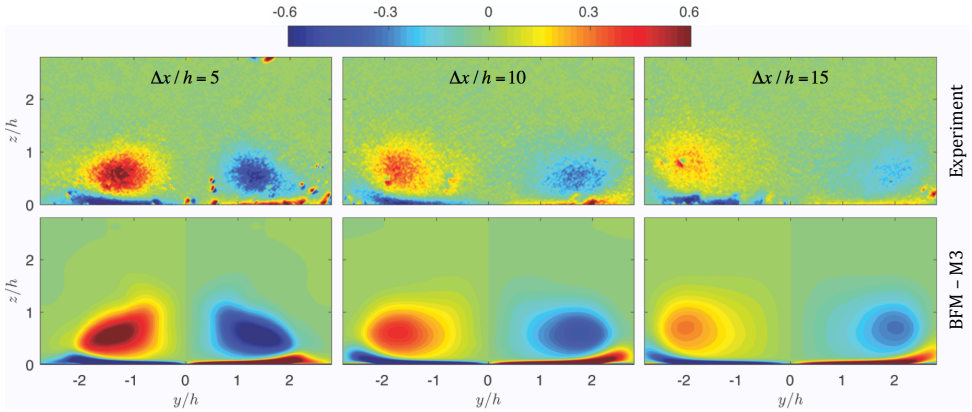

(b) Streamwise vorticity ($\omega_x \cdot h/U_\infty$)

Figure 4.10: Contours plots at three locations downstream of a counter-rotating VG pair on a flat plate for validation of the BFM result.

4.4.3. AIRFOIL WITH COMMON-UP VORTEX-GENERATOR PAIRS

DESCRIPTION

In addition to the flat-plate test cases, a more industrial relevant test case, consisting of a three-dimensional airfoil section, is studied in order to extend our considered range of flow conditions. The chosen airfoil profile has a thickness-to-chord ratio of 18% and is designed for use on variable-pitch and variable-speed multi-megawatt (MW) wind turbines. The effect of triangular VGs for this airfoil was studied experimentally by Manolesos and Voutsinas [61] for a Reynolds number based on the airfoil's chord length of $Re_c = 0.87 \times 10^6$.

The setup used in this work is based on the configuration of Manolesos and Voutsinas [61], however, using rectangular VGs instead of triangular VGs. This was done in order to enhance the similarity with the flat-plate cases and to facilitate a straightforward construction of a quality body-fitted mesh. In contrast with the flat-plate cases, however, the VGs were not submerged but instead have a height that is approximately equal to the local boundary-layer thickness, $h \approx \delta$. For the current analysis, we used an angle of attack of $\alpha = 10°$ and we included counter-rotating common-up VG pairs at 30% of the chord. This corresponds to a distance of approximately 21 VG heights before the point where boundary-layer separation will occur in absence of VGs. More details with respect to the considered flow and VG setup are included in table 4.1.

To limit the computational cost, it was desirable to limit the extent of the numerical domain. In this work the BFM and source-term simulations were therefore performed for a slice of the domain containing half a VG pair only (see figure 4.11(a)). Again, symmetry boundary conditions were used to account for the effect of neighboring VGs. Apart from the crossflow direction, the extent of the numerical domain was governed by the airfoil geometry, rather than the VG.

A 3D body-fitted structured mesh was created using Pointwise®. The mesh around the airfoil and VG was constructed by using a C-type mesh close to the airfoil surface (built by normal extrusion from the surface), and surrounding it by an O-type mesh, with the farfield boundary located 50 chord lengths away from the airfoil. Mesh stretching in wall-normal direction was used away from the surfaces (both the airfoil surface and the VG) to concentrate sufficient cells in the near-wall regions to resolve the boundary layer. A hyperbolic-tangent node distribution was used near the wall, such that the growth rate increases with wall distance. Also near the leading and trailing edges a high cell concentration was created by stretching in streamwise direction to resolve the expected flow

Table 4.6: Mesh details for the airfoil test case, with N the total number of cells, N_c the number of cells in crossflow direction for the considered airfoil section, and y_0 the cell height of the first layer near the wall.

	BFM			Uniform		
	M1	M2	M3	M1	M2	M3
N	0.3×10^6	2.2×10^6	17.8×10^6	2.0×10^6	4.3×10^6	9.9×10^6
N_c	32	64	128	18	36	72
y^+	0.93	0.57	0.28	0.28	0.28	0.28
y_0	3×10^{-5}	1.5×10^{-5}	7.5×10^{-6}	7.5×10^{-6}	7.5×10^{-6}	7.5×10^{-6}

gradients. Snapshots of the mesh are shown in figure 4.11. For the sake of establishing mesh independence of the BFM solution, body-fitted meshes were created with different mesh resolutions, using a factor 2 refinement in all directions between subsequent meshes (see table 4.6).

For the source-term simulations, three structured meshes were generated, also consisting of a C-mesh close to the surface of the airfoil and surrounded by an O-type mesh. These meshes were constructed with mesh resolutions similar to the body-fitted mesh M3, including the clustering of cells near the airfoil's leading and trailing edges and near the wall. Apart from these regions, mesh stretching was also applied in streamwise di-

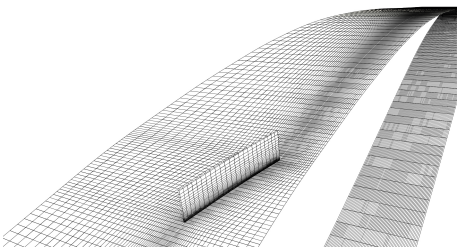

(a) BFM - M2

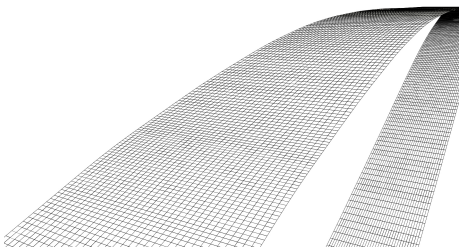

(b) uniform - M2

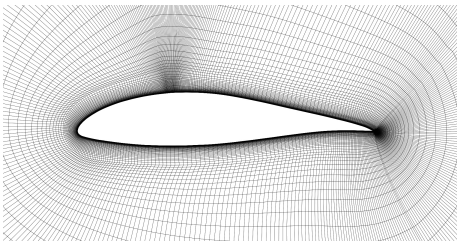

(c) BFM - M2

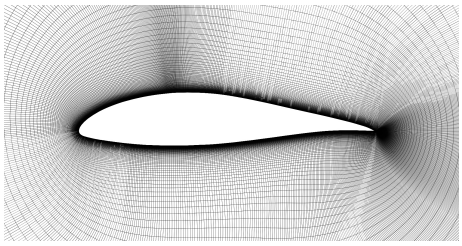

(d) uniform - M2

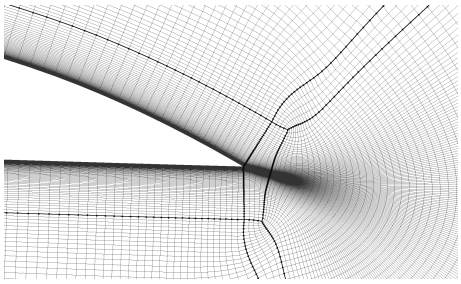

(e) Close-up of the mesh BFM-M3 at the airfoil's trailing edge, including visualization of the blocks used to construct the mesh. Although not exactly coinciding, this part of the mesh is very similar to the uniform meshes.

Figure 4.11: Snapshots of the meshes used for the BFM and source-term simulations of the airfoil case.

rection to cluster cells in the vicinity of the VG location. These three meshes differ with respect to mesh resolution in the vicinity of the VG only, in both the streamwise direction and in crossflow direction, with N_c varying from 18 for M1 to 72 for M3. Although these meshes are not characterized by a uniform mesh spacing, in line with the flat plate cases they are referred to as 'uniform' meshes in the remainder of this work.

On all wall surfaces no-slip boundary conditions were applied. On the farfield boundary, boundary conditions were applied that switch between freestream inflow and outflow conditions based on the direction of the local velocity (the openFOAM® boundary conditions 'freestream' for velocity, 'freestreamPressure' for pressure, and 'inletOutlet' for the turbulent quantities were used). Hence, Dirichlet conditions were specified for the velocity and turbulent quantities (using $U_\infty = 24\text{m/s}$, $k = 3.46 \times 10^{-3}\text{m}^2/\text{s}^2$ and $\omega = 9.8/\text{s}$) in case of inflow, and homogeneous Neumann conditions were used at those faces where the flow leaves the domain.

BODY-FITTED MESH SIMULATION RESULTS

The reliability of the BFM results for use as reference data in our study was verified by studying their mesh dependency. Visual inspection of figure 4.12 indeed suggests mesh convergence. Moreover, for the shape factor the observed order of convergence and estimates for the discretization errors are included in table 4.7, as obtained using Richardson extrapolation. The observed order of convergence was found to be sufficiently close to the expected value of 2 to obtain reliable discretization-error estimates. Despite the estimated errors being larger than for the flat-plate cases, these results confirm that mesh BFM-M3 can be trusted to yield mesh-independent reference results. The discretization error with respect to the shape-factor profiles, one of the key parameters in our study, was found to be well below 1%. Moreover, the dimensionless wall distances near the airfoil and VG surfaces were found to be sufficiently small ($y^+ < 1$) to resolve the inner layers of the boundary layer.

In this case, the required level of iterative convergence was additionally verified by considering the airfoil's lift and drag coefficients. A plot of their iterative convergence is shown in figure 4.13. Upon convergence, the iterative errors were found to be $< 0.01\%$ for C_l and $< 0.05\%$ for C_d.

Since the shape of the VG was modified from triangular to rectangular, no experimental data was available to validate the BFM results. However, lift and drag polars were constructed for the clean airfoil (without VGs) and compared against fully-turbulent clean experimental and reference CFD results. This allowed for a partial validation, ensuring the reliability of our numerical settings and the vortex-unrelated mesh properties. The mesh used for this clean-airfoil validation was based on BFM-M3, having the same mesh refinements near the airfoil surface and the leading and trailing edges. Validation

Table 4.7: Shape-factor discretization errors for the BFM simulations of the airfoil case, according to equations (4.9), (4.10) and (4.11). ϵ_H represents the average in both crossflow (y) and streamwise direction.

	p_o	M1	M2	M3
ϵ_H	1.8	6.7%	1.4%	0.4%

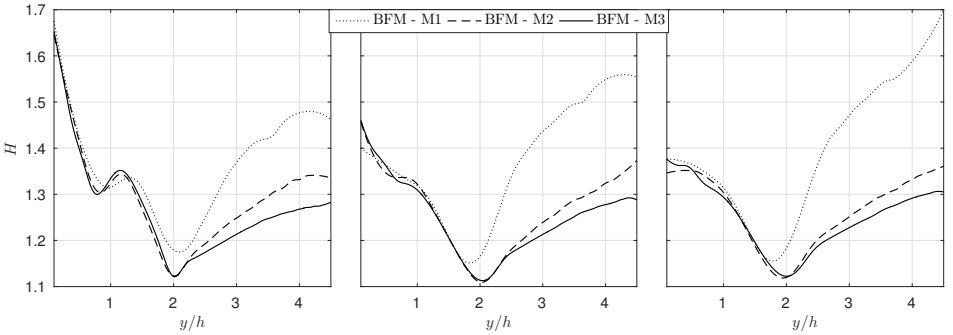

(a) Shape-factor profiles at $\Delta x = 5h$ (left), $\Delta x = 10h$ (middle) and $\Delta x = 15h$ (right) downstream of the VGs.

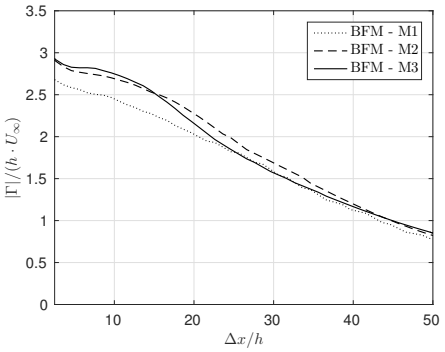

(b) Circulation

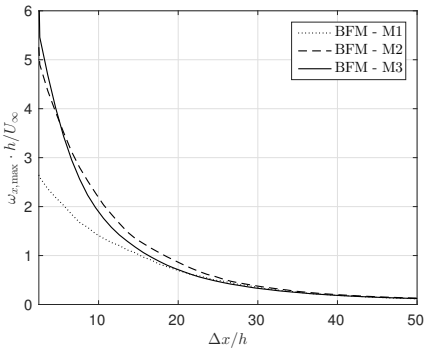

(c) Streamwise peak vorticity

Figure 4.12: Mesh convergence for the airfoil with VG BFM simulations.

was performed against the experimental data of [62] and against CFD simulations for the same situation performed at the Denmark Technical University using the code Ellipsys, as part of the benchmark study in [8].

Our results obtained with OpenFOAM® were found to compare well with the reference CFD data (figure 4.14). For small angles of attack, the numerical results were also in agreement with the experimental data. Apart from the lift and drag polars, also a graph of the spanwise-averaged pressure distribution over the airfoil surface is included, for an angle of attack of $\alpha = 10°$. Again, our numerical results were found to be in excellent agreement with the Ellipsys data. However, when flow separation occurs over the airfoil, the reliability of a RANS simulation in combination with an eddy-viscosity model is clearly insufficient to yield reliable aerodynamic force coefficients.

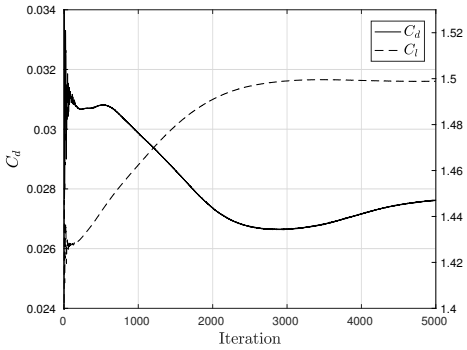

Figure 4.13: Iterative convergence of the lift and drag coefficients, for BFM simulation of the airfoil section with VG.

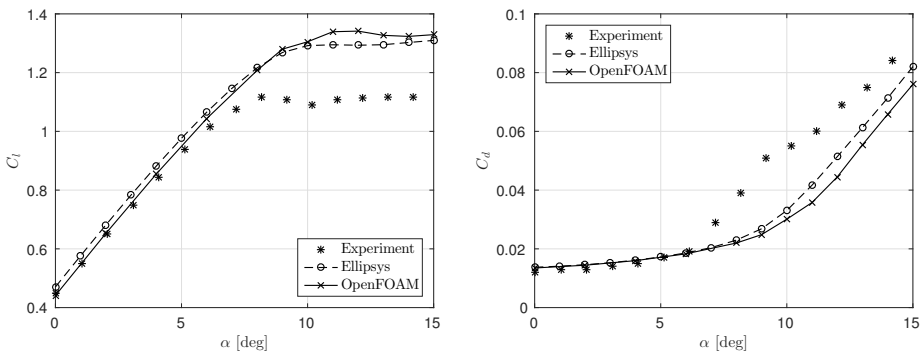

(a) Lift polar

(b) Drag polar

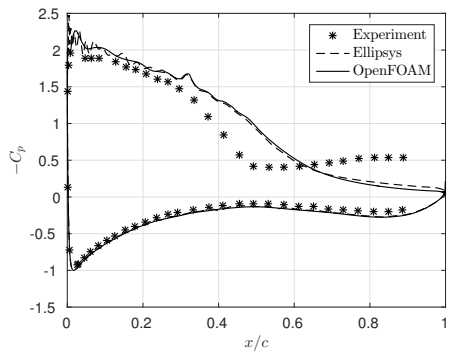

(c) Pressure distribution at $\alpha = 10°$

Figure 4.14: Validation for the airfoil section without VG, validation data according to [8].

5

ANALYSIS OF THE BAY AND JBAY MODELS

As was found in chapter 3, the BAY model and its successor, the jBAY model, are currently the most widely used approaches to include VG effects in CFD simulations. In the present chapter we evaluate their performance based on the research approach outlined in chapter 4, in order to enhance the understanding of the potential and limitations of both models. The current analysis considers the influence of cell selection (for the BAY model, section 5.2) and mesh resolution (section 5.3) on the predictive capabilities of these models with respect to the created boundary-layer disturbance. Moreover, in section 5.3 the impact of the differences between the jBAY model and the original BAY formulation are assessed.

It is shown that the results of the BAY model strongly depend on the selected source-term region, while the jBAY model does not reduce mesh dependency as expected. The results contained in this chapter furthermore highlight that an error is present in both models, which prevents them from accurately reproducing boundary-layer characteristics. This chapter concludes with a summary of our findings in section 5.4.

5.1. IMPLEMENTATION DETAILS

The BAY and jBAY models are implemented in the open-source finite-volume CFD code OpenFOAM®, to allow for the freedom of both analyzing the original formulations as well as constructing and studying model modifications. A thorough description of the baseline lay-out and numerical methods of this code, written in C++ and originally developed at Imperial College, can be found in the work of Jasak [39].

5.1.1. ADDITION OF THE SOURCE TERM TO THE GOVERNING EQUATIONS

Since the flows of interest considered in this work can be characterized as being steady and incompressible (see section 4.2), implementation of the BAY and jBAY models is done by modifying the existing simpleFoam solver. This is a steady-state solver for in-

compressible flows in absence of external forcing, which solves the governing equations

$$\nabla \cdot \mathbf{u} = 0 \tag{5.1}$$

$$\nabla \cdot (\mathbf{uu}) - \nabla(\nu \nabla \mathbf{u}) = -\nabla p, \tag{5.2}$$

where the pressure p actually denotes a modified pressure which is scaled by the density. The simpleFoam solver supports both LES and RANS simulations, and makes use of the SIMPLE algorithm (originally described by Patankar [76]) to obtain a discrete solution for the above coupled system of partial differential equations.

The SIMPLE method, short for semi-implicit method for pressure-linked equations, is a segregated approach that allows for a discrete solution of the flow field by constructing explicit discretized equations for both the pressure and the velocity. To do so, (5.2) is first formulated in semi-discrete form (not discretizing the pressure gradient). Upon substitution into (5.1) and by making use of Gauss's theorem, a Poisson equation for the pressure is obtained which allows solution for the pressure based on the (non-divergence-free) velocity fluxes at the cell faces. As OpenFOAM® uses a collocated mesh approach, interpolation is used to obtain these face fluxes.

Starting from initial guesses for the pressure and turbulence quantities, the SIMPLE method thus solves both velocity and pressure equations in an iterative process to improve p such that $\mathbf{u}$ will progressively get closer to satisfying the continuity equation. Note that the iterative process includes a correction step for $\mathbf{u}$ such that every sub-solution satisfies conservation of mass. It should furthermore be noted that, as the pressure equation is prone to divergence, in general under-relaxation is required when updating the pressure field.

To simulate the effect of VGs on the flow field, the momentum equation (5.2) solved in the original simpleFoam solver is expanded to include a source term $\mathbf{f}$ (the VG model) to become

$$\nabla \cdot (\mathbf{uu}) - \nabla(\nu \nabla \mathbf{u}) - \mathbf{f} = -\nabla p. \tag{5.3}$$

This source term $\mathbf{f}$ consists of a vector field defined in the entire domain, but which is only locally non-zero in the neighborhood of the desired VG locations. In the current implementation $\mathbf{f}$ is added in an explicit fashion to the discretized momentum equation, hence it is lagging in the pressure equation solved in the iterative SIMPLE process. This approach is preferred for stability reasons due to the tendency of the pressure equation towards divergence. However, as observed by Patankar [76], the converged solution is uninfluenced by any approximations made in the pressure equation. The fact that eventually the velocity field resulting from the discretized momentum equation (a function of p) satisfies conservation of mass (5.1), is evidence that we have acquired the correct pressure field.

5.1.2. VG OBJECT DEFINITION

To enable the easy set-up of simulation cases involving VGs, a class was constructed that creates a VG object for every VG within the simulation. These objects are defined by the (private) data members

$$VG(l, h_1, h_2, \beta, A, \mathbf{p}_1, \mathbf{p}_2, \mathbf{b}, \mathbf{n}, \mathbf{t}, \delta, V_{tot}),$$

denoting respectively the VG's length, height at the leading and trailing edges, incidence angle, planform area, surface locations of the leading and trailing edges, unit direction vectors, the domain where the source term is to be added and the volume of application. Creation of a VG object is done in an external dictionary file by specifying the parameters l, h_1, h_2 (only if $h_1 \neq h_2$), β and $\mathbf{p}_1$, only. The other variables are calculated upon creation of the VG object, which is done as an initialization step before entering the SIMPLE loop.

The VG planform area is defined as

$$A = \frac{1}{2} l (h_1 + h_2), \tag{5.4}$$

and the trailing edge location as

$$\mathbf{p}_2 = \mathbf{p}_1 + l \begin{pmatrix} \cos\beta \\ \sin\beta \\ 0 \end{pmatrix}, \tag{5.5}$$

where the z-coordinates of $\mathbf{p}_1$ and $\mathbf{p}_2$ are adapted such as to lie on the surface. The unit vector $\mathbf{b}$ is defined at the location $\mathbf{p}_1$ to be normal to the surface, and

$$\mathbf{t} = \frac{\mathbf{p}_2 - \mathbf{p}_1}{|\mathbf{p}_2 - \mathbf{p}_1|} \qquad \text{and} \qquad \mathbf{n} = \frac{\mathbf{t} \times \mathbf{b}}{|\mathbf{t} \times \mathbf{b}|}. \tag{5.6}$$

The most elaborate part of the VG-object creation consists of the selection of the cells where the source term, representing the VG, is to be applied. Selection of these cells can be done in several ways, an overview of the implemented options is given in section 5.1.3. The outcome of the cell-selection process consists of the characteristic scalar field

$$\delta = \begin{cases} 1 & \text{in } \Omega_{VG} \\ 0 & \text{in } \Omega \setminus \Omega_{VG} \end{cases}, \tag{5.7}$$

with Ω_{VG} the considered domain of application, such that the total volume of application becomes

$$V_{tot} = \sum_{i=1}^{N} V_i \delta_i. \tag{5.8}$$

5.1.3. CELL SELECTION APPOACHES

Several approaches to define the domain Ω_{VG} (and therefore the characteristic scalar field δ) in which the source-term model is applied (and thus $\mathbf{f} \neq 0$) were implemented. These different options are illustrated in figure 5.1 and briefly discussed below.

ALIGNED CELL SELECTION

The aligned cell-selection option consists of defining a virtual zero-thickness surface, with the same planform as the actual VG, and selecting all cells that are cut by this surface. This surface is spanned by the points $\mathbf{p}_1$, $\mathbf{p}_2$, $\mathbf{p}_3 = \mathbf{p}_1 + (0 \quad 0 \quad h_1)^T$ and $\mathbf{p}_4 = \mathbf{p}_2 + (0 \quad 0 \quad h_2)^T$.

ORIGINAL CELL-SELECTION APPROACH

For the original cell-selection approach for the BAY model, defined by Bender et al. [11], several rows of cells are selected, the amount of which is determined by calibration. Implementation of this approach is done in two steps, the first of which consists of applying the aligned approach for a surface spanned by the points

$$\mathbf{p}_1^* = \mathbf{p}_1 + \begin{pmatrix} 0 \\ l/2 \cdot \sin\beta \\ 0 \end{pmatrix}, \mathbf{p}_2^* = \mathbf{p}_1 + \begin{pmatrix} l\cos\beta \\ 0 \\ 0 \end{pmatrix}, \mathbf{p}_3^* = \mathbf{p}_1^* + \begin{pmatrix} 0 \\ 0 \\ h_1 \end{pmatrix} \text{ and } \mathbf{p}_4^* = \mathbf{p}_2^* + \begin{pmatrix} 0 \\ 0 \\ h_2 \end{pmatrix}, \quad (5.9)$$

hence selecting a row of cells in streamwise direction spanning the distance between the VG's LE and TE (indicated in orange in figure 5.1(b)). In the second step extra rows of cells are added by selecting neighboring cells in either positive y-direction or in negative y-direction (indicated in blue in figure 5.1(b)). Rows of cells are added until the crossflow kinetic energy at a chosen location is found to correspond to reference data to a satisfactory extent. The crossflow kinetic energy κ is defined as

$$\kappa = \frac{\int_S \rho(v^2 + w^2)\,\mathrm{d}S}{\int_S \rho u^2\,\mathrm{d}S}, \quad (5.10)$$

with u the streamwise and v, w the secondary velocity components ($\mathbf{u} = (u \quad v \quad w)^T$).

JBAY CELL SELECTION

For the jBAY model, cells are selected on either side of the virtual zero-thickness VG surface. Therefore, the first step consists of performing the aligned cell selection described above. The cell domain selected this way is then extended by adding additional cells adjacent to the selected cells on the other side of the virtual VG surface (if not already selected). A typical domain Ω_{VG} defined this way consists of the colored cells illustrated

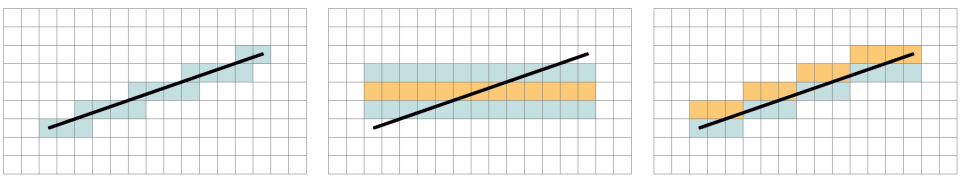

(a) Aligned (b) Original (c) jBAY

Figure 5.1: Top views illustrating the considered cell-selection approaches to define Ω_{VG}.

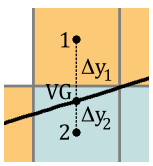

Figure 5.2: Visualization of the notation used for the calculation of the jBAY source term.

in figure 5.1(c). In the source-term calculation, a distinction is made between the cells with $y > y_{VG}$ ($\Omega_{VG,1}$, indicated in orange) and those with $y < y_{VG}$ ($\Omega_{VG,2}$, indicated in blue).

5.1.4. SOURCE-TERM CALCULATION

The calculation of the source term, **f**, that represents the VG effect on the flow is performed during runtime, as **f** depends on the flow field and is updated between iterations.

BAY MODEL

With all VG-specific parameters defined, the (global) source term **f** can be computed based on the BAY model formulation defined by (3.11). This vector field varies between iterations, and is updated using under-relaxation to facilitate convergence. For a relaxation factor α_f, the source-term update due to a specific VG is

$$\mathbf{f} = (1-\delta)\mathbf{f} + (1-\alpha_f)\delta\mathbf{f} + \alpha_f\delta\frac{cA}{V_{tot}}(\mathbf{u}\cdot\mathbf{n})(\mathbf{u}\times\mathbf{b})\left(\frac{\mathbf{u}}{|\mathbf{u}|}\cdot\mathbf{t}\right). \tag{5.11}$$

In the above formulation, the VG-specific scalar field δ allows for easy updating of the global source-term field **f** due to the contribution of a single VG. It was found that in general $\alpha_f = 0.15$ yields good convergence. Note that (5.11) is the source term as added to the discrete momentum equation, hence it is divided by $V_i\rho$ when compared to (3.11).

JBAY MODEL

Calculation of the source term **f** when using the jBAY model is very similar to the BAY-model procedure described above, with some additional interpolation and redistribution steps included. As the approach taken for the interpolation and redistribution is not explicitly stated by Jirasek [41], the approach described below might differ slightly from the original. However, as the concept of the formulation is clear, this should not produce significant differences. The following steps are taken for each of the cells, when looping over the cells in domain $\Omega_{VG,1}$ in streamwise direction. The notation used is clarified in figure 5.2.

1. Calculation of the velocity $\mathbf{u}_{VG}$ on the virtual VG surface. This is done by linear interpolation between the velocities at the cell centers on either side of the virtual VG surface, so using $\mathbf{u}_1$ and $\mathbf{u}_2$ where $\mathbf{u}_1$ corresponds to an orange cell in figures 5.1 and 5.2 and $\mathbf{u}_2$ to the velocity in a blue cell.
2. Calculation of the local body force $\mathbf{f}_{VG}$ at the VG surface according to (3.11), hence as
$$\mathbf{f}_{VG} = \frac{cA}{V_{tot}}(\mathbf{u}_{VG}\cdot\mathbf{n})(\mathbf{u}_{VG}\times\mathbf{b})\left(\frac{\mathbf{u}_{VG}}{|\mathbf{u}_{VG}|}\cdot\mathbf{t}\right). \tag{5.12}$$
3. Redistribution of $\mathbf{f}_{VG}$ to the cell centers on either side of the virtual VG surface. This is done such that
$$\begin{cases} V_1\mathbf{f}_1 + V_2\mathbf{f}_2 = (V_1+V_2)\mathbf{f}_{VG} \\ \Delta y_1\mathbf{f}_1 = \Delta y_2\mathbf{f}_2 \end{cases}, \tag{5.13}$$

where V_1 and V_2 indicate the cell volumes of the associated cells in domain $\Omega_{VG,1}$ and $\Omega_{VG,2}$, and Δy_1 and Δy_2 represent the distance between the cell centers and the location on the virtual VG surface in between. This step results in the vector fields $\mathbf{f}_1$ and $\mathbf{f}_2$, with $\mathbf{f}_1$ non-zero in $\Omega_{VG,1}$ only and $\mathbf{f}_2$ non-zero in $\Omega_{VG,2}$ only.

With $\mathbf{f}_1$ and $\mathbf{f}_2$ specified, the source-term field can thus be updated for the contribution of a specific VG according to

$$\mathbf{f} = (1-\delta)\mathbf{f} + (1-\alpha_f)\delta\mathbf{f} + \alpha_f(\mathbf{f}_1 + \mathbf{f}_2). \tag{5.14}$$

Note that in the above $\mathbf{u}_{VG}$ and $\mathbf{f}_{VG}$ are auxiliary variables, which are used for the calculation of $\mathbf{f}_1$ and $\mathbf{f}_2$. They are not tied to a specific part of the domain and change value while looping over the cells in $\Omega_{VG,1}$.

5.2. INFLUENCE OF THE SOURCE-TERM DOMAIN ON THE BAY-MODEL RESULT

As discussed in section 5.1.3, several approaches to define the source-term domain Ω_{VG} have been implemented. In this section, the influence of Ω_{VG} on the resulting flow field is studied. For this analysis, distinction is made between definition of Ω_{VG} oriented in the direction of the VG (both the "Aligned" and "jBAY" selection methods), hence resembling the actual VG lay-out, and in a rectangular domain (the "Original" approach). Note that, although we are solely considering the BAY model is this section, the jBAY source-term domain is included in this analysis such that other than the direction, also the effect of the width (and hence volume) of the source-term domains can be assessed.

The following test cases, all on a flat plate and varying in mesh resolution and lay-out, were considered: (i) the submerged VG pair (section 4.4.2) using the coarse mesh M0, (ii) the same VG pair case on a finer mesh M2, and (iii) a single submerged VG (section 4.4.1) using mesh M2. Note that the same VG pair case was computed on two different meshes, in order to analyze dependence on the mesh of Ω_{VG} for κ calibration. Scalar vortex-descriptor results and shape-factor profiles are shown in figures 5.3 and 5.4 for the coarse mesh (M0) VG pair case. Similar graphs for the other cases are included in appendix A. Note that for the VG pair cases the circulation results differ slightly from the results presented in section 4.4.2, as a different definition of the vortex region S was used, based on a cut-off value for ω_x rather than the Q-criterion. Additionally, table 5.1 presents the volumes of Ω_{VG} and the scaled streamwise-averaged errors in the vortex parameters for the considered simulations, which are calculated for a quantity q according to

$$\epsilon_q = \frac{1}{n}\sum_{i=1}^{n}\frac{|q_i^* - q_i|}{|q_i^*|}, \tag{5.15}$$

with i indicating the streamwise locations, varying from $\Delta x_i = 5h$ to the end of the considered domain, and the superscript $*$ representing the BFM result.

The obtained results indicate that the source-term domain Ω_{VG} has a large influence on the vortex flow field created with the BAY model. A large spread is especially present in the generated crossflow kinetic energy κ and the vorticity levels (hence in Γ

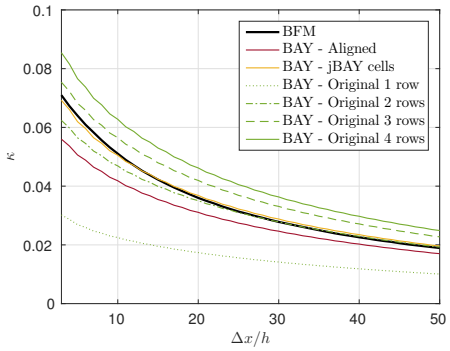

(a) Crossflow kinetic energy

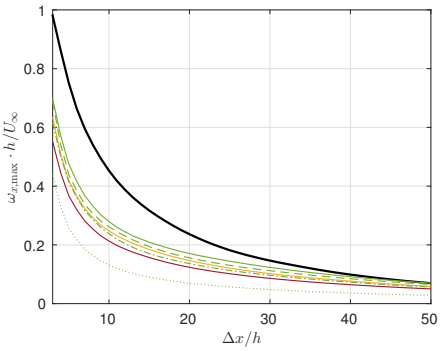

(b) Streamwise peak vorticity

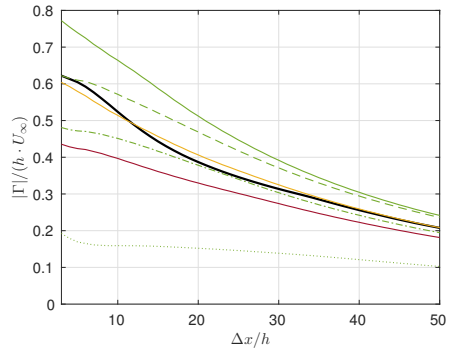

(c) Circulation

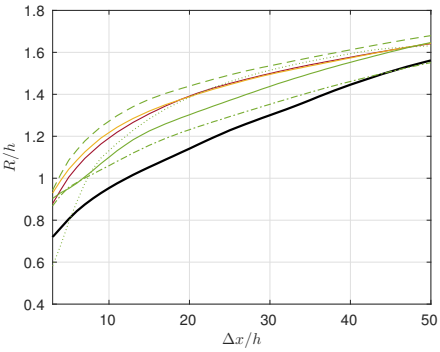

(d) Vortex core radius

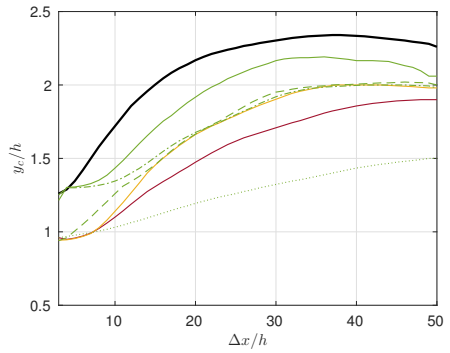

(e) Vortex center in crossflow direction

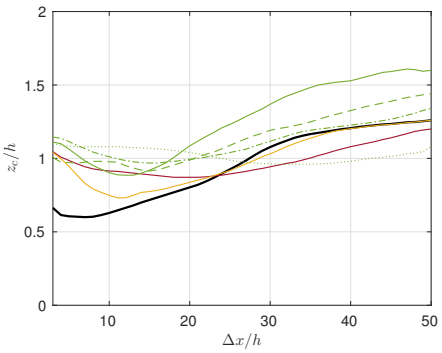

(f) Vortex center in wall-normal direction

Figure 5.3: Non-dimensionalized vortex descriptors for the flat plate with a counter-rotating VG pair test case, using the coarsest mesh M0, comparing the effect of different cell-selection approaches.

and, to a lesser extent, $\omega_{x,\max}$), which are found to increase with V_{tot}. Moreover, a remarkable variation of the vortex-core center location in crossflow direction (y_c) is observed. Overall, the BAY model yields a vortex whose center is located on the suction side of the VG. With increasing V_{tot} the center moves away, towards the VG's pressure side (figure 5.3(e)). The choice for Ω_{VG} therefore clearly has a large impact on both the strength and the path of the generated vortex. The variation in results with respect to the vortex's radius and its distance from the wall, however, is rather limited. Contrary to what might be expected, only a minor increase in vortex radius is observed with increasing width of Ω_{VG} and the corresponding vorticity level.

The large spread in results for different cell-selection approaches confirms that calibration is required for an optimal usage of the BAY model. In [11] it was advised to perform this calibration based on κ. Indeed, the results in table 5.1 show that a match in crossflow kinetic energy typically corresponds to the best agreement in circulation as well, thus yielding a good representation of the total flow mixing. However, depending on one's objective, κ only might not be sufficient to yield an optimal result. For example, the best results with respect to the vortex-core location are obtained for larger Ω_{VG}, which is important to consider when analyzing the vortex path. This implies that it is difficult to obtain accurate results for both the strength and the path of the vortex

Table 5.1: Average errors in vortex properties with respect to the BFM result, as obtained with the BAY model using different cell-selection approaches for several flat-plate test cases. N_r indicates the number of rows of cells. The physical VG volume $V_{VG} = l \cdot h \cdot t$ is included for reference.

Case	Method	V_{tot}	ϵ_κ	$\epsilon_{\lvert\Gamma\rvert}$	ϵ_R	ϵ_{y_c}	ϵ_{z_c}
VG Pair M0 $V_{VG} = 3.1 \times 10^{-8}$	Aligned	1.9×10^{-7}	25%	18%	**17%**	26%	22%
	jBAY cells	3.0×10^{-7}	**6%**	**3%**	19%	**21%**	**13%**
	Orig. $N_r = 1$	1.5×10^{-7}	76%	60%	16%	38%	34%
	Orig. $N_r = 2$	3.0×10^{-7}	**8%**	17%	**7%**	17%	26%
	Orig. $N_r = 3$	4.4×10^{-7}	35%	**14%**	22%	20%	**26%**
	Orig. $N_r = 4$	5.9×10^{-7}	64%	24%	14%	**10%**	37%
VG Pair M2 $V_{VG} = 3.1 \times 10^{-8}$	Aligned	3.4×10^{-8}	34%	22%	**14%**	25%	34%
	jBAY cells	6.4×10^{-8}	**11%**	**7%**	17%	**14%**	**15%**
	Orig. $N_r = 1$	3.2×10^{-8}	84%	69%	17%	43%	42%
	Orig. $N_r = 2$	6.4×10^{-8}	42%	29%	**14%**	27%	35%
	Orig. $N_r = 3$	9.6×10^{-8}	14%	11%	15%	22%	29%
	Orig. $N_r = 4$	1.3×10^{-7}	**12%**	**10%**	16%	**17%**	**22%**
Single VG M2 $V_{VG} = 3.4 \times 10^{-7}$	Aligned	9.0×10^{-7}	33%	18%	**15%**	44%	**8%**
	jBAY cells	1.4×10^{-6}	**16%**	**8%**	17%	**31%**	10%
	Orig. $N_r = 3$	2.1×10^{-6}	37%	24%	**14%**	44%	**11%**
	Orig. $N_r = 5$	3.5×10^{-6}	18%	13%	17%	35%	18%
	Orig. $N_r = 7$	4.9×10^{-6}	**5%**	**3%**	21%	21%	19%
	Orig. $N_r = 11$	7.7×10^{-6}	33%	18%	31%	**14%**	20%

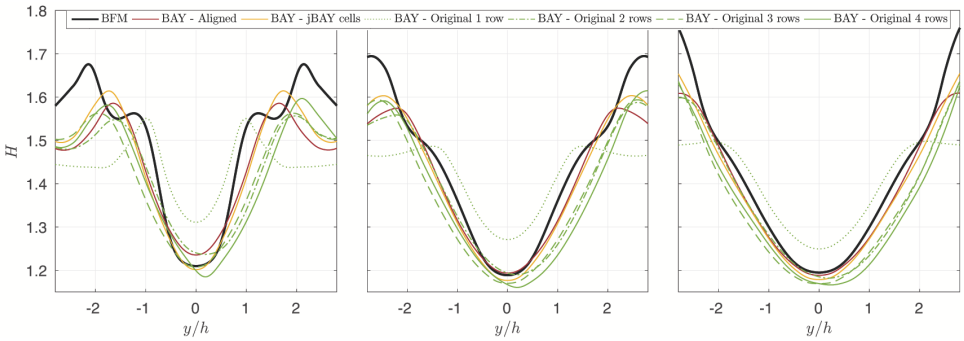

Figure 5.4: Shape-factor profiles for the flat-plate VG-pair simulation on mesh M0, for different source-term regions, at $\Delta x = 5h$ (left), $\Delta x = 10h$ (middle) and $\Delta x = 15h$ (right) downstream of the VGs.

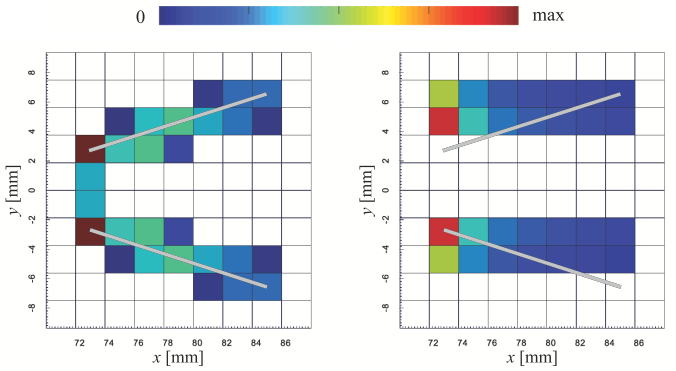

(a) jBAY cell selection (b) Calibrated original cell selection

Figure 5.5: Snapshots showing the domain Ω_{VG} at a cutting plane at $z = 0.6h$ for the VG-pair test case (coarse mesh M0), colored according to source-term magnitude.

when using the BAY model. Moreover, in practice calibration data is often unavailable. The question thus arises whether it is possible to predict the optimal source-term region without reference results.

Our analysis considers two orientations for Ω_{VG}, the first oriented in the direction of the VG, and the second a rectangular domain in streamwise direction. Both of these are found capable of yielding a similar accuracy. Counter-intuitively, alignment of Ω_{VG} with the VG to be modeled does not per se result in a more accurate flow field in terms of the shape-factor profile, even though the source-term distribution (visualized in figure 5.5) bears a larger resemblance with the physical reaction forces imposed on the flow by the actual presence of a VG. When a rectangular domain centered at the VG location is chosen as Ω_{VG}, it is observed that the majority of the forcing is applied at the front edge of the domain. This seemingly arbitrary and unphysical source-term distribution does, however, yield similar shape-factor profiles, as shown in figures 5.4 and A.3, thereby giving a first indication of the rather low importance of the distribution of the source term

over the source-term domain. This latter hypothesis is studied in more detail in chapter 6.

With respect to the optimal size of Ω_{VG}, the results reveal that the width of the domain in the crossflow (y-) direction seems to be the dominant characteristic. When considering the vorticity field, it is clear that the wider (and therefore also the larger) Ω_{VG}, the stronger the flow disturbance introduced in the system. An explanation for this observation can be found in the sharpness of the source-term distribution. Upon addition of cells in crossflow direction, the source-term is distributed more smoothly, thereby being less prone to dissipative truncation errors. A stronger flow disturbance thus results for a wider domain. This effect is not only observed for the original, rectangular-shaped, cell-selection approach, but also when selecting cells aligned with the VG. The jBAY cell-selection approach, featuring two cells for every streamwise position, typically results in a stronger and better calibrated vortex. For the original approach the source-term distribution plots seem to imply that in general choosing Ω_{VG} as the bounding box around the VG (as also done in [21]), and in particular such that $N_r \Delta y \approx l \sin\beta$, yields a well calibrated result for κ. Furthermore, when looking at the source-term distribution in a cutting plane at approximately 60% of the VG height (figure 5.5), it becomes clear that the dimension of Ω_{VG} in streamwise direction is less influential. When approaching the VG's trailing-edge location, the added volumetric forcing is almost zero. This suggests that it might be possible to reduce the source-term domain in streamwise direction without significantly altering the result. However, this is not investigated further in this work.

Overall, our analysis has revealed that the result obtained with the BAY model strongly depends on the choice for the source-term domain Ω_{VG}, and that calibration is therefore essential in order to obtain a reasonably accurate flow field. In the absence of calibration data, the cell-selection approach proposed for the jBAY model, thus aligning Ω_{VG} with the actual VG orientation and selecting two cells for every streamwise position, seems to yield the best calibrated flow field.

5.3. MESH-SENSITIVITY STUDY

Numerical simulations of the flat plate and airfoil test cases are performed using several mesh resolutions in order to identify the effect of grid refinement on the flow field obtained with both the BAY and the jBAY model. Starting from a coarse grid, medium and fine grids are constructed by refining by a factor 2 in streamwise (x-) and crossflow (y-) direction, the details of which are included in sections 4.4.2 and 4.4.3.

Results regarding the evolution of the created vortex downstream of the VG are shown in figures 5.6 and 5.7. In figure 5.8 the shape of the boundary-layer disturbance is studied by considering shape-factor profiles close behind the VG.

This section initially discusses BAY-model results obtained using the aligned cell-selection approach, before moving on to the mesh dependence of the jBAY-model results. In section 5.3.2, results are also included for the BAY model using the jBAY cell-selection approach, such that $\Omega_{VG}^{BAY} = \Omega_{VG}^{jBAY}$. This allows isolation of the effect of the jBAY source-term cell selection from the interpolation and redistribution parts of the jBAY formulation.

5.3.1. BAY MODEL WITH ALIGNED CELL SELECTION

From figures 5.6(a), 5.6(d) and 5.7(a) a large dependence on grid resolution of the vortex-core peak vorticity and, to a lesser extent, the vortex-core radius is observed for the BAY model in combination with aligned cell selection. Peak vorticity is observed to increase with increasing mesh refinement, while the vortex becomes more concentrated, due to the improved resolution. Especially for the airfoil case the variation in these results is large, due to the discretization error being more pronounced for the affordable levels of mesh resolution used. The observed variation in radius is related to the variations with mesh resolution of the peak vorticity, due to the definition of A_S being based on this quantity.

In figures 5.6(a) and 5.7(a) the typical underestimation of the vortex's peak vorticity (which can be interpreted as a measure for the vortex intensity) by the BAY model can be observed. This drawback of the BAY model was already identified in previous publications, for example [61, 94]. Despite the mesh dependence of peak vorticity, this underestimation is considered to be a property inherently related to the BAY model. Moreover, as shown in the previous section, calibration of the model, by means of varying Ω_{VG} through the selection of more cells, in general is not able to eliminate this deficit. Increased mesh resolution might help to resolve this problem, but then one approaches the computational cost of BFM simulations, which source-term models are intended to avoid.

The circulation and, especially, the decay of the created vortex (figures 5.6(b), 5.6(c) and 5.7(b)) appear to be less mesh dependent than the peak vorticity, as expected due to those being integral quantities and therefore being less prone to local high-frequency errors. Correspondingly, the influence of mesh resolution on circulation was found to be much smaller than the influence of the source-term domain Ω_{VG}. From the circulation-decay results it follows that a model error seems to be present. The initial vortex decay due to the cancellation of primary vorticity with opposite vorticity that is lifted from the wall seems not to be captured well. It is expected that this is partly attributable to the inviscid assumption related to the BAY model, yielding among others a lack of leading-edge suction recovery. The BAY model therefore yields a vortex which initially decays slower than that obtained when using a body-fitted mesh. Further downstream, when the interaction between the vortex and the turbulence model starts to dominate the decay, the decay rate is similar to the BFM result. It is observed that this difference in initial decay rate to some extent cancels the underestimation of the vortex circulation further downstream.

The shape-factor variations upon mesh refinement are shown in figure 5.8 for both the VG pair on a flat plate and the airfoil test cases. At the lowest level of refinement used, the result is largely dependent on mesh resolution. This is clear in the airfoil shape-factor results obtained using the BAY model in combination with relatively coarse meshes. Hence a certain minimum mesh resolution is required in order to obtain meaningful results with the BAY model. For the flat-plate case, higher mesh resolutions were used, resulting in only small differences in the shape-factor profiles. This indicates that beyond a certain level of mesh resolution the flow profile does not significantly change with mesh refinement.

A closer look at the shape-factor profiles confirms the presence of a model error, as

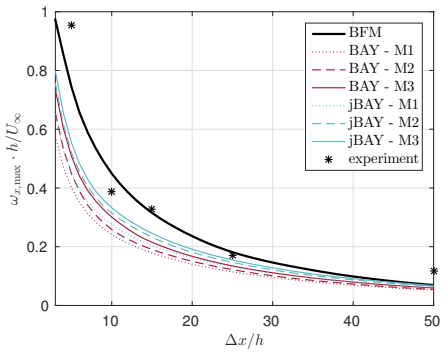

(a) Streamwise peak vorticity.

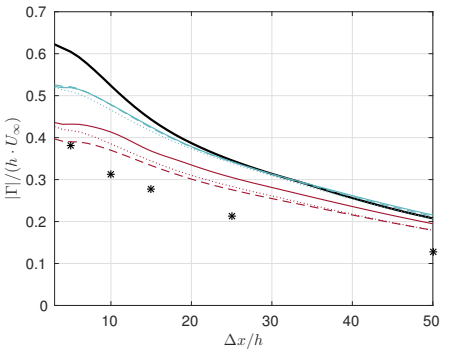

(b) Circulation

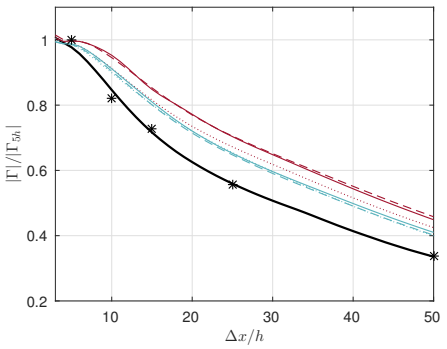

(c) Circulation decay.

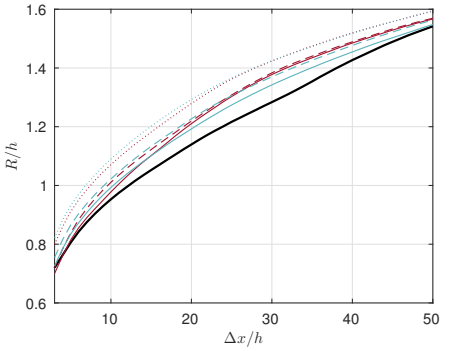

(d) Core radius for an equivalent circular vortex.

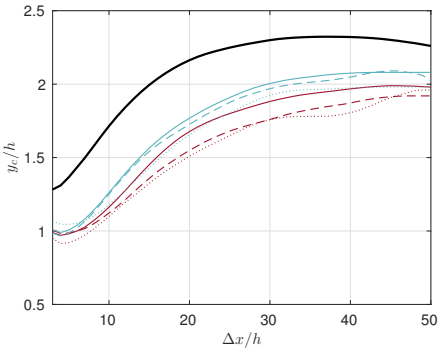

(e) Vortex center in crossflow direction

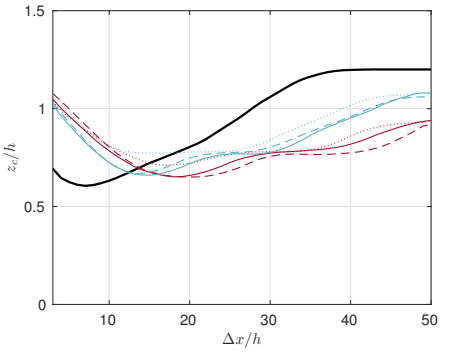

(f) Vortex center in wall-normal direction

Figure 5.6: Vortex evolution downstream of the VG pair on the flat plate for different mesh resolutions for the body-fitted mesh and the BAY (using aligned cell selection) and jBAY models.

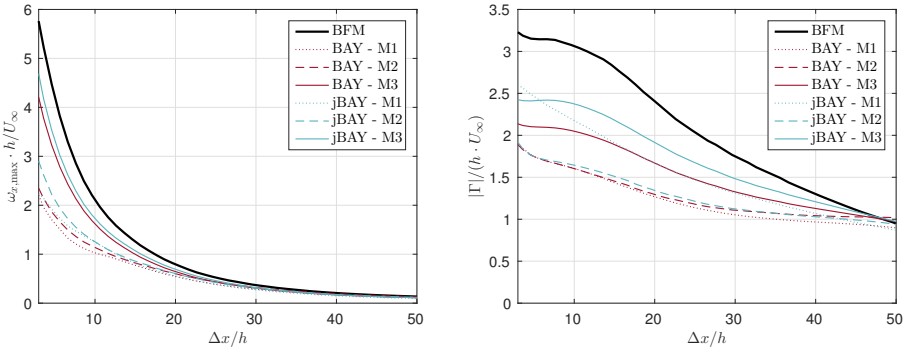

(a) Streamwise peak vorticity.

(b) Circulation

Figure 5.7: Vortex evolution downstream of the VG on the airfoil for different mesh resolutions for the body fitted mesh and the BAY and jBAY models.

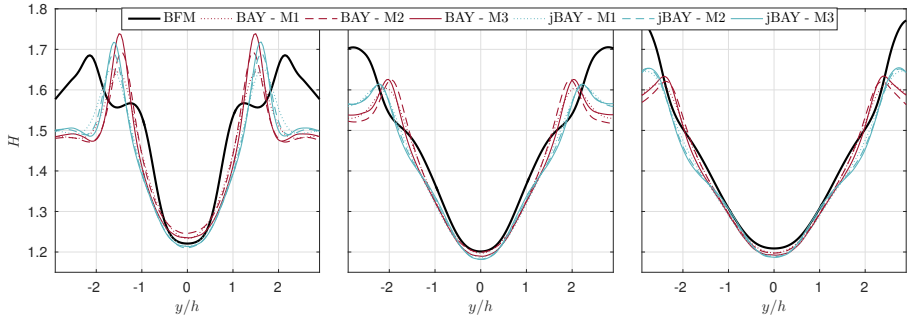

(a) Flat plate with submerged common down VG pair ($h \approx \delta/3$).

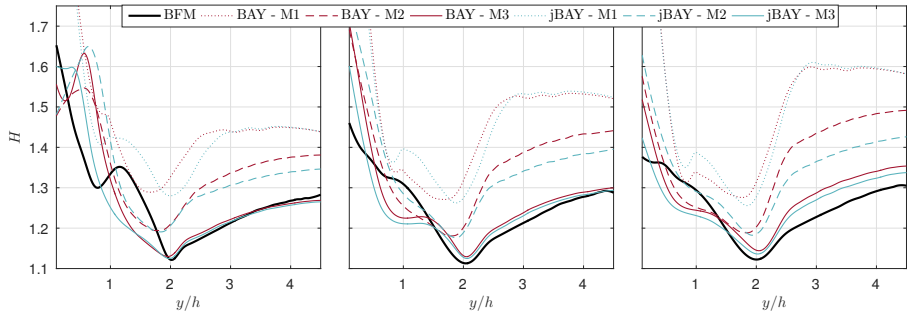

(b) Airfoil section with common up VG pair ($h \approx \delta$).

Figure 5.8: Effect of mesh resolution on the shape factor for the BAY and jBAY models, at (from left to right) $\Delta x = 5h$, $\Delta x = 10h$ and $\Delta x = 15h$ behind the VG pair.

they are very different from the BFM result for small Δx (i.e. closely downstream of the VG). The peaks have different values and are at different locations. This indicates a difference in boundary-layer disturbance, rather than an underestimation of the vortex intensity only. These differences in the boundary-layer profile propagate downstream, and are therefore likely to influence predictions related to the effect of the VGs. However, as the vortex dissipates the shape-function error decreases. Further research is therefore required to quantify the effect of this error on the prediction of boundary-layer separation.

As mentioned before, the observed mesh dependency of the BAY model can be partly explained by the selection of the cells where the model is applied. Upon mesh refinement the forcing is applied in an increasingly confined region. This implies (i) that flow tangency is enforced closer to the actual VG location, (ii) that the distribution of the applied source term becomes smoother, but also (iii) that the total volume V_{tot} where the source term is applied decreases. The first two of these consequences are similar to standard discretization errors and can be expected to decrease upon mesh refinement. However, when selecting cells based on the VG mean surface (as done when using the "aligned" cell-selection approach), for very fine meshes characterized by a local mesh size $\Delta < t_{VG}$ the virtual-VG location will not coincide with the physical-VG location. Upon mesh refinement a zero-thickness VG is approached, instead of the physical VG. Moreover, in this case also V_{tot} and the width of Ω_{VG} will keep on decreasing with mesh refinement. Therefore mesh-independent solutions cannot be expected to be obtained with the BAY model.

5.3.2. JBAY MODEL

The jBAY model[41] was proposed in order to improve accuracy and reduce mesh dependency of the original BAY model. Indeed, our results indicate improved accuracy in the sense that the jBAY model produces a stronger vortex, yielding a smaller error with respect to peak vorticity (figures 5.6(a) and 5.7(a)), and increased flow circulation (figures 5.6(b) and 5.7(b)). Apart from some small variation in intensity, however, the boundary-layer disturbance is very similar to that of the BAY model, as can be seen from the similar shape-factor profiles in figure 5.8. So although the jBAY variation seems to be more successful in capturing the correct amount of vorticity in the flow than the original BAY model, the generated flow disturbance, as characterized by H, is not noticeably different.

A reduced mesh dependency of the jBAY model is to be expected based on the improved formulation of the model. In particular flow tangency is imposed at a consistent location, thereby eliminating a source of mesh dependence from the BAY model. Moreover, the distribution of this forcing over two cells in crossflow direction instead of only one allows for a smoother application of the forcing to the flow field. Both factors are likely to cause the jBAY model to exhibit a reduced mesh dependence compared to the BAY model and therefore to yield less stringent requirements on the mesh resolution. However, the jBAY model retains a mesh dependency due to the region Ω_{VG} where the source term is applied, and hence the term V_{tot}, which decreases with mesh refinement.

In the end, the reduced mesh dependency expected of the jBAY model is not clearly observed. When looking at the circulation (and its decay rate) for the flat-plate VG-pair

case (figures 5.6(b) and 5.6(c)) a seemingly mesh-independent solution is reached for the coarsest mesh, M1, whereas for the BAY model this is only the case for circulation decay for the mesh M2. Also the flat-plate shape-factor profiles, especially further downstream from the VG, seem to differ less than for the standard BAY model. However, for the vortex's peak vorticity, radius and location, there is no clear improvement with respect to mesh dependence compared to the original BAY model.

In order to separate the impact of the two factors that differentiate the jBAY model from the original BAY model, additional BAY-model simulations were performed with Ω_{VG} defined according to the jBAY cell-selection approach, hence $\Omega_{VG}^{jBAY} = \Omega_{VG}^{BAY}$. This implies a 58% to 88% increase in V_{tot} for the VG-pair case compared to the BAY-model results presented in the previous section. The additional simulations were performed for both the VG pair and the single VG on a flat plate cases. The results are included in figures 5.9 and 5.10, and allow separation of the effects of the **u** interpolation and **f** redistribution on the model's performance.

The obtained results indicate that the choice for Ω_{VG} is the main source of difference

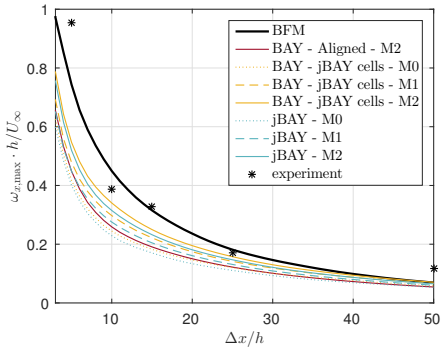

(a) Peak vorticity - VG pair on flat plate

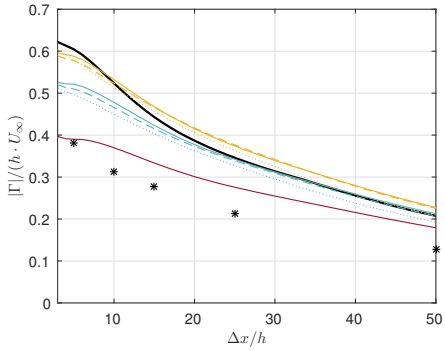

(b) Circulation - VG pair on flat plate

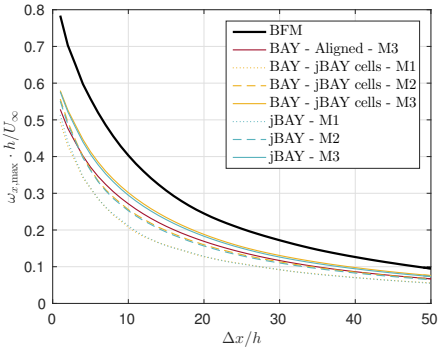

(c) Peak vorticity - Single VG on flat plate

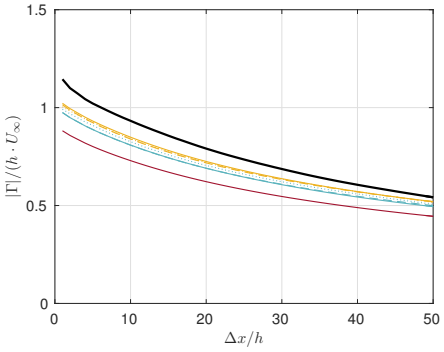

(d) Circulation - Single VG on flat plate

Figure 5.9: Effect of the jBAY cell selection and formulation on the flow-field's vorticity levels.

between the jBAY model and the original BAY model, and not the interpolation and redistribution modifications. When comparing the results of "BAY - jBAY cells" with "BAY - Aligned", and "BAY - jBAY cells" with "jBAY", it is clear that the variation in source-term domain yields a change in results that is more than twice as large as the change due to interpolation and redistribution. The importance of the source-term region definition was also observed in section 5.2.

In chapter 6, integrated source-term data are presented (table 6.1) that give an overview of the total force added to the considered source-term simulations. Whereas this force is little influenced by mesh refinement, an increase of Ω_{VG} yields a significant increase in $|\mathbf{F}|$. These observations suggest that a certain total force is required to align the flow in a specific region of the domain with the VG direction. Furthermore, this total force seems to be directly related to the created circulation in the flow. The addition of cells where the BAY model is applied effectively increases the region where the flow direction is to be altered, and therefore more source-term forcing is required to effectuate this change. Due to the resulting increase in circulation, the peak vorticity also rises. Moreover, because the source term is now distributed over a wider region, a larger part of the boundary layer is disturbed, as seen from the shape-factor profiles in figure 5.10.

The effect of the interpolation and redistribution formulations on the generated flow

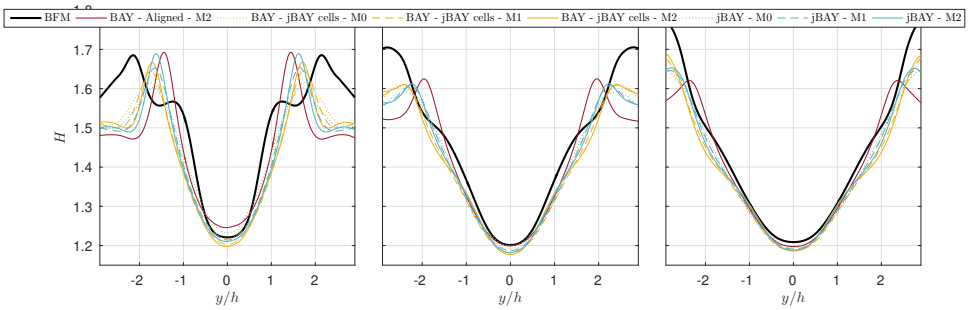

(a) VG pair on flat plate

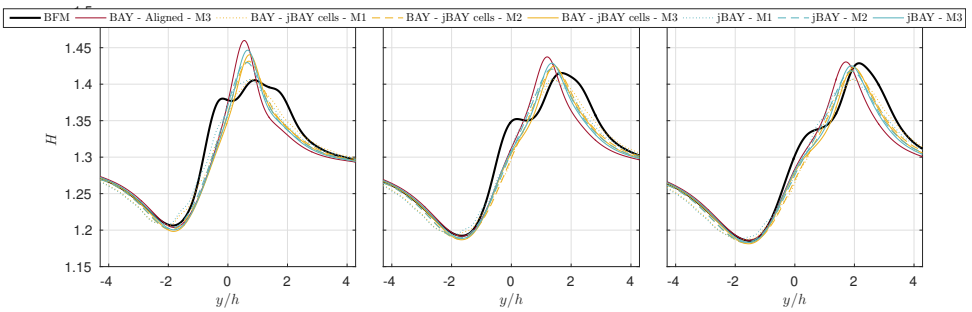

(b) Single VG on flat plate

Figure 5.10: Shape-factor profiles for the BAY and jBAY models, at (from left to right) $\Delta x = 5h$, $\Delta x = 10h$ and $\Delta x = 15h$ behind the VG's TE.

field consists of a reduction in overall vorticity levels, and hence the strength of the created vortex. Both the total circulation and the peak vorticity in the vortex core are clearly decreased (figure 5.9) in comparison to application of the BAY model on the same Ω_{VG}. This can be explained by observing that the jBAY model aims to align the flow with the VG direction in a smaller region due to the location where flow tangency is evaluated, which is now consistent at the zero-thickness virtual-VG surface. A smaller force and less circulation is thus required to achieve the desired change in flow direction. Due to this overall decrease in circulation, the peak vorticity also drops. Moreover, the interpolation and redistribution procedures of the jBAY model cause the applied source term to be more concentrated towards the actual VG location, which results in a slightly smaller region of the boundary layer being disturbed (figure 5.10).

Overall, isolation of the two factors that cause the jBAY model to differ from the BAY model, consisting of the mesh-dependent Ω_{VG} selection and the mesh-independent interpolation and redistribution, indicates that the former is dominant in both the jBAY's accuracy and mesh-convergence behavior. Additional interpolation and redistribution to ensure a consistent location of the virtual VG does not affect the results upon mesh refinement. Hence, the remaining source of mesh dependency in the jBAY formulation, the variation of V_{tot}, seems to be dominant and thereby prevents a fully mesh-independent flow field from being achievable. It therefore follows that for the original BAY model variation of V_{tot} is also the main source of mesh dependence.

5.4. CONCLUSIONS

The analysis presented in this chapter reveals the presence of model errors in both the BAY and the jBAY models, in the sense that they consistently under-predict the vortex intensity and create erroneous shape-factor profiles when compared with body-fitted mesh simulations. Moreover, the vortex center is typically located too far on the VG's suction side.

It is found that both the mesh resolution and the source-term region strongly influence the obtained result, with the effect of the latter being largest. Hence, for the BAY model, calibration by means of varying Ω_{VG} is advised in order to achieve an accurate representation of the amount of flow mixing generated by the presence of a VG.

The main modification related to the jBAY model was found to consist of aligning the source-term domain with the actual VG direction, and using a width of two cells. This choice for Ω_{VG} indeed seems to yield the most reliable results in the absence of high-fidelity reference data to perform calibration.

The interpolation and redistribution parts of the jBAY model, however, have not been observed to yield the expected reduction in mesh dependency of the model. Our results indicate that the effect of this addition on the generated flow field is limited, and manifests itself as a small decrease in overall vorticity levels.

6

INFLUENCE OF SOURCE-TERM PARAMETERS

In the previous chapter an analysis of the BAY and jBAY models was presented, which revealed shortcomings of these models in representing the boundary-layer disturbance caused by the presence of a VG. The cause of these deviations was however not identified. In this chapter therefore a closer look is taken at the source term that is added to the governing equations to represent the VG effect. The effects on the created flow field of the total force added to the simulation by the source term and its distribution are investigated (section 6.2), after which the importance of magnitude and direction of the total applied forcing are studied in more detail in section 6.3. To this end, first several modified source-term formulations are introduced in section 6.1. The main findings of this assessment are summarized in section 6.4.

6.1. RATIONALE OF THE ANALYSIS

The aim of this part of our investigation consists of assessing the impact of different aspects of the source-term field that is added to the governing equations in order to represent the effect of VGs on the flow. The aspects that are studied here are the distribution of the source-term field over the selected cells and the resultant total force that is imposed on the flow by the source term, where the latter is further divided into the effects of the magnitude and the direction of this resultant force. In particular, with this analysis we want to gain insight into which are the most influential parameters of the source-term field, and to improve our understanding of the underlying mechanisms that govern the creation of a vortex by the addition of a source term. Eventually, we expect this new insight to be helpful in focusing future research efforts towards the development of improved models that minimize (or even eliminate) shortcomings of existing BAY-like models, as discussed in chapter 5.

So far, in this work we have focused our attention on existing partly-modeled/partly-resolved reaction-force models that aim to achieve flow tangency in the neighborhood

of the VG, in particular the BAY and the jBAY model. Assessment of these models is performed using body-fitted mesh simulations as reference, which are considered to yield the best result achievable within the limitations of the selected numerical framework.

Five additional source-term formulations, based on the BAY model and the actual reaction force a VG imposes on the flow, are now introduced in order to isolate the considered source-term parameters. These formulations are first discussed below, and then used in the analysis presented in the following sections. The comparisons which will be considered are illustrated in figure 6.1.

6.1.1. ADDITIONAL SOURCE-TERM FORMULATIONS

Uniform $\mathbf{F}^{\mathbf{BAY}}$ In this formulation a uniformly-distributed source term is locally added to the momentum equation such that the source-term forcing per unit volume is constant over the selected cells (Ω_{VG}), and such that the total applied force equals the total force added to the flow by the BAY model. Hence, in the domain Ω_{VG} a source term

$$\mathbf{f}_i^{UB} = \frac{V_i}{V_{tot}}\mathbf{F}^{BAY} \qquad \text{with} \qquad \mathbf{F}^{BAY} = \sum_{i=1}^{N} \mathbf{f}_i \tag{6.1}$$

is applied, where N equals the number of cells in the source-term region and $\mathbf{f}_i$ represents the source-term forcing in a single cell according to the BAY-model formulation 3.11. Compared to the BAY model, this implies that the applied source term is no longer focused near the leading edge of the VG.

Uniform $\mathbf{F}^{\mathbf{exact}}$ Similar to the uniform $\mathbf{F}^{\mathrm{BAY}}$ model, a uniformly distributed source term is added to the momentum equation in the selected cells (Ω_{VG}). In this formulation, however, the magnitude and direction of the resultant applied force are obtained from the total surface force acting on the VG in a body-fitted mesh simulation. Hence, the exact total reaction force is imposed on the flow, and the applied source term equals

$$\mathbf{f}_i^{UE} = \frac{V_i}{V_{tot}}\mathbf{F}^{\mathrm{exact}} \qquad \text{with} \qquad \mathbf{F}^{\mathrm{exact}} = \oiint_{S_{VG}} \tilde{p}\,\mathbf{n}\,\mathrm{d}S, \tag{6.2}$$

where S_{VG} represents the surface of the VG, $\tilde{p}$ is the stress (pressure and viscous) acting on the VG surface for a BFM VG simulation and $\mathbf{n}$ indicates the wall-normal direction.

The main force acting on the VG's surface is due to pressure, the distribution of which is shown for the BFM VG-pair case in figure 6.2. It is apparent that the majority of the reaction force due to pressure is focused near the VG's leading edge.

(Distributed) $\mathbf{f}^{\mathbf{exact}}$ Given that the force distribution on a VG is non-uniform, formulations using non-constant source magnitudes may be advantageous. In this formulation we therefore not only calibrate the total force added to the system, but also the distribution of the source term over the cells is matched as closely as possible to the actual VG surface-force distribution. This is achieved by first calculating the VG force in every interior VG cell i of the body-fitted mesh by integration over its faces as

$$\tilde{\mathbf{f}}_i^{E} = \oiint_{S_i} \tilde{p}_i \mathbf{n}_i \,\mathrm{d}S. \tag{6.3}$$

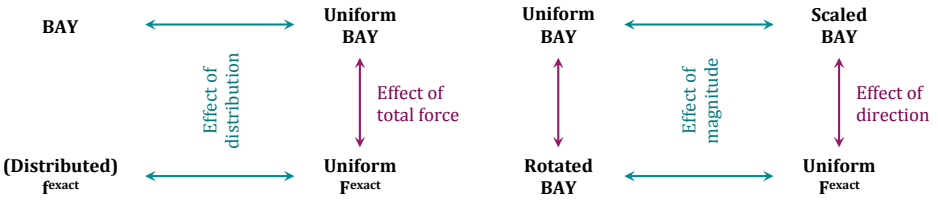

(a) Distribution versus total force analysis (b) Magnitude versus direction analysis

Figure 6.1: Illustration of the assessment approach using the modified source-term formulations.

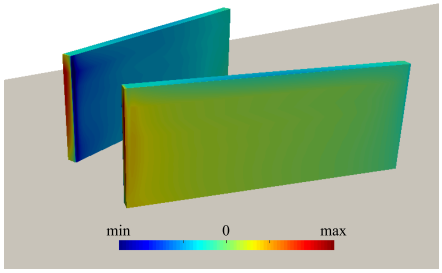

Figure 6.2: Illustration of the pressure distribution over the VG surface, as obtained from a BFM simulation.

Afterwards, this force distribution is mapped onto the uniform grid and calibrated to account for interpolation errors as

$$\mathbf{f}_i^E = \left(\tilde{\mathbf{f}}_i^E\right)_{\text{BFM}\mapsto\text{uniform}} \frac{\mathbf{F}^{\text{exact}}}{\sum_{i=1}^{N}\left(\tilde{\mathbf{f}}_i^E\right)_{\text{BFM}\mapsto\text{uniform}}}. \tag{6.4}$$

to ensure

$$\sum_{i=1}^{N} \mathbf{f}_i^E = \mathbf{F}^{\text{exact}}. \tag{6.5}$$

This distributed $\mathbf{f}^{\text{exact}}$ approach theoretically represents the highest accuracy that could be reached with a BAY-like model, as it replaces the VG geometry with exactly the force it imposes on the flow. Hence, the error related to the BAY model due to the approximation of the VG force is eliminated.

Rotated uniform $\mathbf{F}^{\text{BAY}}$ (= $\mathbf{F}^{\text{RB}}$) In order to distinguish between the relative impact of the direction (denoted as θ) and magnitude of the total force added to a simulation, two additional formulations based on the uniform $\mathbf{F}^{\text{BAY}}$ source-term formulation are introduced. The rotated uniform $\mathbf{F}^{\text{BAY}}$ formulation ('uniform $\mathbf{F}^{\text{RB}}$') represents a uniform distribution, with the total force equal in magnitude to the total force resulting from the BAY model (hence $|\mathbf{F}^{RB}| = |\mathbf{F}^{BAY}|$), but rotated into the direction of the total force as obtained

from the reference BFM simulation (such that $\theta^{RB} = \theta^{\text{exact}}$). The source-term field is thus defined as

$$\mathbf{f}_i^{RB} = \frac{V_i}{V_{tot}}\mathbf{F}^{RB} \qquad \text{with} \qquad \mathbf{F}^{RB} = \frac{|\mathbf{F}^{BAY}|}{|\mathbf{F}^{\text{exact}}|}\mathbf{F}^{\text{exact}}. \tag{6.6}$$

Scaled uniform $\mathbf{F}^{\mathbf{BAY}}$ (= $\mathbf{F}^{\mathbf{SB}}$) Similarly, the scaled uniform $\mathbf{F}^{\text{BAY}}$ formulation ('uniform $\mathbf{F}^{\text{SB}}$') represents a uniform distribution, but now with the total force scaled such that its magnitude equals the magnitude of the exact VG reaction force ($|\mathbf{F}^{SB}| = |\mathbf{F}^{\text{exact}}|$). The direction of the added forcing, however, remains equal to the result of the BAY-model simulation, hence $\theta^{SB} = \theta^{BAY}$. Therefore we have

$$\mathbf{f}_i^{SB} = \frac{V_i}{V_{tot}}\mathbf{F}^{SB} \qquad \text{with} \qquad \mathbf{F}^{SB} = \frac{|\mathbf{F}^{\text{exact}}|}{|\mathbf{F}^{BAY}|}\mathbf{F}^{BAY}. \tag{6.7}$$

6.1.2. SET-UP AND IMPLEMENTATION

The above described uniform source-term formulations were implemented in OpenFOAM® such that the user need only to specify the total forcing as additional input (hence $\mathbf{F}^{\text{BAY}}$, $\mathbf{F}^{\text{exact}}$, $\mathbf{F}^{\text{RB}}$ and $\mathbf{F}^{\text{SB}}$ for the first two and the last two formulations respectively). Specification of the source-term domain Ω_{VG} over which the source term is uniformly distributed was done as in the BAY model. Note that for these formulations the source-term field was held constant throughout the simulation.

The (distributed) $\mathbf{f}^{\text{exact}}$ source-term field, however, was calculated using an additional utility and directly read (without modification) by the modified simpleFoam solver. This utility required the construction of an additional mesh, equal to the body-fitted mesh but including the volume 'within' the VG, for the calculation of $\tilde{\mathbf{f}}_i^E$ according to 6.3. This result was then mapped onto the uniform mesh of interest, according to 6.4, using OpenFOAM®'s mapFields utility.

For the results presented in the following sections, the domain Ω_{VG} was specified using the aligned cell-selection approach. Note that in section 5.2 it was found that in general the jBAY cell-selection approach yields a better calibrated result. However, the aligned approach was chosen for this study because it is the most natural way of imposing the exact reaction-force distribution $\mathbf{f}^{\text{exact}}$, thus facilitating a convenient comparison of the relative change in result upon modification of the source-term parameters of interest (see figure 6.1), Furthermore, to minimize the effects of discretization errors, all data presented in this investigation were obtained on the finest meshes considered, unless specified otherwise.

6.2. EFFECTS OF SOURCE-TERM DISTRIBUTION AND TOTAL FORCING

To facilitate discussion of the relative impact of the source-term distribution ($\mathbf{f}$) and total imposed forcing ($\mathbf{F}$) table 6.1 was constructed, which contains data related to the total applied source-term forcing for a range of simulations (as discussed in chapter 5). The normal, tangential and wall-normal components ($\mathbf{F}_n$, $\mathbf{F}_t$ and $\mathbf{F}_b$ respectively) as well as the magnitude $|\mathbf{F}|$ of the resultant total forcing are included, as are the magnitude of the

Table 6.1: Components and magnitude of the total VG force (normalized w.r.t. $|\mathbf{F}|$), resultant forcing per unit volume ($|\bar{\mathbf{f}}|$), and direction of the total VG force (θ_{xy} and θ_z), for simulations as discussed in chapter 5. All quantities are normalized by the BFM result. "A" indicates the use of the aligned cell-selection approach, and "J" of the jBAY cell-selection approach.

Case	Model	$\mathbf{F}_n$	$\mathbf{F}_t$	$\mathbf{F}_b$	$\lvert\mathbf{F}\rvert$	$\lvert\bar{\mathbf{f}}\rvert$	θ_{xy}	θ_z
VG Pair	BFM	99%	8%	8%	100%	100%	0°	0°
	BFM (inviscid)	99%	5%	7%	99%	99%	-1.4°	-0.6°
	BAY - A - M0	86%	-4%	0%	86%	14%	-7.1°	-4.8°
	BAY - A - M1	77%	-3%	0%	77%	29%	-7.0°	-4.8°
	BAY - A - M2	69%	-3%	0%	69%	64%	-6.9°	-4.8°
	BAY - A - M3	74%	-3%	0%	74%	116%	-6.9°	-4.8°
	BAY - J - M0	125%	-8%	0%	125%	13%	-8.2°	-4.8°
	BAY - J - M1	103%	-6%	0%	103%	23%	-8.0°	-4.8°
	BAY - J - M2	99%	-6%	0%	99%	48%	-8.1°	-4.8°
	BAY - J - M3	96%	-6%	0%	96%	93%	-7.9°	-4.8°
	jBAY - M0	104%	-5%	0%	104%	11%	-7.6°	-4.8°
	jBAY - M1	92%	-5%	0%	92%	21%	-7.4°	-4.8°
	jBAY - M2	89%	-5%	0%	89%	43%	-7.6°	-4.8°
	jBAY - M3	86%	-4%	0%	86%	83%	-7.4°	-4.8°
Airfoil	BFM	-99%	2%	10%	100%	10%	0°	0°
	BFM (inviscid)	-99%	0%	8%	100%	100%	1.2°	-1.0°
	BAY - A - M1	-67%	-4%	1%	68%	15%	4.9°	-4.6°
	BAY - A - M2	-74%	-1%	2%	74%	37%	2.2°	-4.4°
	BAY - A - M3	-68%	-4%	1%	68%	74%	4.3°	-4.5°
	jBAY - M1	-74%	-7%	1%	75%	10%	6.5°	-4.7°
	jBAY - M2	-85%	-4%	2%	85%	26%	3.8°	-4.5°
	jBAY - M3	-76%	-5%	2%	77%	50%	5.1°	-4.5°
Single VG	BFM	100%	6%	5%	100%	100%	0°	0°
	BFM (inviscid)	100%	2%	4%	100%	100%	-1.9°	-0.6°
	BAY - A - M1	75%	-2%	0%	75%	14%	-4.8°	-3.0°
	BAY - A - M2	70%	-2%	0%	70%	27%	-4.7°	-3.0°
	BAY - A - M3	67%	-2%	0%	67%	56%	-4.6°	-3.0°
	BAY - J - M1	84%	-3%	0%	84%	10%	-5.3°	-3.0°
	BAY - J - M2	80%	-3%	0%	81%	20%	-5.2°	-3.0°
	BAY - J - M3	79%	-2%	0%	79%	39%	-5.1°	-3.0°
	jBAY - M1	82%	-2%	0%	82%	10%	-4.7°	-3.0°
	jBAY - M2	77%	-2%	0%	77%	19%	-4.9°	-3.0°
	jBAY - M3	75%	-2%	0%	75%	37%	-4.8°	-3.0°

average added forcing per unit volume $|\bar{\mathbf{f}}| = |\mathbf{F}|/V_{tot}$, and the deviations in total-force direction in the $x-y$ plane (θ_{xy}) and normal to the wall (θ_z). For ease of interpretation, the presented data is normalized with respect to the BFM result (which, according to the rationale behind the BAY model, corresponds to the objective). Moreover, the resultant

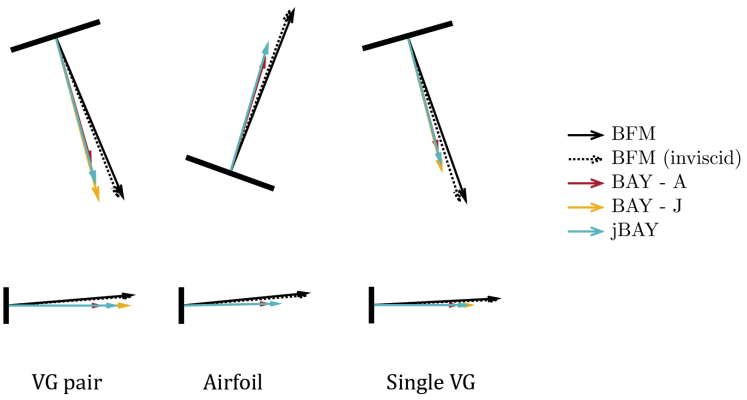

Figure 6.3: Resultant source-term forcing in the $x-y$ (top) and $x-z$ (bottom) plane for different simulation approaches and test cases. All results are obtained on the finest meshes considered in table 6.1.

forces in the $x-y$ plane, and in the plane normal to the wall, are visualized in figure 6.3, for the finest meshes considered.

When looking at the large variation in the forcing per unit volume in table 6.1, and comparing this with the relatively small variation in the obtained boundary-layer profile for the corresponding simulation results (as presented in chapter 5, see for example figure 5.10), it becomes clear that $|\bar{\mathbf{f}}|$ does not govern the success of the BAY model. This insignificance of the forcing per unit volume already gives an indication for the relative low importance of the distribution of the source term over Ω_{VG}. On the other hand, a much smaller variation in the total added force is observed from table 6.1, suggesting that instead it is $\mathbf{F}$ which governs the result obtained with a source-term approach. Moreover, these data suggest that the total VG force $\mathbf{F}$ can be used as an indicator of fidelity for the total circulation created by source-term models (see for example figure 5.9).

Upon comparison of the total VG forces in table 6.1, it follows that for most cases the BAY model under-predicts the force acting on the flow compared to the actual VG surface force obtained from the BFM simulation, with the error in magnitude varying from -38% to 25% (which reduces to a range from -27% to 4% for the jBAY model). Furthermore, an error in orientation up to 8 degrees is observed. A closer look at the force components reveals that the latter is mainly due to the large error in the tangential VG force. Comparison with the inviscid BFM force, so considering only the pressure force acting on the VG surface, illustrates that this deficit is much larger than what can be attributed to the absence of the wall-shear-stress contribution in the BAY and jBAY models.

A closer look at these force components reveals that whereas all components are typically underestimated, the largest relative deviation is in the components parallel to the VG surface (i.e. in the direction of $\mathbf{t}$ and $\mathbf{b}$). This can be partly explained by the large relative contribution of viscosity, which is neglected in the BAY model. The component along the span of the VG is even absent for the flat-plate cases. This suggests an inability of the BAY model to adequately predict crossflow and roll up over the top edge of the VG,

both of which are important flow patterns when considering low aspect-ratio geometries like typical VGs. Despite their small magnitude, these secondary components (especially $\mathbf{F}_b$, in spanwise VG direction) directly contribute to the swirling motion of the flow.

The non-negligible influence of $\mathbf{F}_t$ and $\mathbf{F}_b$ on the generated flow field is visible in figures 6.4 and 6.5, showing streamwise velocity and vorticity snapshots up to $15h$ behind the VG. When looking at the source-term model simulations, it is observed that the $\mathbf{f}^{\text{exact}}$ source term yields a strong improvement in capturing the uplifting of fluid from the wall, resulting in a boundary-layer profile and created vortex that are closer to the BFM result than the BAY model. This effect, which is also visible in the shape-factor profiles (figure 6.7) by the improved peak locations, is believed to be directly attributable to the force component in VG spanwise direction $\mathbf{F}_b$.

In contrast to the jBAY model formulation, which does not yield a change in shape-factor profile, adaptation of the total force added to the flow is thus observed to alter the shape-factor profile. However, it should be noted that, although improving the added total force seems to be very beneficial, it does not entirely resolve the deviation in shape-factor profile close behind the VG. This is shown in figure 6.7, which indicates a large spread in the results for the different methods. Even the '$\mathbf{f}^{\text{exact}}$' model does not succeed in yielding a perfect match to the BFM results. These remaining deviations may be expected to have an impact on the prediction of the overall VG effect (e.g., with respect to flow separation) as initial errors in the boundary-layer profile propagate downstream. Further research is thus required to determine how the ability of different turbulence models to predict separation is affected by the upstream velocity field introduced by vortex generators.

When additionally considering the properties of the created vortex, it is found that a large improvement is possible when the total force is closer to the actual VG force. This is for example visible in figure 6.8, showing the downstream evolution of the scalar vortex properties $\omega_{x,\max}$ and $|\Gamma|$. For both the source terms '$\mathbf{f}^{\text{exact}}$' and 'uniform $\mathbf{F}^{\text{exact}}$' improved circulation and vortex intensity are obtained compared to the BAY model simulations. This is in line with the findings from chapter 5, where it was already discussed that there seems to be a direct relation between the (magnitude of) the total imposed forcing and the generated flow circulation (see also figure 6.9). Apart from this direct and intuitive effect on the vorticity level, a positive effect on the initial circulation decay is observed. We believe that this may be attributed to the improved representation of the uplifting of the fluid layer with opposite vorticity close to the wall. In the case of the flat-plate VG-pair flow, this initial flow-field improvement for the models with exact VG force even yields a nearly perfect representation of the circulation and decay further downstream as well.

On the other hand, the distribution of the source term over the domain Ω_{VG} seems to have a smaller effect on the obtained flow field (both in terms of intensity and shape of the created vortex) compared with the total force added by the source term. This is supported by the streamwise velocity and vorticity contour plots (figures 6.4, 6.5 and 6.6), when comparing the deviation between the results for the BAY model and the 'uniform $\mathbf{F}^{\text{BAY}}$' model to the deviation between the 'uniform $\mathbf{F}^{\text{BAY}}$' model and the 'uniform $\mathbf{F}^{\text{exact}}$' model. The latter difference seems to be more pronounced. Note that in the considered cases, the variation in distribution in essence means that the source term is no longer

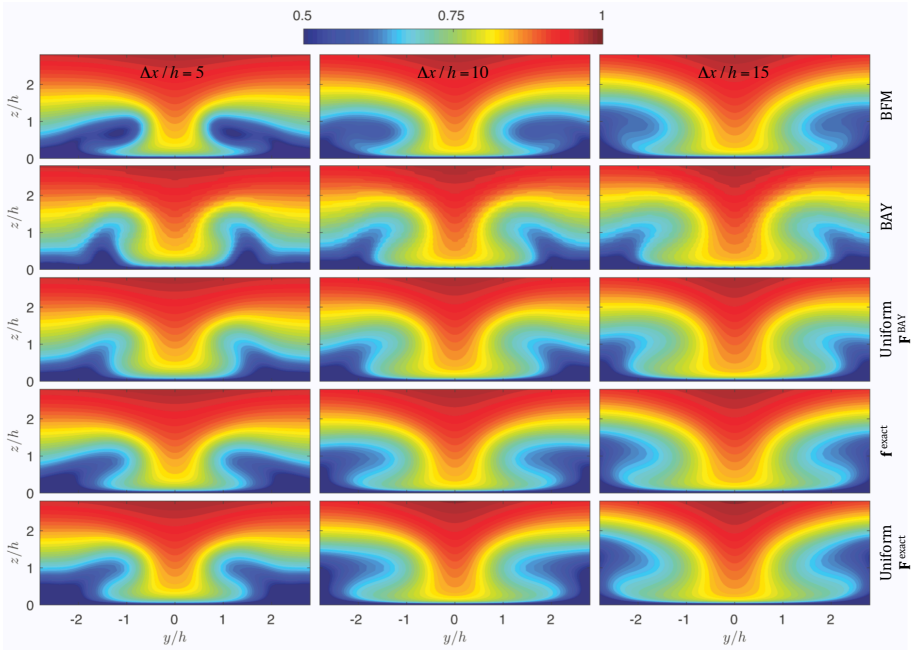

(a) Streamwise velocity (U_x/U_∞)

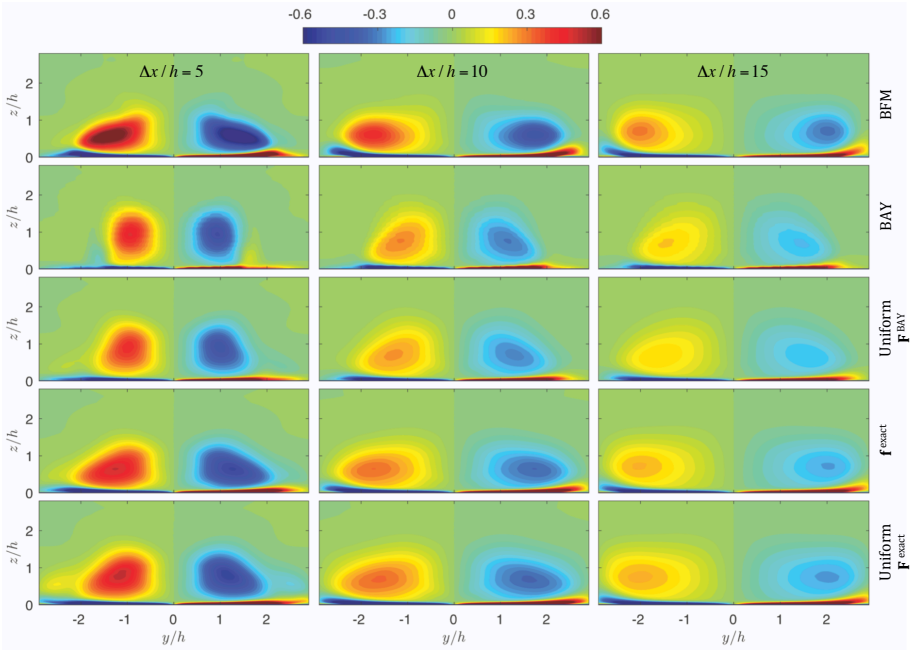

(b) Streamwise vorticity ($\omega_x \cdot h/U_\infty$)

Figure 6.4: Flow-field snapshots for several source-term formulations for the VG pair case, using mesh M3.

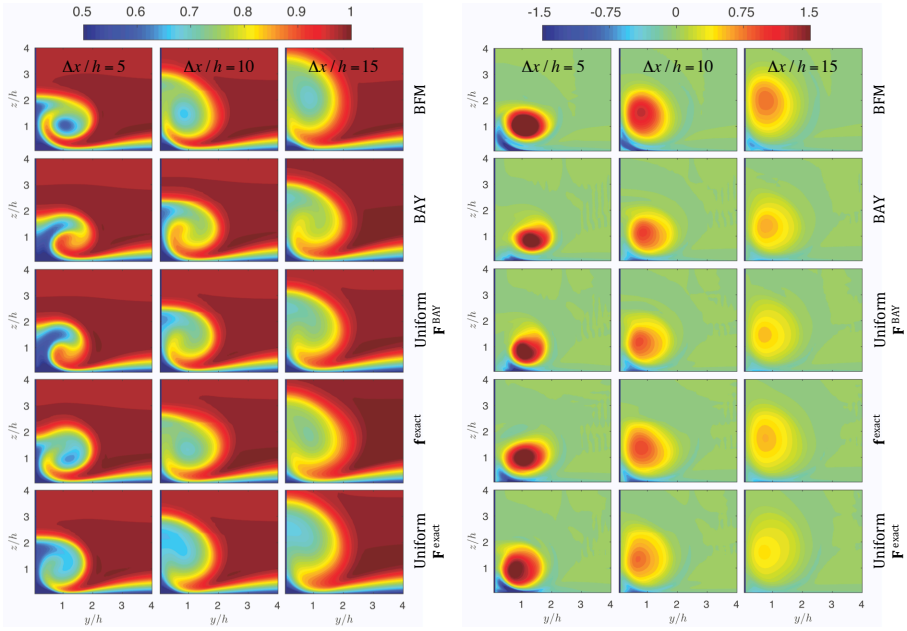

(a) Streamwise velocity (U_x/U_∞) (b) Streamwise vorticity ($\omega_x \cdot h/U_\infty$)

Figure 6.5: Flow-field snapshots for several source-term formulations for the VG on an airfoil section case, using mesh M3.

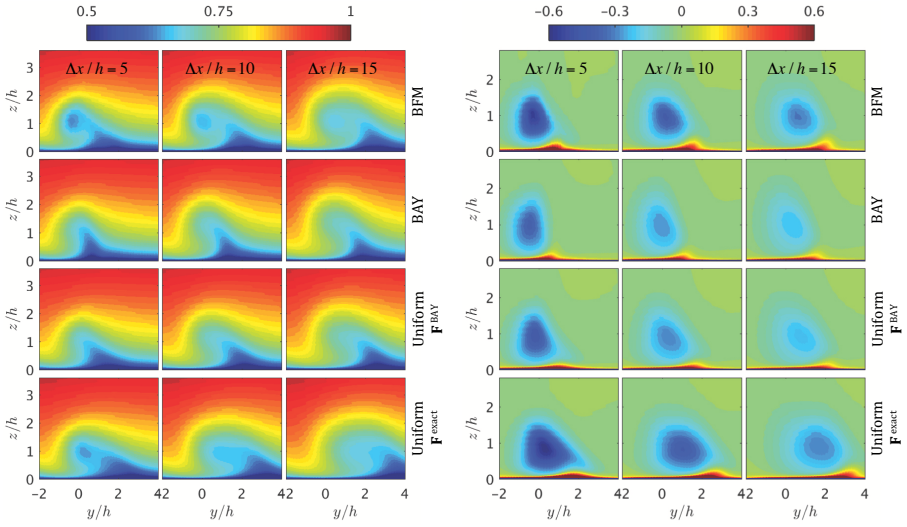

(a) Streamwise velocity (U_x/U_∞) (b) Streamwise vorticity ($\omega_x \cdot h/U_\infty$)

Figure 6.6: Flow-field snapshots for several source-term formulations for a single submerged VG on a flat plate, using mesh M3.

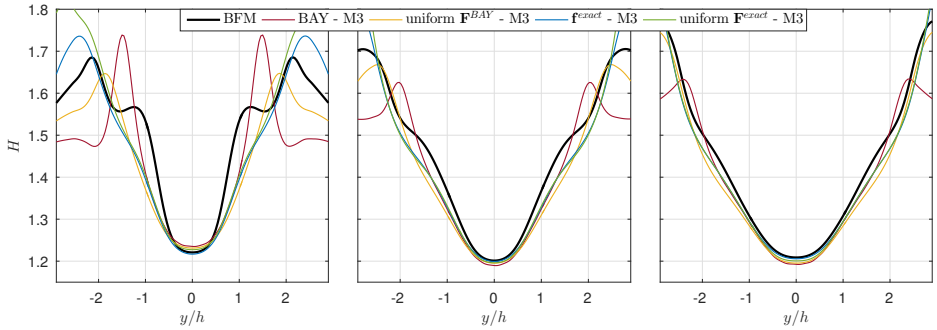

(a) VG pair

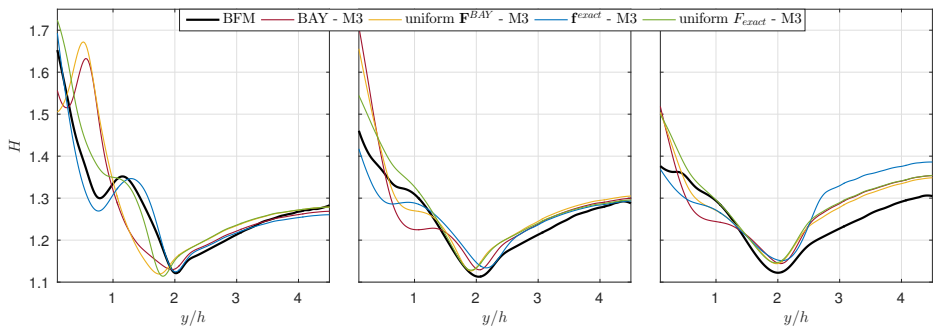

(b) Airfoil

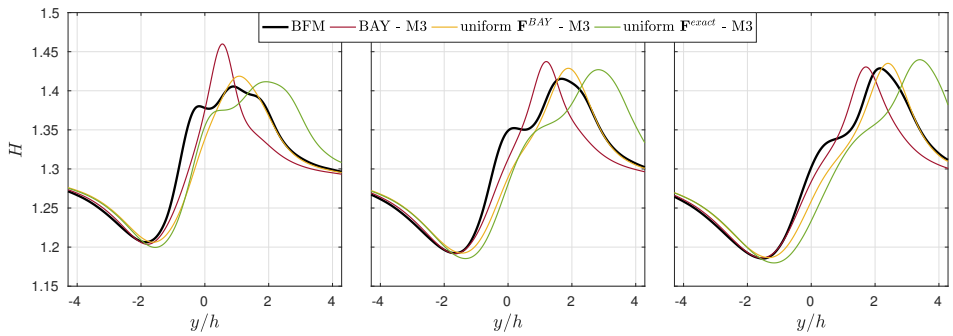

(c) Single VG

Figure 6.7: Shape-factor profiles for different simulation approaches at (from left to right) $\Delta x = 5h$, $\Delta x = 10h$ and $\Delta x = 15h$ behind the VG trailing edges.

focused near the leading edge, but is instead equally distributed over the entire domain Ω_{VG}.

Overall, our results indicate that a simple uniformly-distributed source term with the exact total-force components (uniform $\mathbf{F}^{\text{exact}}$) is able to yield a good representation of the VG-induced flow field. Improved shape-factor results are achieved compared with the BAY model (in the sense of improved peak locations), which is expected to enhance the fidelity of flow-separation predictions. Furthermore, the resulting vortex in general exhibits a shape, location and strength that is in closer agreement with the BFM result than does the vortex created by the BAY model, as especially clearly seen in the contour plots in figure 6.6.

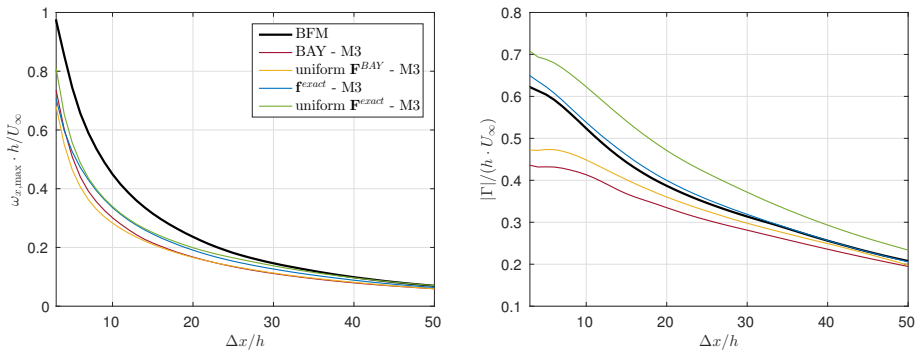

(a) Streamwise peak vorticity. (b) Circulation.

Figure 6.8: Vortex evolution downstream of a VG pair on a flat plate for different source term variations.

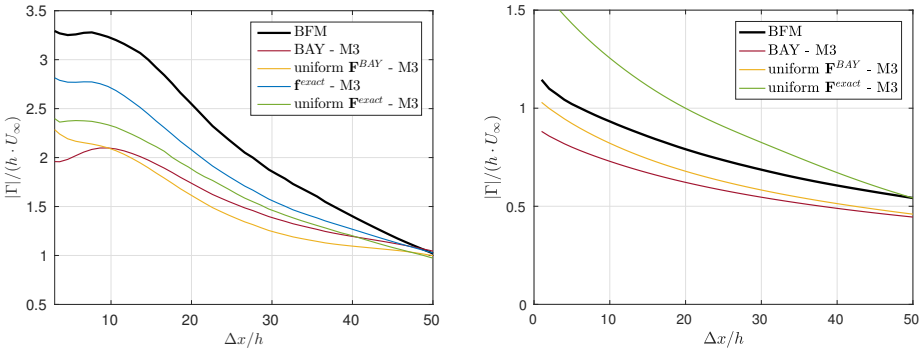

(a) Airfoil (b) Single VG

Figure 6.9: Total circulation for various source-term formulations.

6.3. INFLUENCE OF MAGNITUDE AND DIRECTION OF THE TOTAL FORCING

In the previous section it is found that the total forcing added to the simulation governs the flow field obtained with a source-term approach, rather than the distribution of this forcing over the source-term domain. To further narrow down our search towards the essential features of a successful source-term model, in this section the relative importance of correctly modeling the total force's magnitude and direction is analyzed. This is done by mutual comparison of the result obtained with four source-term variations, as introduced in section 6.1 and visualized in figure 6.1(b). Of these, 'uniform $\mathbf{F}^{\mathrm{BAY}}$' and its rotated alternative 'uniform $\mathbf{F}^{\mathrm{RB}}$' are equal in magnitude of the added forcing, as are its scaled alternatives 'uniform $\mathbf{F}^{\mathrm{SB}}$' and 'uniform $\mathbf{F}^{\mathrm{exact}}$'.

From the results presented in figure 6.10 it becomes clear that the magnitude of the total imposed source-term forcing, $|\mathbf{F}|$, is the main driver of the increased streamwise-

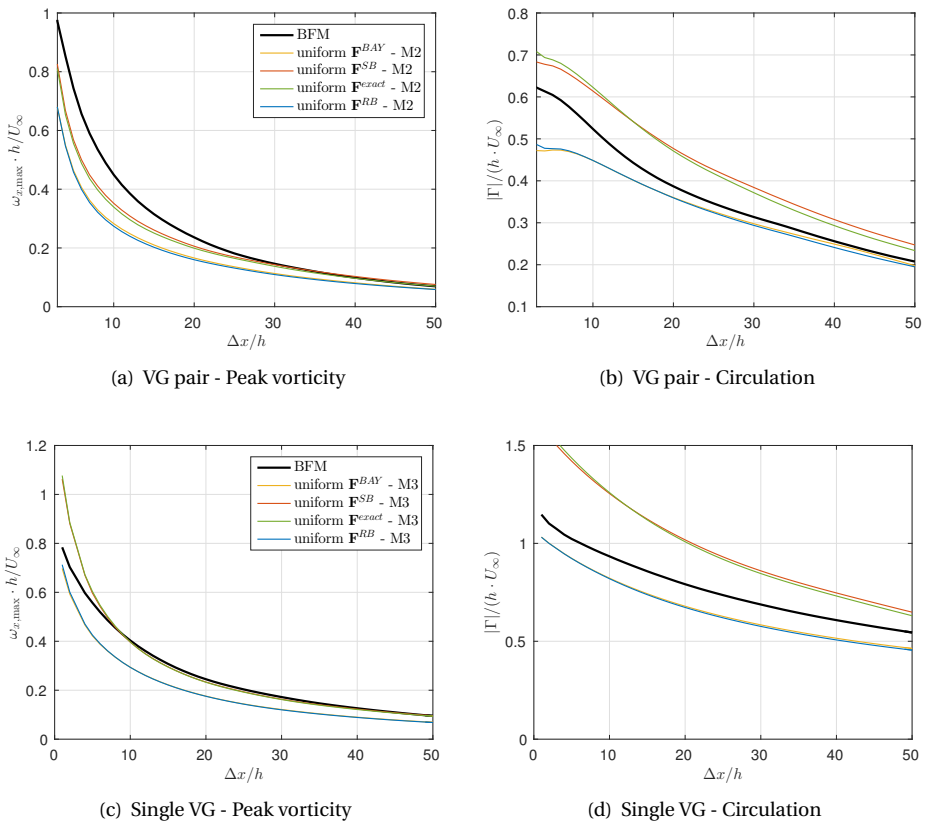

(a) VG pair - Peak vorticity

(b) VG pair - Circulation

(c) Single VG - Peak vorticity

(d) Single VG - Circulation

Figure 6.10: Effect of magnitude and direction of the resultant source-term forcing on the flow-field's vorticity levels.

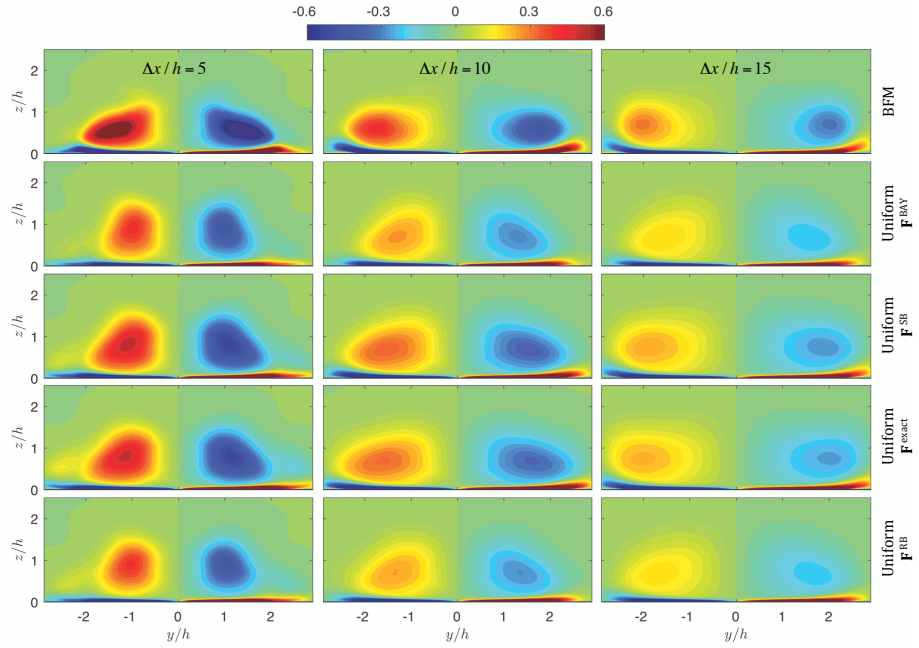

(a) VG pair (M2) - streamwise vorticity $\omega_x \cdot h/U_\infty$

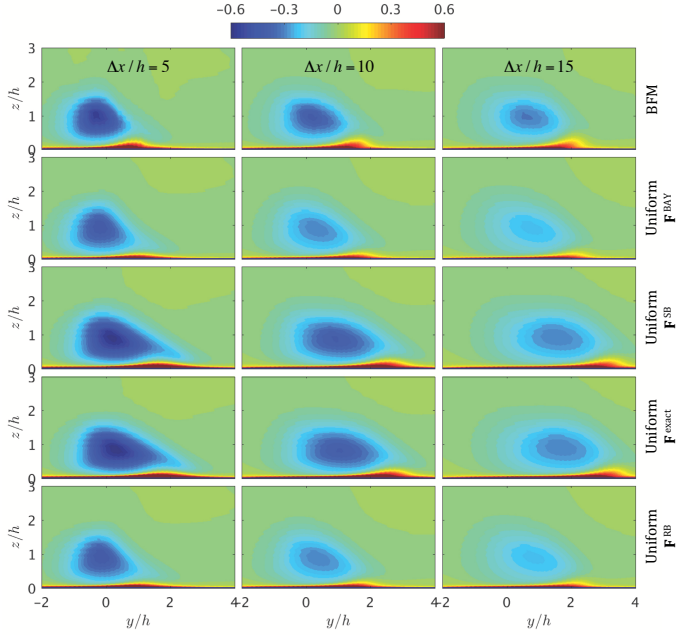

(b) Single VG (M3) - streamwise vorticity $\omega_x \cdot h/U_\infty$

Figure 6.11: Flow-field snapshots for several source-term formulations visualizing the impact of magnitude and direction of the total forcing.

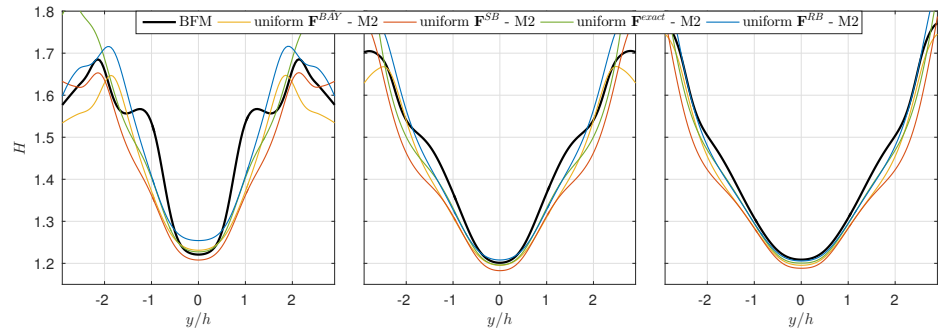

(a) VG pair

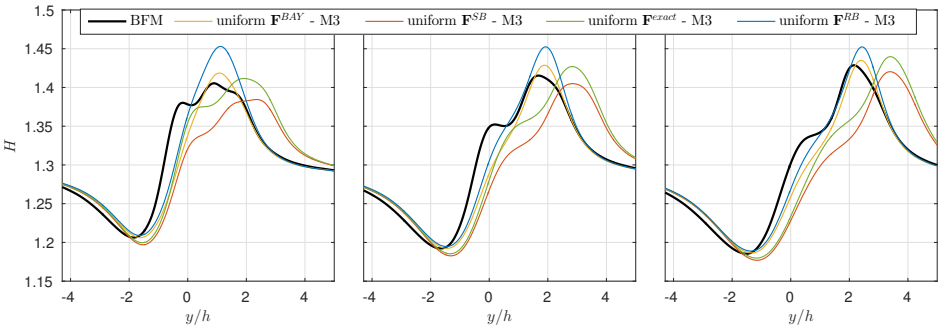

(b) Single VG

Figure 6.12: Effect of the total force's magnitude and direction on the shape-factor profile for different simulation approaches at (from left to right) $\Delta x = 5h$, $\Delta x = 10h$ and $\Delta x = 15h$ behind the VG trailing edges.

vorticity levels in the flow field. The source terms with equal magnitude also result in visually equal peak vorticity and circulation. Despite their differences in direction, a clear variation is observed with changing magnitude: a stronger vortex is created with increasing $|\mathbf{F}|$. This effect is in line with expectations, as the imposed momentum source corresponds to a local acceleration of the fluid particles in (local) crossflow direction. Thereby it directly contributes to the swirling motion of the flow and the local kinetic-energy level.

The shape-factor profiles and the flow-field snapshots (figures 6.11 and 6.12) clearly illustrate that also the shape of the obtained vortex, and hence the boundary-layer disturbance, is governed by $|\mathbf{F}|$. The effect on the size of the vortex is obvious, with the influence of the source term reaching further upon increase of $|\mathbf{F}|$ and thus causing a flow disturbance over a larger area. However, it is found that not only the size, but also the shape of the vortex is influenced by the magnitude of the imposed forcing. It is believed that this is due to the stronger interaction a stronger vortex has with the boundary layer. As was explained in section 2.3.2, this interaction introduces a stress-induced layer with opposing vorticity near the surface, which near the upflow side of the vortex may result

in the creation of a secondary vortex. Stronger interaction between vortex and boundary layer yields a stronger secondary vortex to arise, whose interaction with the primary vortex influences the (initial) shape of the latter.

The effect of rotation becomes visible when examining the obtained shape-factor profiles (figure 6.12), which show a variation in peak values upon changing direction of **F**. In practice, the presence of a VG creates a region of recirculating flow that is detached from the VG surface on the VG's suction side. This yields a streamwise momentum deficit which reflects into an increase in H. The retarding effect on the flow is captured in the uniform $\mathbf{F}^{\text{exact}}$ and uniform $\mathbf{F}^{\text{RB}}$ simulations by the source-term component acting in opposite streamwise direction. For the uniform $\mathbf{F}^{\text{BAY}}$ and uniform $\mathbf{F}^{\text{RB}}$ simulations, however, this streamwise component has decreased, yielding a smaller region with retarded flow, and thus the creation of a smaller wake.

However, the streamwise-vorticity levels are only marginally affected by small variations in the direction of the resultant volumetric forcing. For our investigation directional changes up to 7° in crossflow direction, and up to 5° in wall-normal direction, have been considered without any considerable impact on the vortex strength. Similarly, figure 6.11 indicates that also the shape and location of the created vortex are visually unaffected by the considered small variations in the direction of the resultant forcing.

The above observations can be explained by the realization that the calculated streamwise vorticity is a combination of the flow accelerations in both (freestream) crossflow directions, in our frame of reference being y and z. The considered directional changes of the resultant source-term forcing are such that an increase in $\mathbf{F}_y$ is combined with a decreasing $\mathbf{F}_z$. Even though $\mathbf{F}_y$ is the dominant component, its variation upon rotation of the resultant forcing is limited. For small rotations in the $x-y$ plane, it is found that $\mathbf{F}_y$ scales approximately with $\sin\theta_{xy}\sin\beta$. Hence, the opposing effects in y- and z-direction partially cancel each other, thereby yielding only a limited variation in streamwise vorticity. It should be noted, however, that this does not imply that the vortex properties are insensitive to rotation of the resultant source-term forcing. In reality, variations in the direction of **F** will cause the created vortex to be rotated. When studying the impact of rotation in the local crossflow plane (**n**-**b**), it is expected that a larger effect will be observed.

6.4. CONCLUSIONS

Two factors defining the BAY-model source term are investigated in more detail: the distribution of the source term over the selected cells, and the total resultant force added to the flow, where for the latter further distinction is made between magnitude and direction. The current analysis indicates that the distribution of the source term over Ω_{VG} has a lesser influence on the characteristics of the created vortex than the resultant source-term forcing, which dominates both the strength and shape of the created streamwise vortex. It is found that the magnitude of the resultant forcing is the main driver in this respect, as it directly governs the energy that is added to the system. A larger forcing magnitude yields the creation of a larger and stronger vortex. Moreover, due to the stronger interaction with the boundary layer also the vortex's shape is influenced. Small variations in the direction of the imposed forcing, however, are found to have only a limited effect on the created flow field.

In particular, the component in the VG spanwise direction $\mathbf{F}_b$, despite being small in magnitude, seems to have a significant effect on the shape of the created vortex. The large underestimation of this force component by the BAY model yields a poor prediction for the uplifting of fluid from the wall close behind the VG, and therefore directly affects the flow profile. Furthermore, the BAY model typically yields an erroneous approximation of the VG's tangential force $\mathbf{F}_t$, resulting in an underestimation of the wake created behind the VG and therefore consistently underestimating the shape-factor peaks.

The aforementioned observations with respect to the resultant source-term force and the source-term distribution are expected to be significant for a possible improvement of the BAY model. Whereas previous efforts have mainly focused on approaches to obtaining more realistic and smooth distributions of the source term over the selected domain, for example [41], our analysis indicates that a focus on the total force added by the source term could potentially be more effective in obtaining realistic flow fields with a BAY-like model. It is found that a simple uniformly-distributed source term with the exact total force components is able to yield a fair representation of the VG-induced flow field. In particular, the source-term's magnitude seems to be an important parameter to focus on, governing both the strength and shape of the created vortex.

Although this analysis has shown that for BAY-like source-term models the resultant forcing added to Ω_{VG} is the main driver for the created flow field, it is not likely that an improved estimate for $\mathbf{F}$ only, distributed uniformly over Ω_{VG}, will be able to yield optimal shape-factor profiles on a coarse mesh. Even though to a lesser extent, the distribution of $\mathbf{f}$ over the VG domain also influences the result. It is thus believed that in order to obtain highly-accurate results on coarse meshes, the combination of an improved estimate for $\mathbf{F}$ with a suitable low-resolution source-term distribution, optimized for use on a coarse mesh, will be required. Based on the presented uniform-distribution results, we envision that it might be possible to derive such a source-term formulation that only requires a low level of spatial resolution, thereby making it resolvable on coarse meshes. The BAY-like models studied in this chapter and in chapter 5 automatically concentrate the majority of the added forcing near the location of the VG's leading edge. It would thus be interesting to investigate whether, when abandoning the BAY-model formulation, such a (low-resolution) source-term field indeed exists.

7

DEVELOPMENT OF A GOAL-ORIENTED SOURCE-TERM OPTIMIZATION FRAMEWORK

The results presented in chapters 5 and 6 suggest that an improvement of current VG models is required to accurately simulate VG effects for realistic cases. Our analysis of the BAY and jBAY models has shown that these approaches perform reasonably well, creating a vortex with characteristics similar to those of a reference BFM simulation. However, also some deficiencies are observed. It is found that still a rather refined mesh is required in the vicinity of the VG, and that the vortex characteristics do not converge to the BFM results upon refinement of the mesh. Moreover, analysis of the boundary-layer shape factor revealed deviations that could indicate unreliability with respect to separation prediction. Being constrained by the use of suboptimal meshes, it is unclear whether and to which extent improvement is possible.

The questions thus arise *what is the highest accuracy one can expect to achieve when making use of a source-term model to simulate VG-induced flow effects, on a given mesh?* And *which source term is able to yield this result?* In this chapter an inverse approach is presented that makes it possible to answer both questions. The optimal source-term field, which recreates the characteristics of a given high-fidelity 3D flow field on a low-resolution mesh, is calculated by means of a goal-oriented optimization, using the continuous adjoint system. The formulation of this optimization problem is presented in section 7.1, followed by the derivation of the related continuous adjoint system in section 7.2. The expression for the sensitivity of the objective functional is derived in section 7.3, after which section 7.4 elaborates on the gradient optimization approach that allows for efficient calculation of the optimal source term. The approach presented in this chapter is tested in chapter 8, where results for the considered test cases are discussed.

Note that although the current work is focused on the simulation of VG-induced flow effects, the presented methodology is general. It can in theory also be used to find a suitable source term to replace other missing features in CFD simulations.

7.1. FORMULATION OF THE OPTIMIZATION PROBLEM

The objective of this part of our research consists of finding a source term that, on a particular low-resolution mesh, reproduces the flow disturbance caused by the presence of a VG as accurately as possible. This disturbance consists of a vortex created within the boundary layer, propagating downstream and thereby altering the boundary-layer profile.

As identified in section 4.1, the quantities of interest when analyzing this effect include the streamwise vorticity field, in particular the peak value and the evolution of the location of this peak, and its integral measure accounting for the change in overall flow circulation. If the VG is included for separation control, it is also of primary importance to accurately represent its effect on the boundary-layer shape factor, which gives an indication of the boundary layer's ability to withstand adverse pressure gradients (and hence its susceptibility to flow separation).

When looking at the definitions of these quantities in section 4.1, it becomes clear that these measures are all a function of the (local) velocity field only. This implies that a source term which provides an optimal match to the velocity field, hence without explicit consideration of other flow properties like pressure and turbulent quantities, would be sufficient to yield the highest achievable accuracy with respect to the quantities of interest. Goal-oriented optimization using an objective functional J that minimizes the l^2-norm of the deviation between the velocity field obtained with a source-term simulation, $\mathbf{u}$, and a high-fidelity reference solution $\tilde{\mathbf{u}}$,

$$J(\mathbf{u}) = \int_\Omega |\mathbf{u} - \tilde{\mathbf{u}}|^2 \, \mathrm{d}\Omega, \tag{7.1}$$

is therefore expected to be able to yield an optimal source term for representing the effect of a VG on the local flow field. The use of the general goal function $\mathbf{u}$, rather than our main quantity of interest H, ensures the flow field created by the optimal source term to be physically relevant. Moreover, the resulting source term can be expected to be more widely applicable, as it also accounts for applications of VGs other than separation control.

When considering that the velocity field $\mathbf{u}$ depends on the imposed source term, the optimal source term $\mathbf{f}^*$ that minimizes (7.1) can thus be calculated by solving the constrained optimization problem

$$\mathbf{f}^* = \arg\min_{\mathbf{f}} J(\mathbf{u}) \qquad \text{subject to} \qquad \mathbf{R}(\mathbf{u}, p, \gamma, \mathbf{f}) = 0 \qquad \text{on} \quad \Omega, \tag{7.2}$$

with γ denoting the turbulence model variables and $\mathbf{R}(\mathbf{u}, p, \gamma, \mathbf{f})$ representing the state equations and boundary conditions to be satisfied by the flow in the domain Ω. Here, $\mathbf{R}$ is defined by the incompressible Reynolds Averaged Navier-Stokes (RANS) equations, which for this purpose are written in the form

$$\mathbf{R}_\mathbf{u} = (\mathbf{u} \cdot \nabla)\mathbf{u} + \nabla p - \nabla \cdot (2\nu D(\mathbf{u})) + \mathbf{f} = 0 \tag{7.3}$$

$$R_p = \nabla \cdot \mathbf{u} = 0, \tag{7.4}$$

where $\mathbf{R} = (\mathbf{R}_\mathbf{u}, R_p)^T$, ν denotes the kinematic viscosity (comprising both the molecular and turbulent viscosity) and $D(\mathbf{u}) = \frac{1}{2}(\nabla\mathbf{u} + (\nabla\mathbf{u})^T)$ is the strain tensor. The general momentum source $\mathbf{f}$ now no longer bears a link with the BAY model, and is instead defined

in a particular cell as

$$\mathbf{f} = \begin{cases} \mathrm{diag}(\mathbf{c})\,\mathbf{f}_0 & \text{in } \Omega_{VG} \\ 0 & \text{in } \Omega \setminus \Omega_{VG} \end{cases}, \tag{7.5}$$

where diag($\mathbf{c}$) is a 3×3 coefficient matrix and $\mathbf{f}_0$ an initial (uniform) forcing which is nonzero in Ω_{VG} only, such that

$$\mathbf{f}_0 = \begin{cases} \mathbf{F}_0 / V_{tot} & \text{in } \Omega_{VG} \\ 0 & \text{in } \Omega \setminus \Omega_{VG} \end{cases}. \tag{7.6}$$

In (7.6), V_{tot} denotes the volume of Ω_{VG} and $\mathbf{F}_0$ is an initial estimate for the total forcing applied in Ω_{VG}. Optimization of the source term distribution is achieved by varying the vector of control variables $\mathbf{c}$ in each cell contained in Ω_{VG}. This approach is chosen over the direct optimization of $\mathbf{f}$ in order to prevent matrix conditioning problems due to poor scaling of the system.

To solve the constrained optimization problem, equation (7.2) is reformulated as an (easier to solve) unconstrained optimization problem using the Lagrange-multiplier method. This method implicitly enforces the optimization constraints by introducing a new functional which consists of the objective functional augmented by the product of the state constraints and their Lagrange multipliers. More information about this method, and how to use it for practical optimal-control situations, can be found in for example the work of Ito and Kunisch [38] and the first part of [72], respectively. Using the control variable $\mathbf{c}$ instead of $\mathbf{f}$, the Lagrange-multiplier method requires solving

$$\mathbf{c}^* = \arg\min_{\mathbf{c}} \mathscr{L}(\mathbf{u}, p, \gamma, \mathbf{c}, \mathbf{v}, q), \tag{7.7}$$

with the Lagrange functional

$$\begin{aligned} \mathscr{L}(\mathbf{u}, p, \gamma, \mathbf{c}, \mathbf{v}, q) &= J(\mathbf{u}) + \lambda \cdot \int_\Omega \mathbf{R}\,\mathrm{d}\Omega & (7.8) \\ &= \int_\Omega |\mathbf{u} - \tilde{\mathbf{u}}|^2\,\mathrm{d}\Omega + \int_\Omega \mathbf{v} \cdot \mathbf{R}_\mathbf{u}(\mathbf{u}, p, \gamma, \mathbf{c})\,\mathrm{d}\Omega + \int_\Omega q R_p(\mathbf{u})\,\mathrm{d}\Omega, & (7.9) \end{aligned}$$

where $\lambda = (\mathbf{v}, q)^T$, with $\mathbf{v}$ and q the Lagrange multipliers, often denoted as the adjoint velocity and adjoint pressure respectively. Note that by rewriting the constrained problem as an unconstrained problem the dimensionality of the system has increased, because we now have the adjoint variables λ as additional unknowns.

In order to find the optimal control $\mathbf{c}^*$ which minimizes $\mathscr{L}$, and for $\mathbf{R} = \mathbf{0}$ therefore also J, the necessary condition for an extremum of the Lagrange functional needs to be satisfied. This implies requiring the first-order variation $\delta\mathscr{L}$ to equal 0, hence

$$\delta\mathscr{L} = \delta_\phi \mathscr{L} + \delta_\mathbf{c} \mathscr{L} + \delta_\lambda \mathscr{L} = 0, \tag{7.10}$$

for the state variables $\phi = (\mathbf{u}, p, \gamma)^T$. The above first variations can be evaluated using the directional derivatives of $\mathscr{L}$ with respect to the state, control and adjoint variables. (7.10) therefore yields the equivalent set of optimality conditions

$$\nabla_\phi \mathscr{L}\,\delta\phi = 0, \tag{7.11}$$

$$\nabla_\mathbf{c} \mathscr{L}\,\delta\mathbf{c} = 0, \tag{7.12}$$

$$\nabla_\lambda \mathscr{L}\,\delta\lambda = 0, \tag{7.13}$$

for arbitrary variations $\delta\phi$, $\delta\mathbf{c}$ and $\delta\lambda$. Simultaneously satisfying (7.11), (7.12) and (7.13) constitutes the necessary and sufficient condition for determining a local optimum of $\mathscr{L}$. It does not, however, yield a global optimum.

Derivation of the expressions corresponding to the above optimality conditions is presented in the following sections. The expression related to the last optimality condition is however straightforward. Due to linearity of $\mathscr{L}$ in λ, (7.13) reduces to the original constraint imposed on the objective functional, requiring that the state variables satisfy the state equations. Hence, (7.13) is equivalent to solving $\mathbf{R}(\phi) = 0$.

7.2. DERIVATION OF THE CONTINUOUS ADJOINT SYSTEM

The first optimality condition, (7.11), is the most complex to solve for. Upon evaluation of the gradient of the Lagrangian with respect to the state variables, an adjoint system of equations and corresponding boundary conditions is obtained. In this work, the continuous adjoint system is derived, so that no initial assumptions with respect to the numerical discretization method are made. The applied approach is similar to the one used by Othmer [75], where a continuous adjoint formulation is derived for the purpose of topology optimization. Furthermore, other examples of the use of an adjoint-based approach for goal-oriented optimization can be found in literature. These include, for example, airfoil geometry optimization [98], control strategies for active flow control [68] and a posteriori error estimation for adaptive mesh refinement [36].

7.2.1. ADJOINT EQUATIONS

By considering that

$$\delta_\phi \mathscr{L} = \delta_{\mathbf{u}} \mathscr{L} + \delta_p \mathscr{L} + \delta_\gamma \mathscr{L} = \nabla_{\mathbf{u}} \mathscr{L}\, \delta\mathbf{u} + \nabla_p \mathscr{L}\, \delta p + \nabla_\gamma \mathscr{L}\, \delta\gamma, \tag{7.14}$$

and upon substitution of (7.9), the first optimality condition (7.11) becomes

$$\begin{aligned} \nabla_\phi \mathscr{L} \delta\phi \quad = \quad & \nabla_{\mathbf{u}} J\, \delta\mathbf{u} + \nabla_p J\, \delta p + \nabla_\gamma J\, \delta\gamma \\ & + \int_\Omega \mathbf{v} \cdot \nabla_{\mathbf{u}} \mathbf{R}_{\mathbf{u}}\, \delta\mathbf{u}\, \mathrm{d}\Omega + \int_\Omega \mathbf{v} \cdot \nabla_p \mathbf{R}_{\mathbf{u}}\, \delta p\, \mathrm{d}\Omega + \int_\Omega \mathbf{v} \cdot \nabla_\gamma \mathbf{R}_{\mathbf{u}}\, \delta\gamma\, \mathrm{d}\Omega \\ & + \int_\Omega q \nabla_{\mathbf{u}} \mathbf{R}_p\, \delta\mathbf{u}\, \mathrm{d}\Omega + \int_\Omega q \nabla_p \mathbf{R}_p\, \delta p\, \mathrm{d}\Omega + \int_\Omega q \nabla_\gamma \mathbf{R}_p\, \delta\gamma\, \mathrm{d}\Omega \quad = 0. \end{aligned} \tag{7.15}$$

The directional derivatives in the above expression can be evaluated by assuming Fréchet differentiability of $\mathscr{L}$ and by making use of the Gâteau derivative, which is defined for a function $f(\mathbf{x})$ as

$$\nabla_{\mathbf{x}} f\, \delta\mathbf{x} = \mathrm{d}f|_{\mathbf{x}}(\delta\mathbf{x}) = \lim_{\epsilon \to 0} \frac{f(\mathbf{x} + \epsilon\delta\mathbf{x}) - f(\mathbf{x})}{\epsilon}. \tag{7.16}$$

When furthermore assuming, similar to Taylor's frozen turbulence hypothesis, that both the influence of small local variations in the turbulent quantities γ on $\delta_\phi \mathscr{L}$ and the vari-

ation in γ with small local variations in $\mathbf{u}$ and p are negligible, this yields

$$\begin{aligned}
\nabla_{\mathbf{u}} J \delta\mathbf{u} &= \int_\Omega 2(\mathbf{u}-\tilde{\mathbf{u}})\cdot\delta\mathbf{u}\,\mathrm{d}\Omega, && (7.17)\\
\nabla_p J \delta p &= 0, && (7.18)\\
\nabla_\gamma J \delta\gamma &= 0, && (7.19)\\
\nabla_{\mathbf{u}}\mathbf{R}_{\mathbf{u}}\delta\mathbf{u} &= (\delta\mathbf{u}\cdot\nabla)\mathbf{u}+(\mathbf{u}\cdot\nabla)\delta\mathbf{u}-\nabla\cdot(2\nu D(\delta\mathbf{u})), && (7.20)\\
\nabla_p\mathbf{R}_{\mathbf{u}}\delta p &= \nabla\delta p, && (7.21)\\
\nabla_\gamma\mathbf{R}_{\mathbf{u}}\delta\gamma &= 0, && (7.22)\\
\nabla_{\mathbf{u}}\mathbf{R}_p\delta\mathbf{u} &= \nabla\cdot\delta\mathbf{u}, && (7.23)\\
\nabla_p\mathbf{R}_p\delta p &= 0, && (7.24)\\
\nabla_\gamma\mathbf{R}_p\delta\gamma &= 0. && (7.25)
\end{aligned}$$

Since both the objective functional and the continuity equation do not explicitly depend on the pressure, the second and penultimate terms on the right hand side of (7.15) vanish. Satisfying the first optimality condition thus requires solving

$$\begin{aligned}
\int_\Omega 2(\mathbf{u}-\tilde{\mathbf{u}})\cdot\delta\mathbf{u}\,\mathrm{d}\Omega + \int_\Omega \mathbf{v}\cdot[(\delta\mathbf{u}\cdot\nabla)\mathbf{u}+(\mathbf{u}\cdot\nabla)\delta\mathbf{u}-\nabla\cdot(2\nu D(\delta\mathbf{u}))]\,\mathrm{d}\Omega\\
+\int_\Omega q\nabla\cdot\delta\mathbf{u}\,\mathrm{d}\Omega+\int_\Omega\mathbf{v}\cdot\nabla\delta p\,\mathrm{d}\Omega=0. \qquad (7.26)
\end{aligned}$$

Using integration by parts, this can be written in the form

$$\begin{aligned}
\int_\Omega\left[2(\mathbf{u}-\tilde{\mathbf{u}})-\nabla\mathbf{v}\cdot\mathbf{u}-(\mathbf{u}\cdot\nabla)\mathbf{v}-2\nu\nabla\cdot D(\mathbf{v})-\nabla q\right]\cdot\delta\mathbf{u}\,\mathrm{d}\Omega-\int_\Omega(\nabla\cdot\mathbf{v})\,\delta p\,\mathrm{d}\Omega\\
+\int_{\partial\Omega}\left[\mathbf{n}(\mathbf{v}\cdot\mathbf{u})+\mathbf{v}(\mathbf{u}\cdot\mathbf{n})+2\nu\mathbf{n}\cdot D(\mathbf{v})+q\mathbf{n}\right]\cdot\delta\mathbf{u}\,\mathrm{d}S+\int_{\partial\Omega}(\mathbf{v}\cdot\mathbf{n})\,\delta p\,\mathrm{d}S\\
-\int_{\partial\Omega}2\nu\mathbf{n}\cdot D(\delta\mathbf{u})\cdot\mathbf{v}\,\mathrm{d}S=0, \qquad (7.27)
\end{aligned}$$

which should hold for arbitrary $\delta\mathbf{u}$ and δp that satisfy the equations of state (7.3) and (7.4). Equation (7.27) thus reduces to the adjoint momentum and continuity equations

$$\begin{aligned}
\nabla\mathbf{v}\cdot\mathbf{u}+(\mathbf{u}\cdot\nabla)\mathbf{v}+2\nu\nabla\cdot D(\mathbf{v})-2(\mathbf{u}-\tilde{\mathbf{u}}) &= -\nabla q && (7.28)\\
\nabla\cdot\mathbf{v} &= 0, && (7.29)
\end{aligned}$$

with the boundary conditions to be defined such as to satisfy

$$\int_{\partial\Omega}\left[\mathbf{n}(\mathbf{v}\cdot\mathbf{u})+\mathbf{v}(\mathbf{u}\cdot\mathbf{n})+2\nu\mathbf{n}\cdot D(\mathbf{v})+q\mathbf{n}\right]\cdot\delta\mathbf{u}\,\mathrm{d}S-\int_{\partial\Omega}2\nu\mathbf{n}\cdot D(\delta\mathbf{u})\cdot\mathbf{v}\,\mathrm{d}S=0 \qquad (7.30)$$

and

$$\int_{\partial\Omega}(\mathbf{v}\cdot\mathbf{n})\delta p\,\mathrm{d}S=0. \qquad (7.31)$$

Note that the presented derivation assumes the influence of small local variations in the turbulent quantities (for example the eddy viscosity in many RANS turbulence models) on $\delta_\phi\mathscr{L}$ to be negligible. This implies an incomplete derivative in (7.15) and therefore the obtained sensitivities (section 7.3) are no longer exact. However, this comes at

the advantage of not having to solve additional equations for the adjoint turbulence variables. Despite the possibility of large sensitivity errors [121], in general this assumption is valid for cases where the integral scales are sufficiently large compared to the smaller scales [37], hence cases with a low turbulence intensity. For example, in [23] it is shown (for a discrete adjoint approach) that the assumption of a frozen eddy viscosity yields excellent results for a high-lift airfoil case. For the sake of computational expediency, in the current work we therefore assume the applied assumption to have little impact on the determined optimum. As will be shown in chapter 8, the accuracy of the obtained results indicates that this assumption is indeed valid for our purpose.

7.2.2. ADJOINT BOUNDARY CONDITIONS

The boundary conditions that should be imposed on the adjoint variables $\mathbf{v}$ and q when solving the above derived adjoint equations (7.28) and (7.29) in a domain of interest, are to be extracted from the integral equations (7.30) and (7.31) by substitution of the corresponding boundary conditions for the state variables $\mathbf{u}$ and p. In this section, these boundary conditions are derived for the different types of boundaries encountered in our considered test problems.

WALLS AND INLET

Both the wall surfaces and the inflow boundaries are typically characterized by a fixed velocity and a zero-gradient condition for the pressure, hence

$$\mathbf{u} = \text{constant} \qquad \text{and} \qquad \nabla p = 0. \tag{7.32}$$

This condition on $\mathbf{u}$ implies $\delta\mathbf{u} = 0$ such that on these boundaries (7.30) reduces to

$$\int_\Gamma 2\nu\mathbf{n} \cdot D(\delta\mathbf{u}) \cdot \mathbf{v} \, \mathrm{d}S = 0. \tag{7.33}$$

Furthermore, since (7.31) should hold for arbitrary δp, it immediately follows that along the wall and inflow boundaries we have

$$\mathbf{v} \cdot \mathbf{n} = v_n = 0. \tag{7.34}$$

(7.33) thus becomes

$$\int_\Gamma \nu\mathbf{n} \cdot \left[\nabla\delta\mathbf{u} + (\nabla\delta\mathbf{u})^T\right] \cdot \mathbf{v}_t \, \mathrm{d}S = 0, \tag{7.35}$$

which is satisfied for all $\nabla\delta\mathbf{u}$ if we require the tangential component of the adjoint velocity, $\mathbf{v}_t$, to be zero as well.

For the considered state boundary conditions, the boundary integral equations (7.30) and (7.31) do not yield a necessary condition for the adjoint pressure q. Similar to [75] we therefore exploit the similarity between the state and adjoint equations, and use $\nabla q = 0$. The adjoint boundary conditions along the wall and inflow boundaries thus become

$$\mathbf{v} = 0 \qquad \text{and} \qquad \nabla q = 0. \tag{7.36}$$

OUTLET

At the outlet of the domains the flow is required to be parallel to the surface, and we prescribe a constant value for the pressure. The boundary conditions for the state variables at the outlets are therefore

$$(\mathbf{n}\cdot\nabla)\mathbf{u} = 0 \qquad \text{and} \qquad p = \text{constant}. \tag{7.37}$$

The latter implies that $\delta p = 0$ such that (7.31) is automatically satisfied. Furthermore, it is shown in [75] that the terms in (7.30) containing the rate of strain tensor D are equivalent to

$$2\nu\mathbf{n}\cdot[D(\mathbf{v})\cdot\delta\mathbf{u} - D(\delta\mathbf{u})\cdot\mathbf{v}] = \nu\left[(\mathbf{n}\cdot\nabla)\mathbf{v}\cdot\delta\mathbf{u} + (\mathbf{n}\cdot\nabla)\delta\mathbf{u}\cdot\mathbf{v}\right], \tag{7.38}$$

such that (7.30) becomes

$$\int_\Gamma \left[\mathbf{n}(\mathbf{v}\cdot\mathbf{u}) + \mathbf{v}(\mathbf{u}\cdot\mathbf{n}) + \nu(\mathbf{n}\cdot\nabla)\mathbf{v} + q\mathbf{n}\right]\cdot\delta\mathbf{u}\,\mathrm{d}S - \int_\Gamma \nu(\mathbf{n}\cdot\nabla)\delta\mathbf{u}\cdot\mathbf{v}\,\mathrm{d}S = 0. \tag{7.39}$$

Because $\mathbf{u}+\delta\mathbf{u}$ should satisfy the boundary condition for $\mathbf{u}$, we also obtain the requirement $(\mathbf{n}\cdot\nabla)\delta\mathbf{u} = 0$, such that the last integral in (7.39) cancels. The adjoint boundary conditions are thus to be obtained from the requirement

$$\mathbf{n}(\mathbf{v}\cdot\mathbf{u}) + \mathbf{v}(\mathbf{u}\cdot\mathbf{n}) + \nu(\mathbf{n}\cdot\nabla)\mathbf{v} + q\mathbf{n} = 0. \tag{7.40}$$

Decomposition of the above expression into its normal and tangential components yields

$$\mathbf{v}\cdot\mathbf{u} + v_n u_n + \nu\mathbf{n}\cdot\nabla v_n + q = 0 \tag{7.41}$$

$$u_n\mathbf{v}_t + \nu\mathbf{n}\cdot\nabla\mathbf{v}_t = 0, \tag{7.42}$$

from which respectively the adjoint pressure q and the tangential component of the adjoint velocity, $\mathbf{v}_t$, at the outlet boundary can be obtained. The adjoint boundary conditions for the outlet are closed by considering the adjoint continuity equation (7.29), which implies that

$$(\mathbf{n}\cdot\nabla)\,v_n = -\nabla\cdot\mathbf{v}_t. \tag{7.43}$$

TOP

Along the boundary on the top of the considered domains zero-gradient requirements hold for both state variables, hence

$$(\mathbf{n}\cdot\nabla)\mathbf{u} = 0 \qquad \text{and} \qquad \nabla p = 0. \tag{7.44}$$

Similar to the outlet boundary, this condition for the velocity implies that the adjoint pressure and tangential velocity should satisfy (7.41) and (7.42), respectively. However, in this case the boundary conditions can be closed by the requirement for p, which, similar as for the wall and inlet boundaries, implies from equation (7.31) that

$$v_n = 0 \tag{7.45}$$

along the top boundary.

SIDES

Finally, for all considered cases the side boundaries parallel to the freestream direction (x) act as symmetry planes, thereby simulating the effect of neighbouring VGs in order to create a VG array. A symmetry condition is also imposed for the adjoint variables.

7.3. GRADIENT OF THE OBJECTIVE FUNCTIONAL

As last remaining optimality condition the variation of the Lagrangian with respect to the control variable $\mathbf{c}$ is considered. Since (7.12) should be satisfied for arbitrary variations $\delta\mathbf{c}$, this reduces to

$$\nabla_{\mathbf{c}} \mathscr{L} = 0. \tag{7.46}$$

Given that (7.13) is satisfied, it follows that this condition is equivalent to

$$\nabla_{\mathbf{c}} J = 0, \tag{7.47}$$

thus yielding an optimum for the objective functional J.

With the state and adjoint solutions known, the sensitivity of the objective functional to changes in the control variable $\mathbf{c}_i$ in a particular cell i can be calculated as

$$\begin{aligned}
\nabla_{\mathbf{c}_i} J &= \nabla_{\mathbf{c}_i} \mathscr{L} \\
&= \int_\Omega \mathbf{v} \cdot \nabla_{\mathbf{c}_i} \mathbf{R}_{\mathbf{u}}(\mathbf{u}, p, \mathbf{c}) \, \mathrm{d}\Omega \\
&= \int_\Omega \mathbf{v} \cdot \nabla_{\mathbf{c}_i} \left(\mathrm{diag}(\mathbf{c})\, \mathbf{f}_0 \right) \mathrm{d}\Omega \\
&= \int_\Omega \mathrm{diag}(\mathbf{v}_i)\, \mathbf{f}_{0_i} \, \mathrm{d}\Omega \\
&= \mathrm{diag}(\mathbf{v}_i)\, \mathbf{f}_{0_i} V_i,
\end{aligned} \tag{7.48}$$

with V_i the volume of cell i. In combination with a gradient-optimization algorithm (see section 7.4) the above obtained gradient can subsequently be used to calculate the optimal $\mathbf{c}^*$ that yields a minimum in J.

Despite the cost of having to solve the additional system of adjoint equations, the advantage of the methodology described in sections 7.1, 7.2 and 7.3 is that it allows for the direct calculation of the gradient of the objective functional with respect to the control variable. As $\nabla_{\mathbf{c}_i} \mathscr{L}$ is inexpensive to calculate, this implies that with only the computational cost equivalent to two state equation solves one is able to obtain the necessary sensitivity information to use a gradient optimization algorithm to calculate $\mathbf{c}^*$, and therefore also the optimal source term $\mathbf{f}^*$.

7.4. GRADIENT OPTIMIZATION APPROACH

7.4.1. OVERVIEW

The optimality conditions defined by (7.11), (7.12) and (7.13) must all be satisfied at an optimum. In [87] a one-shot approach is proposed, solving for all three conditions simultaneously using a reduced SQP-type method. Despite some promising results, the most straightforward and widely used approach consists of first solving the system of

state and adjoint equations (consisting of (7.3), (7.4), (7.28) and (7.29), in combination with the related boundary conditions) and using the gradient of the cost functional (7.48) in an outer gradient optimization loop [71, 75, 98].

In [71] several limited-memory quasi-Newton line-search optimization methods are tested in the context of DNS-based optimal control of turbulent flows. It was found that the L-BFGS approach performed best among the tested methods, requiring the smallest overall computational cost, with the damped L-BFGS method being most efficient. The latter is attributed to its small numerical overhead per iteration, compensating for the larger number of required iterations due to its less accurate Hessian approximation, compared with standard L-BFGS.

In this work, however, we prefer the use of a trust-region (TR) optimization method instead of a line-search method. As the majority of the computational cost is attributed to the evaluation of the objective functional, requiring the solution of the state system, a low number of iterations is considered more important than the overhead of the iterative scheme per iteration. Furthermore, TR methods are generally more robust when dealing with nearly singular systems[73]. We therefore make use of a TR inexact-Newton optimization scheme, in combination with a modified conjugate-gradient (CG) algorithm due to Steihaug[99], and approximating the Hessian matrix with the L-BFGS method. The latter is a low memory variation to the Broyden-Fletcher-Goldfarb-Shanno (BFGS) updating scheme, reconstructing the Hessian every iteration using only the gradient information of the most recent iterations. The implementation of the components of our optimization method is similar as outlined in [73]. An overview of the steps involved is presented below in section 7.4.2 and visualized in figures 7.1 and 7.2.

It should be noted that this TR optimization approach is only able to find a local optimum. Moreover, by the choices we make for the shape of the source term, both through the selection of Ω_{VG}, where $\mathbf{f}$ is to be applied and optimized, and through our choice for $\mathbf{f}_0$ as (7.5), we impose a restriction on the achievable accuracy. Hence, it might be possible that a source term with a different initial shape than studied in this work yields a source term that is more effective in reproducing the reference flow field. For example, in theory a source term that is defined in every cell of the domain would be more effective in minimizing J. However, such a source term would be impractical for the application of VG models.

7.4.2. DETAILS OF THE TRUST-REGION OPTIMIZATION METHOD

Both line-search methods and trust-region methods generate an update of the control variable based on a quadratic model of the objective function. Whereas line-search methods use this model to determine a suitable step direction, trust-region methods first determine the region around the current iterate in which this quadratic approximation is reliable, then choosing the update such as to minimize the approximate model within this trusted region. A common choice for the quadratic approximation, which is also used in this work, is

$$m_k(\mathbf{p}) = f(\mathbf{x}_k) + (\nabla f(\mathbf{x}_k))^T \mathbf{p} + \frac{1}{2}\mathbf{p}^T B_k \mathbf{p}, \tag{7.49}$$

where $f(\mathbf{x}_k)$ denotes the objective functional, $\mathbf{p}$ the step to update $\mathbf{x}$ such that $\mathbf{x}_{k+1} = \mathbf{x}_k + \mathbf{p}_k$, and B_k a symmetric matrix which is typically chosen to be the (approximate)

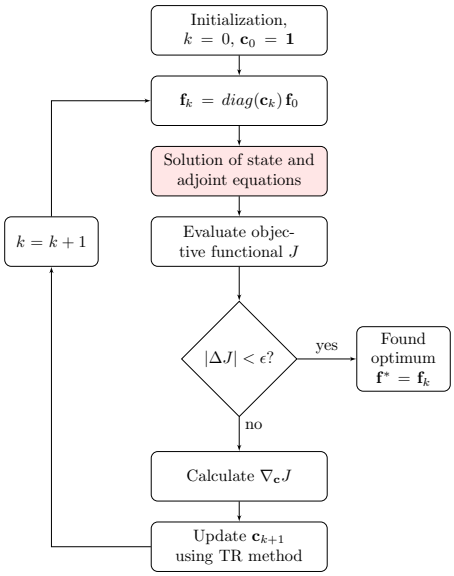

Figure 7.1: Overview of the source-term optimization implementation. The computationally most expensive part consists of the state and adjoint system solves, indicated in red.

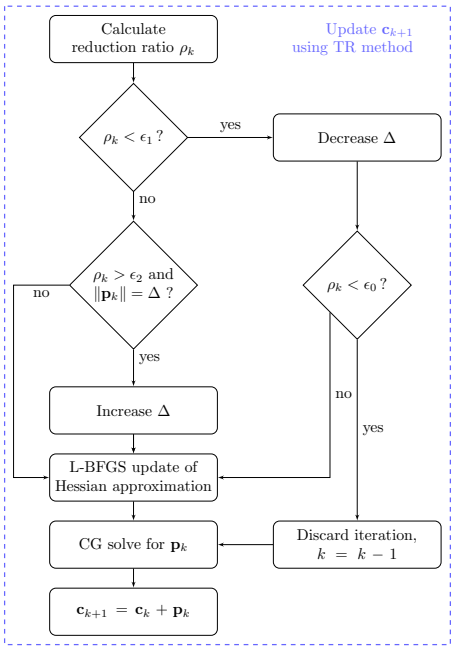

Figure 7.2: Steps involved in the TR Newton CG optimization approach to update the control vector $\mathbf{c}$. The reduction ratio ρ is defined as the ratio between the achieved and predicted reduction in J, and is used to determine whether the trust-region size Δ should be reduced or increased, where $0 < \epsilon_0 < \epsilon_1 < \epsilon_2 < 1$.

Hessian. The gradient of the cost functional, $\nabla f(\mathbf{x}_k)$, corresponds to the gradient calculated in section 7.3. Using this approximation, the next iterate can thus be constructed using a step that minimizes the quadratic approximation and falls within the trusted region. Hence,

$$\mathbf{p}_k = \arg\min_{\mathbf{p}_k \in \mathbb{R}^n} m_k(\mathbf{p}) \qquad \text{such that} \qquad \|\mathbf{p}_k\| \leq \Delta_k, \tag{7.50}$$

with Δ_k denoting the trust-region radius at iterate k.

A crucial step in trust-region methods is the determination of the size of the trust region, which governs to a large extent the convergence rate. This trust-region radius Δ is based on the agreement between the real and predicted reduction of the objective functional for a certain step, quantified as the reduction ratio

$$\rho_k = \frac{f(\mathbf{x}_k) - f(\mathbf{x}_k + \mathbf{p}_k)}{m_k(0) - m_k(\mathbf{p}_k)} = \frac{f(\mathbf{x}_k) - f(\mathbf{x}_k + \mathbf{p}_k)}{-(\nabla f(\mathbf{x}_k))^T \mathbf{p}_k - \frac{1}{2}\mathbf{p}_k^T B_k \mathbf{p}_k}. \tag{7.51}$$

If $\rho_k \approx 1$ the approximate model yields a good representation of the objective functional within the trust region, such that the current trust-region radius can be increased and fast convergence is to be expected. If, on the other hand, ρ_k is small, m_k yields a poor approximation and the trust region needs to be reduced. Moreover, in the case of an increase in objective functional, characterized by a negative ρ_k, the current iterate is discarded. This process is visualized in figure 7.2.

Furthermore, the above described process requires a Hessian matrix B_k in order to construct the quadratic approximation. As no exact Hessian is available, an approximation to the Hessian is constructed using the BFGS method. When starting from an initial symmetric positive-definite matrix B_0, this method produces increasingly accurate Hessian approximations, that remain symmetric positive definite, using the updating formula

$$B_{k+1} = B_k - \frac{B_k \mathbf{p}_k \mathbf{p}_k^T B_k^T}{\mathbf{p}_k^T B_k \mathbf{p}_k} + \frac{\mathbf{y}_k \mathbf{y}_k^Y}{\mathbf{y}_k^T \mathbf{p}_k}, \tag{7.52}$$

where $\mathbf{y}_k$ represents the change in gradient between subsequent iterations, hence $\mathbf{y}_k = \nabla_{k+1} f - \nabla_k f$. The approximate Hessian matrix has size $n \times n$, with n the total number of control variables (hence $n = 3N_{VG}$ with N_{VG} the number of cells in the source-term domain Ω_{VG}).

Since n quickly grows with mesh refinement and the size of Ω_{VG}, the Hessian update according to 7.52 can become expensive to calculate, thereby slowing down the source-term optimization. It is thus worthwhile to limit the memory requirements by using a low-memory variant of the BFGS updating scheme instead. Following [73], we therefore construct a Hessian approximation using the m most recent iterates for $\mathbf{p}_k$ and $\mathbf{y}_k$ as

$$B_k = \delta_k I - \begin{bmatrix} \delta_k S_k & Y_k \end{bmatrix} \begin{bmatrix} \delta_k S_k^T S_k & L_k \\ L_k^T & -D_k \end{bmatrix}^{-1} \begin{bmatrix} \delta_k S_k^T \\ Y_k^T \end{bmatrix}, \tag{7.53}$$

where

$$\delta_k = \frac{\mathbf{y}_{k-1}^T \mathbf{y}_{k-1}}{\mathbf{p}_{k-1}^T \mathbf{y}_{k-1}}, \tag{7.54}$$

S_k and Y_k denote the $(n \times m)$-matrices

$$S_k = \begin{bmatrix} \mathbf{p}_{k-m} & \dots & \mathbf{p}_{k-1} \end{bmatrix} \qquad \text{and} \qquad S_k = \begin{bmatrix} \mathbf{y}_{k-m} & \dots & \mathbf{y}_{k-1} \end{bmatrix}, \tag{7.55}$$

and L_k and D_k are respectively the lower-triangular and diagonal $(m \times m)$-matrices

$$(L_k)_{i,j} = \begin{cases} \mathbf{p}_{k-m-1+i}^T \mathbf{y}_{k-m-1+j} & \text{if } i > j, \\ 0 & \text{otherwise} \end{cases}, \tag{7.56}$$

$$D_k = \operatorname{diag}\begin{bmatrix} \mathbf{p}_{k-m}^T \mathbf{y}_{k-m} & \dots & \mathbf{p}_{k-1}^T \mathbf{y}_{k-1} \end{bmatrix}. \tag{7.57}$$

The size of the square matrix in (7.53) therefore becomes $2m \times 2m$, with m typically small, such that the required matrix inversion is cheap to evaluate. Note that this requires $\mathbf{p}_k T \mathbf{y}_k > 0$ for the matrix to be nonsingular.

Once the approximate model $m_k(\mathbf{p})$ is updated with the estimate for B_k, a next iterate can be determined by calculating the step $\mathbf{p}$ according to the trust-region subproblem (7.50). When equating the derivative of $m_k(\mathbf{p})$ to zero an explicit formula for the step $\mathbf{p}_k$ can be obtained, yielding

$$\mathbf{p}_k^N = -B_k^{-1} \nabla f(\mathbf{x}_k), \tag{7.58}$$

which for $B_k = \nabla^2 f(\mathbf{x}_k)$ corresponds to a step of unit length in the Newton descent direction. However, the step $\mathbf{p}_k$ needs to be chosen such as to be within the trust region, which is not guaranteed for (7.58). Therefore Steihaug's conjugate-gradient method [99] is used instead, which calculates an inexact Newton step by iteratively varying both the (descent) direction and step length until the residual

$$\mathbf{r}_k = B_k \mathbf{p}_k + \nabla f(\mathbf{x}_k) < \epsilon_k, \tag{7.59}$$

with $\epsilon_k = \min\left(0.5, \sqrt{\|\nabla f(\mathbf{x}_k)\|}\right) \|\nabla(\mathbf{x}_k)\|$ to enhance convergence speed. The step obtained this way is the optimal approximation to the Newton step $\mathbf{p}_k^N$ that falls within the trust region.

For the optimization problem as defined in section 7.1, the above method yields a new iterate $\mathbf{c}_{k+1} = \mathbf{c}_k + \mathbf{p}_k$. Subsequent solution of the state and adjoint equations allows the gradient of the objective functional (7.48) to be re-evaluated, until eventually $\mathbf{c}^*$ is found for which $\nabla_{\mathbf{c}} \mathscr{L} = 0$ and thus $\mathbf{f}^* = \operatorname{diag}(\mathbf{c}^*)\, \mathbf{f}_0$ is obtained.

7.5. IMPLEMENTATION

The described methodology has been implemented in the open-source CFD package OpenFOAM®. A basic shape-optimization algorithm is already contained in the package [75], which served as the starting point for our goal-oriented source-term optimization method. The steady incompressible RANS equations and their continuous adjoint counterpart are solved in a coupled fashion by making use of the SIMPLE algorithm. Once a steady-state solution is obtained, the objective functional is evaluated according to (7.1) and its gradient with respect to the control variable is calculated from (7.48). The source term is then updated using the trust-region approach, as described above in section 7.4, until a local optimum is found. This process is visualized in figure 7.1.

During the initialization step, Ω_{VG} is defined by a cell-selection method, as discussed in section 5.1.3. In the selected cells an initial forcing per unit volume $\mathbf{f}_{0_i}$ is defined, according to 7.6, based on a user defined input vector $\mathbf{F}_0$ (for each VG considered), which represents an estimate for the total forcing the presence of the VG would impose on the flow. This estimate does not need to be accurate, however, it is important that all components are non-zero. Note that the control variables $\mathbf{c}_i$ are vectors defined for the cells contained in Ω_{VG} only, yielding a total of $3N_{VG}$ controls to be optimized, with N_{VG} the number of cells in the VG domain Ω_{VG}.

8

ACCURACY AND DISTRIBUTION OF AN OPTIMAL SOURCE TERM

After the derivation of a goal-oriented source-term optimization framework in chapter 7, the present chapter demonstrates the successful application of this methodology. Flow-field results obtained with an optimized source term are presented for different domains in which the source term is applied. The results show that significant accuracy improvements are possible, compared to the conventional and modified models assessed in chapters 5 and 6. The results also highlight the differences in the source-term field which allow this to be achieved.

The present chapter starts with the rationale of our analysis approach, followed by an analysis of the achievable accuracy for various situations, and the related numerical cost (section 8.3). Afterwards, in section 8.4, the calculated optimal source terms are studied in more detail in order to identify important characteristics and similarities. Conclusions with respect to the use of a goal-oriented source term for VG-induced flow simulations are gathered in section 8.5.

8.1. ANALYSIS APPROACH

The goal-oriented source-term optimization framework, as derived and discussed in the previous chapter, was applied to the flat-plate test cases (see sections 4.4.2 and 4.4.1) in order to test the framework and to study the resulting optimal source terms. The optimization of the source term $\mathbf{f}$ was performed with respect to the flow field obtained from BFM simulations. In this work a RANS approach was used for the BFM simulations, however, the use of another high-fidelity simulation result would also be possible. The reference velocity field $\tilde{\mathbf{u}}$ consists of the projection of the BFM result onto the uniform low-resolution meshes used for the source-term simulations. It should be noted that $\tilde{\mathbf{u}}$ is not a flow-field solution of (7.3) and (7.4) on the considered low-resolution meshes. For example, due to the projection operation $\tilde{\mathbf{u}}$ is no longer guaranteed to be divergence free. A source term yielding a perfect match in velocity field, hence $J = 0$, is therefore

unlikely to be obtained. However, this "projected BFM" solution $\tilde{\mathbf{u}}$ is very similar to the actual BFM solution (as shown by the results in section 8.3). An optimal match with $\tilde{\mathbf{u}}$, which additionally satisfies the divergence-free criterion, can thus be trusted to yield an excellent representation of the actual BFM solution.

In contrast to chapters 5 and 6, where our study is mostly performed using high-resolution uniform meshes in order to assess model properties, the current study focuses mainly on the coarsest uniform meshes described in sections 4.4.2 and 4.4.1. The ultimate goal of source-term modeling is being able to simulate (VG-induced) flow effects by use of a source term without requiring mesh modifications with respect to a clean flow simulation (without VGs). Hence, in this chapter the source-term optimization is mainly performed on such desired low-resolution meshes, in order to investigate overall possibilities and limitations of the source-term modeling hypothesis. This way it can be verified whether the hypothesis stated at the end of chapter 6 (i.e. that a source term with only a low level of spatial resolution is required to achieve a highly accurate flow field) is valid.

Moreover, unlike the previously discussed source-term simulation results, all results presented in the current chapter were obtained using 2^{nd}-order upwind schemes for the convective terms in both the state and the adjoint equations. The considered numerical domains were also slightly reduced in both streamwise and wall-normal direction with respect to sections 4.4.2 and 4.4.1 in order to limit computational cost. The mesh resolutions are, however, unaltered.

For the following analysis, two different types of source-term domain, Ω_{VG}, are considered. For the first type, optimization of the source term was performed for Ω_{VG} consisting of a rectangular domain enclosing the VG (the original cell selection approach, see section 5.1.3, but with the domain extending in crossflow direction beyond the VG's leading and trailing edges). For the second type, in order to facilitate the comparison between the optimized source term and the BAY and jBAY models, the same cells used by the jBAY model were used to define Ω_{VG}. This domain corresponds to the physical location of the VG. These two Ω_{VG} selection approaches are shown in figure 8.1 and will be referred to as types A and B, and the optimal source terms calculated in these regions as OSTA and OSTB, respectively. Considering both types allows determination of the effects of the selected cells on both the source-term distribution pattern and the achievable accuracy.

Furthermore, as in the 'uniform $\mathbf{F}^{\text{exact}}$' approach of chapter 6, the surface force acting

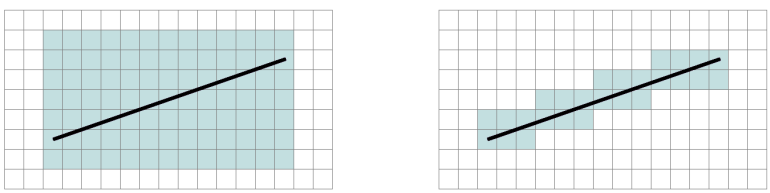

(a) Type A (b) Type B

Figure 8.1: Cell-selection types as considered for the analysis of the optimized source terms.

on the VG surface as obtained from the BFM simulations was used as $\mathbf{F}_0$ in (7.6) in order to define the initial source-term field from which to start the optimization. Subsequent assessment of the success of the optimization was performed by studying the convergence of the algorithm and the similarity of the obtained flow field (both by considering the reduction in objective function (7.1) and by inspection of the vortex and flow-field descriptors).

8.2. VALIDATION OF THE ADJOINT-BASED GRADIENT OF THE OBJECTIVE FUNCTIONAL

The adjoint-based gradient of the objective functional with respect to the source-term coefficients $\mathbf{c}_i$, defined by (7.48), was validated against finite-difference approximations for the single VG test case. As the total number of control variables is typically large ($3N_{VG}$), and finite-difference approximations require at least one function evaluation per control change, it was chosen to study the sensitivity to overall changes in the x-, y- and z-component, rather than considering the sensitivity to changes in separate cells. Therefore simulations have been performed starting from a uniform source-term distribution in Ω_{VG}, and subsequently imposing a perturbation that is equal in all cells.

When making use of finite-difference discretizations, the sensitivity of J to overall changes in the x-component of $\mathbf{c}$ can thus be approximated using both

$$\nabla_{c_x} J^{FD,c} = \frac{J(\mathbf{u}(c_x + \alpha c_x)) - J(\mathbf{u}(c_x - \alpha c_x))}{2\alpha} \tag{8.1}$$

and

$$\nabla_{c_x} J^{FD,u} = \frac{J(\mathbf{u}(c_x + \alpha c_x)) - J(\mathbf{u}(c_x))}{\alpha}, \tag{8.2}$$

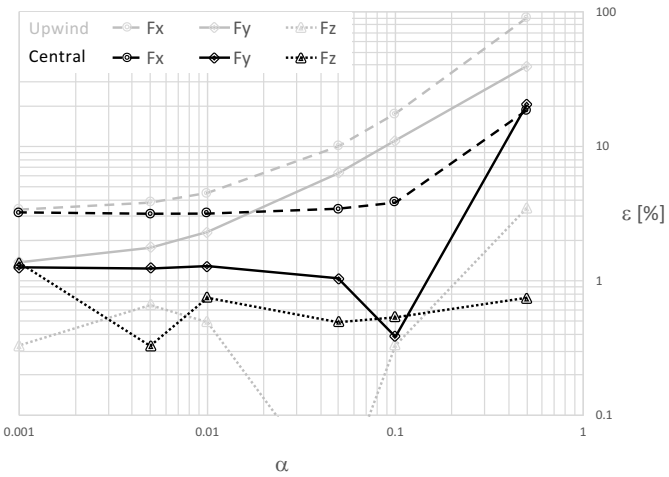

Figure 8.2: Relative difference between the adjoint-based and finite-difference approximated gradients related to the total source-term forcing in x-, y- and z-direction.

for central and upwind schemes respectively, with α the step length. Equivalently, the overall adjoint-based sensitivity to a global change in the x-component of $\mathbf{c}$ equals

$$\nabla_{c_x} J^{ADJ} = \sum_{i=1}^{N_{VG}} \nabla_{c_{x_i}} J. \tag{8.3}$$

In figure 8.2 the normalized difference between the adjoint-based and finite-difference gradients, defined as

$$\epsilon = \frac{|\nabla_{c_x} J^{FD} - \nabla_{c_x} J^{ADJ}|}{\nabla_{c_x} J^{ADJ}} \cdot 100\%, \tag{8.4}$$

is shown for different step lengths α. From these results it follows that the relative error converges to approximately 3%, 1% and 0.5% for c_x, c_y and c_z respectively. The remaining deviations are likely attributable to our use of the frozen-turbulence assumption. Overall, this validation indicates good reliability of the adjoint-based gradients, which are considered sufficiently accurate of the intended purpose.

8.3. ACHIEVABLE ACCURACY IMPROVEMENT WITH AN OPTIMIZED SOURCE TERM

In this section the results obtained with an optimized source term are presented and discussed. These were optimized with respect to $\tilde{\mathbf{u}}$, the projection of the BFM flow field onto the low-resolution meshes used for the source-term simulations, where $\tilde{\mathbf{u}}$ differs only slightly from the original high-resolution BFM result. The single VG case is used for the initial testing of the optimization framework, while the majority of the analysis is focused on the more complex VG pair case, involving the interaction between neighboring vortices. In the remainder, OSTA refers to the result obtained using an optimized source term with Ω_{VG} defined by selection type A, whereas for OSTB selection type B was used.

For both flat-plate test cases considered, a source term that significantly decreases the flow deviation with respect to the projected BFM solution was obtained for both OSTA and OSTB. This is illustrated by the objective-functional results presented in table 8.1, which contains the $J(\mathbf{u})$ values for (i) an undisturbed boundary layer (the initial condition IC), (ii) the resulting flow field when simulating the presence of VGs using the jBAY model, (iii) the flow field obtained with a source term optimized in a rectangular

		IC	jBAY	OSTA	OSTB
Single VG	M1	2.88×10^{-3}	1.34×10^{-4}	2.78×10^{-5}	3.01×10^{-5}
	M2	2.93×10^{-3}	1.09×10^{-4}	4.93×10^{-5}	5.54×10^{-5}
VG Pair	M0	2.77×10^{-4}	2.98×10^{-5}	3.84×10^{-6}	3.89×10^{-6}
	M1	2.78×10^{-4}	3.21×10^{-5}	2.63×10^{-6}	6.68×10^{-6}
	M2	2.88×10^{-4}	4.35×10^{-5}	-	1.12×10^{-5}

Table 8.1: Objective-function values J for various mesh resolutions as obtained with the jBAY model and the optimized source terms. The 'IC' result corresponds to the initial condition (clean boundary layer without VGs), before starting the optimization with J evaluated on $\Omega \setminus \Omega_{VG}$ and Ω_{VG} determined according to method B.

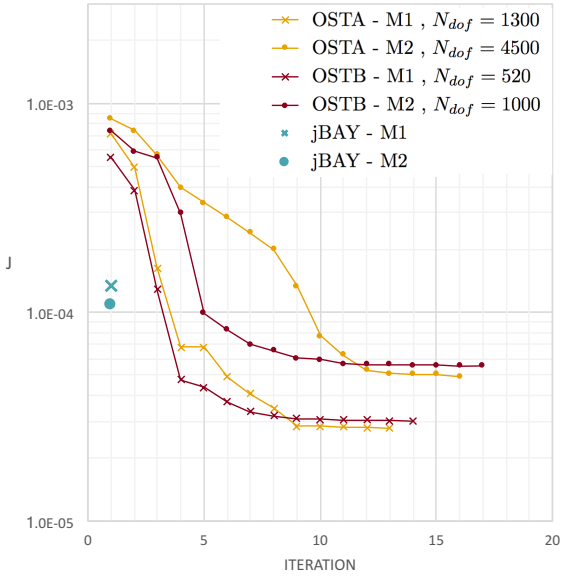

(a) Single submerged VG

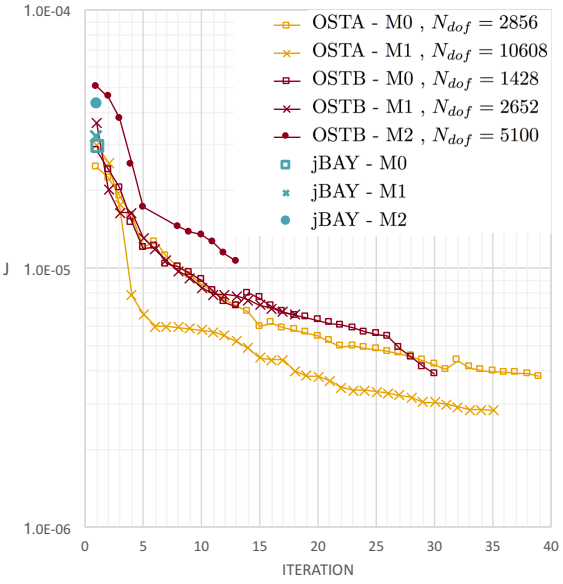

(b) VG pair

Figure 8.3: Convergence of the source-term optimization algorithm, with the computational cost related to 1 iteration approximately equal to the cost for 1 jBAY model solve.

area enclosing the VG (OSTA), and (iv) the flow field obtained with a source term optimized in the cells corresponding to the VG location (OSTB). Whereas the jBAY model has a flow deviation one order of magnitude lower than the undisturbed boundary layer, the use of a goal-oriented optimized source term is able to decrease the flow deviation by almost another order of magnitude. A much better correspondence with the BFM results is thus obtained with the optimized source terms than with the jBAY model, for all cases considered.

Furthermore, table 8.1 shows that for cell-selection type B (so both the jBAY and OSTB results) the lowest value for the objective function is obtained on the coarsest mesh and that J increases with mesh refinement. This, however, does not mean that the obtained flow field becomes a worse representation of the VG-induced flow upon mesh refinement (as can be seen in figures 8.4 and 8.7). Rather, these relatively high J values on meshes M1 and M2 are attributed to the reducing size of Ω_{VG}. Since $J(\mathbf{u})$ is evaluated on the entire domain except Ω_{VG}, for selection type B mesh refinement implies that the velocity deviation is measured in a region closer to the VG surface, where in the BFM results a boundary layer is present. This causes an increase in the overall velocity deviation, as in this region the largest differences with respect to the BFM result are found, even though the representation of the flow downstream has still improved (figures 8.4 and 8.7). This increasing J phenomenon is not observed for type A, as in that case Ω_{VG} remains constant upon mesh refinement.

The cost related to the source-term optimization is minimal, despite the large number of degrees of freedom considered (ranging from $N_{dof} = 520$ for the single VG OSTB result on mesh M1 to $N_{dof} = 10680$ for the VG pair OSTA result on mesh M1). The convergence results in figure 8.3 show that the main drop in objective function is obtained within the first 10 iterations, independent of the number of degrees of freedom. It is found that the average computational cost per iteration is approximately equal to the cost related to one flow simulation with the jBAY model. This suggests that, independent of the mesh size and the number of cells over which the source term is distributed, in general a largely improved source term can be obtained while keeping the computational cost within the cost equivalent to 10 jBAY simulations on the same coarse mesh.

Our results clearly show that a low mesh resolution does not prohibit the reproduction of a highly accuracy VG-induced flow field. For the most complex case considered, involving the interaction of two vortices emerging from a VG pair, even on the coarse mesh M0 figure 8.4 shows a much improved agreement in velocity profile, both for the dominant streamwise velocity component u_x, and the secondary rotational velocities $u_{\text{rot}} = \sqrt{u_y^2 + u_z^2}$. The low objective-function values therefore indeed indicate the creation of a physically meaningful flow field.

This is confirmed by the improved modeling of the total flow circulation and the created vortex core, shown in figure 8.5 respectively. By obtaining a higher accuracy for the circulation and the vortex-core size and location, the optimized source term approach ensures that the interaction of the vortices with the wall and their neighbors can be predicted with a high reliability.

It follows from figure 8.7 that on all considered meshes the optimized source terms therefore indeed achieve the primary goal of reducing the shape-factor error. A visual improvement of the shape-factor profiles is observed, with the extrema and inflection

points now being situated at the correct locations. Even for the coarsest mesh used to simulate the effect of a single VG (M1, with $\Delta \approx 0.7h$), a source term is obtained that yields an excellent representation of the effect of the vortex-formation process on the local boundary layer.

However, it is also observed from figure 8.7 that the shape-factor extrema are not completely resolved, and this error does not decrease with downstream distance of the VG. This is probably attributable to the limited mesh resolution, as it is clear from comparison between the VG pair results on meshes M0 and M1 that the error in the peak values is smaller for the finest mesh considered. The results also show that the choice of Ω_{VG} has an influence, although the difference between the OSTA and OSTB results reduces downstream. In the following sections, the OSTA and OSTB approaches are discussed in more detail.

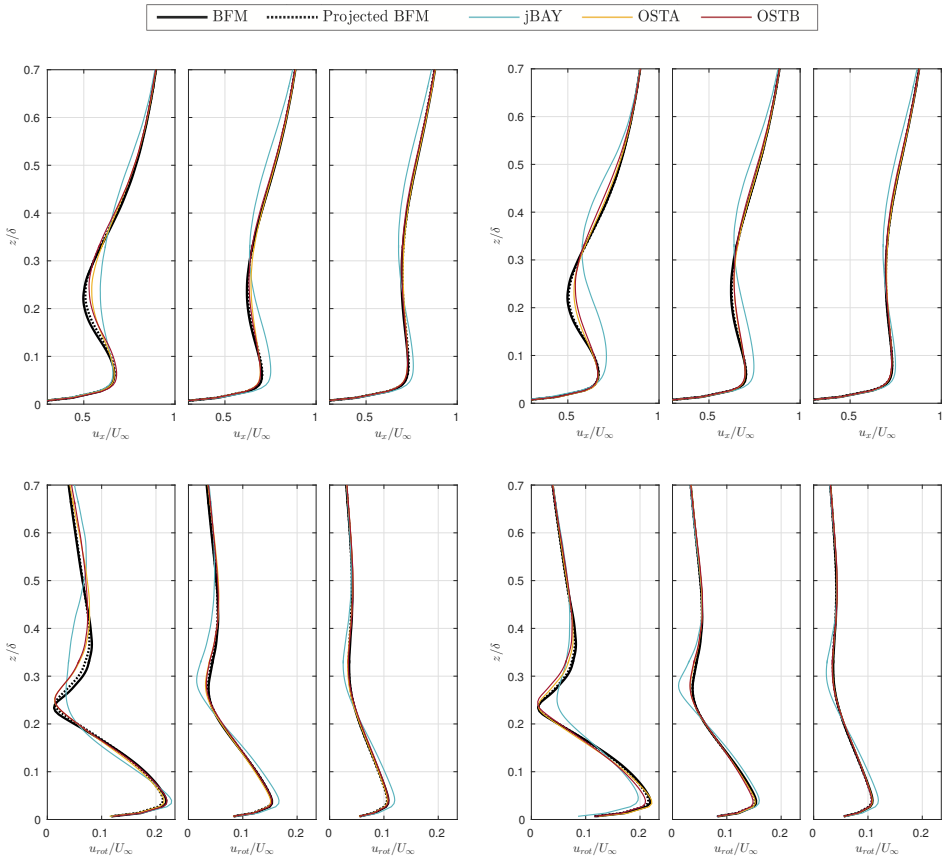

(a) Mesh M0 (b) Mesh M1

Figure 8.4: Streamwise (u_x) and rotational (u_{rot}) velocity profiles for $y = y_{TE}$ at (from left to right) $\Delta x/h = 5$, $\Delta x/h = 10$ and $\Delta x/h = 15$, VG pair case.

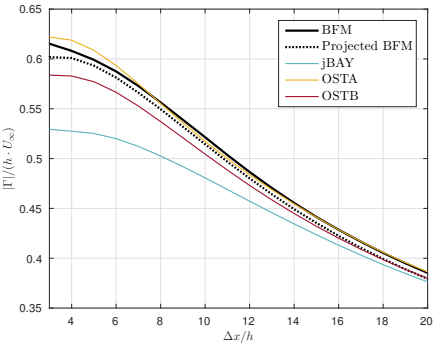

(a) Total circulation.

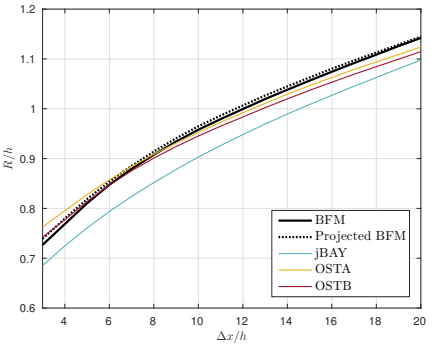

(b) Radius of an equivalent circular vortex.

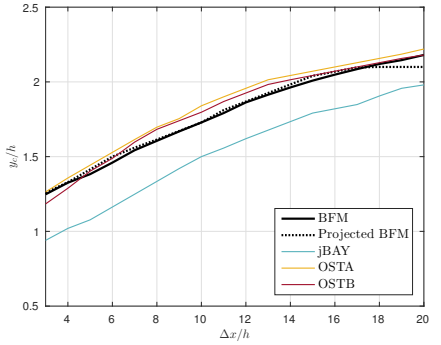

(c) Center location in y-direction.

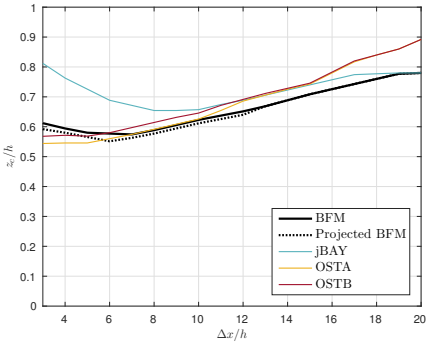

(d) Center location in z-direction.

Figure 8.5: Vortex core characteristics for the VG pair case, mesh M1.

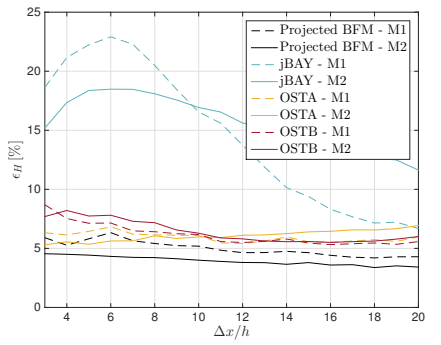

(a) Single submerged VG

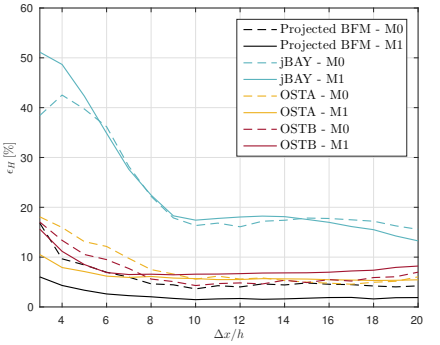

(b) VG pair

Figure 8.6: Shape-factor errors, computed as the mean deviation from the BFM result and normalized with the deviation in H with respect to an undisturbed turbulent boundary layer.

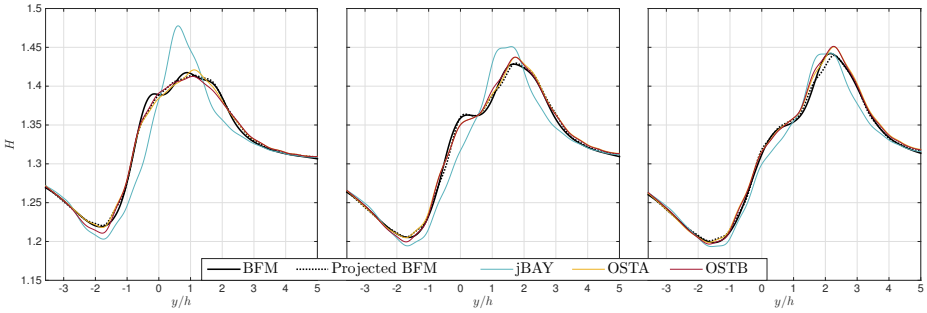

(a) Single submerged VG - Mesh M1

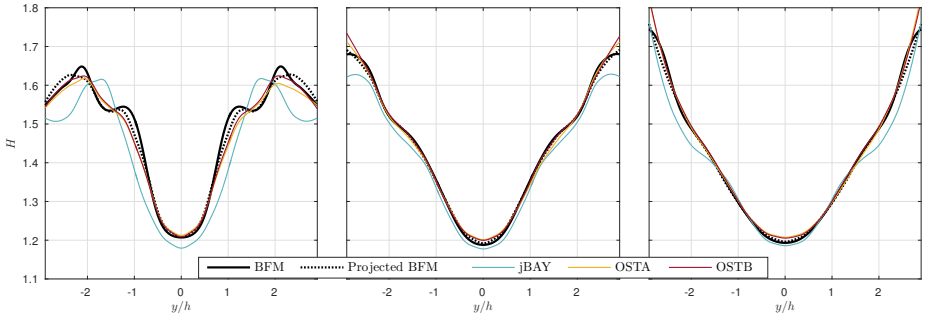

(b) VG pair - Mesh M0

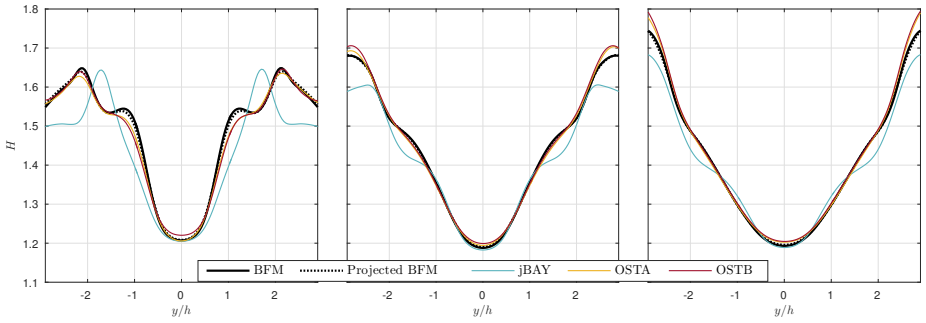

(c) VG pair - Mesh M1

Figure 8.7: Shape-factor profiles at (left to right) $\Delta x/h = 5$, $\Delta x/h = 10$ and $\Delta x/h = 15$.

Overall, the shape-factor error is reduced significantly using an optimized source term when compared to the jBAY results, even on very coarse meshes. Figure 8.6 shows that for the entire domain the error is at least halved. The largest reduction is found in the first $10h$ behind the VG pair. This corresponds to the region with the weakest interaction between the vortex core and the turbulent length scales, and therefore the region which best represents the effect of the source term. This allows to conclude that our optimization framework is successful in calculating reliable source-term distributions to represent VG effects on a wall-bounded flow, and that the frozen-turbulence assumption has not significantly impacted the results.

8.4. CHARACTERISTICS OF THE IMPROVED SOURCE TERM

8.4.1. OPTIMAL SOURCE TERM USING SELECTION TYPE A (OSTA)

OSTA is considered the most general source-term optimization approach, as Ω_{VG} can be chosen arbitrarily. In our case Ω_{VG} consists of a rectangular region enclosing the VG(s) of the test case, thereby basically being unrelated to the VG geometry. This selection method allows for a smooth distribution of the resulting source term, due to its large freedom for choosing Ω_{VG} such that the source term can be distributed over a large region. This is an interesting feature as it shows the potential for using very coarse meshes.

The OSTA source term obtained for the VG pair on mesh M1 is shown in figure 8.8, for a plane parallel to the surface and located at half the VG height. As expected, it follows that the obtained source term basically aims to impose the created vortices on the undisturbed boundary layer. For example, the component in z-direction clearly introduces the downwash typically observed between a vortex pair, whereas the component in x-direction shows similarities with the separation region on the suction side of the VGs. Although Ω_{VG} comprises the region of vortex creation, involving the most complicated flow patterns, OSTA is observed to be successful (see section 8.3), even on the coarsest mesh considered and employing a rather small Ω_{VG}.

By increasing the domain Ω_{VG}, especially in case of coarse meshes, it is expected

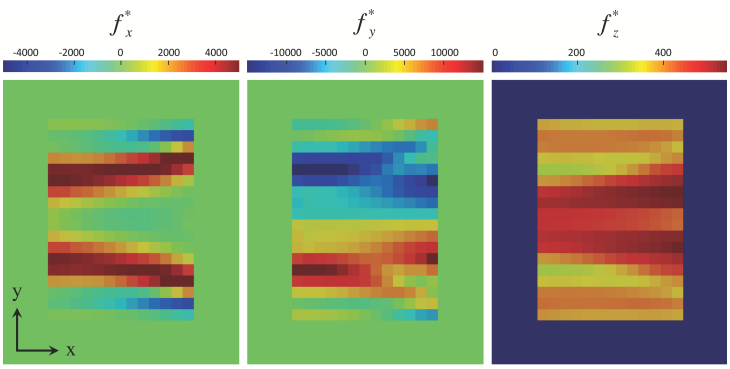

Figure 8.8: Top view of the OSTA optimal source-term components (as force per unit volume) in x-, y- and z-direction, for a plane at $z = h/2$ for the VG-pair case on mesh M1. Note that due to the sign of **f** in (7.3) the displayed body forces are opposite to their effect on the velocity field.

that the accuracy of the OSTA results can be even further improved, as the numerical diffusion can be compensated in a larger part of the domain. Hence, when considering $\Omega_{VG} = \Omega$, thus adding a source term in the entire flow domain, in theory a perfect match in flow field can be obtained. From a practical viewpoint, however, this situation is undesirable. In reality, the choice for Ω_{VG} will therefore often be a trade-off between accuracy and practicality.

Note that the obtained source term seems to be in line with the rationale behind vortex-profile VG models [20, 63], which typically impose a developed vortex profile downstream of the VG. The outstanding accuracy of the OSTA result, compared to these existing models, can be attributed to the case-specific vortex profile that is imposed (which is optimized for both the situation of interest and the used mesh). However, the inclusion of the vortex-creation process may be equally important, as it allows for a more natural and smooth adaptation of the boundary layer.

The presented OSTA results demonstrate that, with a suitable source term, even on very coarse meshes an accurate representation of a VG-induced flow field can be obtained. A relatively smooth and low-resolution (as seen from figure 8.8, the wavelengths vary from approximately 10 to 25 cells for the coarse-mesh simulation of the VG pair) was found sufficient to produce a highly accurate flow-field representation and shape-factor profiles. This indicates a potential for the future development of good (low-resolution) mesh-independent source-term fields.

Furthermore, the approach allows the assessment of whether mesh refinements are required in order to reach a specific simulation goal. Apart from the academic significance, this notion and the developed approach may (after additional research) possibly be of interest for industry, where typically flow simulations are required for large geometries including numerous VGs with a similar design (for a wind-turbine blade, for example). It is envisioned that an OSTA approach might be used as part of a multi-fidelity modeling framework, allowing for accurate source-term simulations of these large structures with minimal mesh requirements. The construction of a BFM is rather straightforward for a single VG, and the associated BFM simulation computationally inexpensive. With only minimal additional effort it may therefore be possible to calculate an optimized source term for a coarse mesh of interest. By doing this for a range of expected inflow conditions, optimal source terms could be calculated and imposed at every VG location in order to include the effect of VGs in large-scale simulations of the overall geometry of interest. This way it might be possible to obtain highly-accurate flow results at a reasonable computational cost, and without the tedious task of creating a suitable mesh for the geometry including VGs. Further research is required, however, in order to determine the feasibility of such a multi-fidelity approach, and to study the case dependency of obtained source terms.

8.4.2. OPTIMAL SOURCE TERM USING SELECTION TYPE B (OSTB)

OSTB is basically a special case of OSTA, in which the domain Ω_{VG} is limited to the cells corresponding to the VG location, as shown in figure 8.1. Apart from the reduction in degrees of freedom of the optimization problem, limiting the domain to that used by the jBAY model has the advantage of allowing investigation of the full potential of the jBAY modelling approach, and if the addition of VG surface reaction forces could result in a

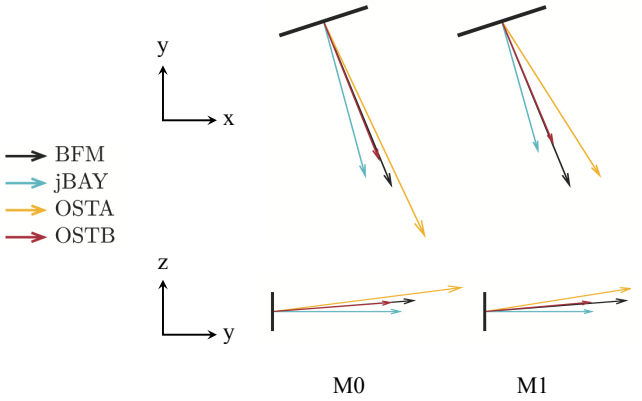

Figure 8.9: Top and side view illustrating the magnitude and direction of the resultant source term forcing.

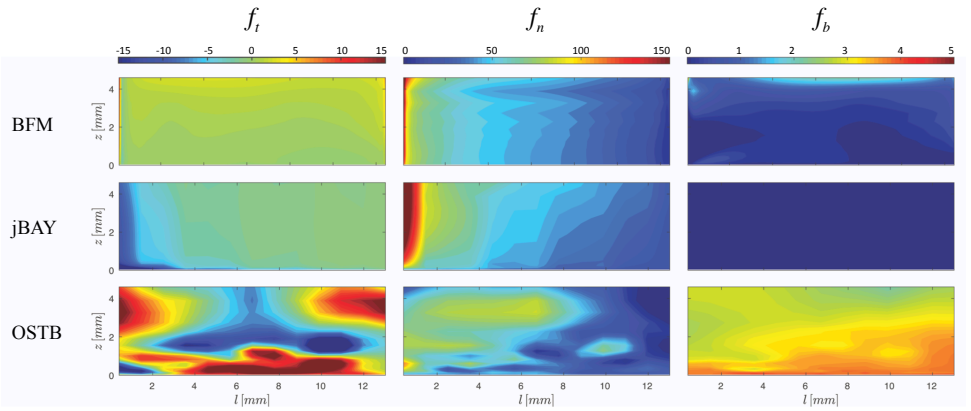

Figure 8.10: VG surface force (BFM) and the added body forces for the jBAY and OSTB simulations in tangential, normal and VG spanwise direction. The distributions show the force per unit area, which for the jBAY and OSTB result are obtained by interpolation of the source term to the virtual VG plane (VG pair, mesh M1).

suitable vortex. Due to the particular shape and limited size of Ω_{VG}, the OSTB approach does not allow for the creation of a source term that imposes a fully-developed vortex, but rather is forced to focus on the driving force that causes the creation of the vortex. Thereby the OSTB approach is a particularly useful tool in a study of the jBAY model, as it allows assessment of both the maximal attainable accuracy on a given mesh and the key features of the corresponding source term.

In section 8.3 it was shown that in general the OSTA results show the closest agreement with the objective flow fields, but that the difference with OSTB is small. This indicates that it indeed suffices to add a source term to only a small number of cells in order to generate the desired streamwise vortex, with an appropriate choice for Ω_{VG} defined by the cells that correspond to the physical VG location, similar to the jBAY model. Our

results therefore demonstrate that even on a coarse mesh, with a resolution too low to resolve the detailed flow patterns related to vortex creation, there exists a specific driving force that yields an accurate representation of the desired flow field. This is a favorable outcome, as it demonstrates the validity behind the jBAY rationale. Furthermore, selection method B in theory simplifies the analysis and description of an optimal source term due to the possibility of choosing Ω_{VG} as a 2D plane rather than a 3D volume.

Whereas the jBAY model is observed to be unable to accurately represent the shape factor, our OSTB results display a largely improved accuracy in this respect. These results suggest that an improvement for the jBAY model is both desired and possible. It is therefore worthwhile to investigate the differences in the applied source term for both these simulation approaches. For this purpose first the resultant source term is considered, the magnitude and direction of which are visualized in figure 8.9. As expected, it follows that the OSTB source term adds a resultant forcing that is nicely aligned with the exact VG surface force (as extracted from the BFM simulation). In contrast, the direction of the forcing included by the jBAY model is tilted upstream and downward (as was also observed in [26]). Counter-intuitively, the magnitude of the optimal source term is smaller than the exact VG surface force. This suggest that aiming for an exact representation of the resultant VG surface force is not the optimal approach when using an under-resolved mesh. This is confirmed by the source-term distributions, show in figure 8.10 for the VG pair using mesh M1, which are interpolated to the virtual VG plane and displayed as force per unit surface. The jBAY model clearly aims to represent the actual VG force distribution, with the focus being on the leading edge of the VG.

The OSTB result on the other hand shows a more uniform distribution of the normal force ($\mathbf{f}_n$), which is less focused on the leading edge region but spread over the front half of the virtual VG plane. Furthermore, large differences are observed in the secondary components $\mathbf{f}_t$ and $\mathbf{f}_b$, in the tangential and VG-spanwise directions respectively. Although insufficient to draw general conclusions regarding the optimal source-term layout, the presented results show that aiming for an exact representation of the VG surface-force distribution seems not to be the optimal approach for coarse meshes.

8.5. CONCLUSION

In this chapter we presented the successful optimization of the source term added to a CFD simulation in order to represent the flow effects induced by the presence of VGs. The results proved the viability of the idea to replace a physical obstacle by a local source term, for the situation of an incompressible flow over a flat plate with rectangular, vane-type VGs. It was shown that, even on a low-resolution mesh, a nearly perfect representation of the boundary layer can be achieved when only adding a source term to a limited number of cells in the neighborhood of the VG location.

Although good results were achieved for all cases considered, comparison of the source terms optimized in two different domains indicated that extension of the source-term domain Ω_{VG} has a favorable effect on the accuracy of the created flow field. On a coarse mesh a high-gradient source-term distribution is hard to resolve, and its effects are more subject to truncation errors. A smoother distribution with the same net effect, as is possible on a larger Ω_{VG}, is thus favorable, even if in that case the source term does no longer yield the closest match possible with the physical VG reaction force on the

flow. The obtained results indicated that it is not necessary to have a high-frequency source term, and to resolve all flow details close around the VG, to obtain an accurate representation of the downstream flow field. A low-resolution source-term field, which is thus resolvable on coarse meshes, may be sufficient to simulate the effect of VGs on a boundary layer.

The value of the presented optimization approach consists of its ability to determine the source term which yields the highest accuracy that can potentially be achieved with a source-term method on a given (coarse) mesh for a certain situation of interest. It may therefore be used (i) as a tool for the development of improved VG models, (ii) in order to assess whether or not mesh refinement is required for achieving a specific objective, and (iii) to obtain the specific source term that allows achieving this highly accurate result, even for unconventional VG designs. Apart from an academic point of view, with some additional research the current method is therefore also expected to be of use for industrial applications involving large VG arrays, as valuable information can be obtained by studying the simplified sub-problem of only a single VG or VG pair.

9

CONCLUSIONS & RECOMMENDATIONS

Vortex generators (VGs) are, and can be expected to remain, one of the most widely used means of passive flow control. Despite this widespread use, making reliable predictions about their effect on the local flow field, and on the performance of the object equipped with VGs, remains far from straightforward. From an accuracy point of view, fully resolved CFD simulations are preferred to study VG-induced flows. The large scale difference, in combination with the complex flow dynamics observed around a VG, however, imposes an excessive computational cost, thereby precluding this type of simulations for other than academic purposes. As an alternative, partly-modeled/partly-resolved CFD methods are typically used instead. These methods do not resolve the flow details around the VG, but rather add an external forcing locally to the simulation which triggers the formation of a streamwise vortex similar to the main vortex created by the VG. For these methods to be successful, a good understanding of the principles governing their result is a prerequisite. Still, many essential questions related to their use and accuracy remained unanswered.

9.1. CONCLUSIONS

To fill this scientific gap, this dissertation has presented a study of the impact of model formulation and simulation parameters on the VG-induced flow field obtained with partly-modeled/partly-resolved source-term CFD methods. It did so by starting from existing models and perturbing their formulation, until eventually arriving at fully optimized source-term distributions for specific cases. Given that the primal objective of VGs consists of the reduction or elimination of flow separation, the shape factor was identified as key parameter in assessing the accuracy of simulations, with accuracy defined relative to body-fitted mesh simulations.

In this dissertation it was shown that the idea of reproducing VG-induced flows by use of a coarse mesh in combination with a local source-term model is viable. Current

models were found to posses several shortcomings, causing their accuracy to be uncertain and the required mesh resolution to be still rather fine. Improvement of these models is thus desired, and as shown, possible. Case-specific optimized source terms are shown to be capable of yielding highly accurate flow fields on very coarse meshes.

9.1.1. EFFECTIVENESS OF SOURCE-TERM MODELS FOR FLOW SIMULATIONS DOWNSTREAM OF VORTEX GENERATORS

The effectiveness of the BAY and jBAY models for including VG effects in CFD simulations was investigated, which revealed the presence of model errors in both methods. For mesh resolutions approaching the body-fitted mesh resolution, significant deviations in the boundary-layer profile were observed, thus suggesting the presence of model errors that might result in poor predictions with respect to the VG effect on the flow. Our results showed a consistent under-prediction of the vortex strength and errors in the shape-factor profiles for the flow fields obtained with both the BAY and the jBAY models. Moreover, the center of the initiated vortex was found to be too far on the VG suction side, yielding deviations in the vortex path upon downstream propagation.

Both mesh resolution and the region where the source-term model is applied were found to have a large impact on the created flow field, with the effect of the latter being largest. The overall vorticity levels in the flow, and therefore the total circulation and hence amount of mixing, increase with the width (and thus size) of the source-term region. For the BAY model, the source-term region can therefore be used to calibrate the generated flow circulation, however, this will not improve the overall accuracy of the flow representation. In the absence of calibration data the jBAY source-term region, consisting of a 2-cells wide region aligned with the (virtual) VG, was found to yield the most reliable result.

Mesh dependence was observed for the results of both the BAY and the jBAY model, with a more concentrated vortex being created upon refinement of the mesh. For source-term regions that are aligned with the VG, an important source of mesh dependence was found to be the variation of the source-term region with mesh resolution, which becomes more confined with mesh refinement. The interpolation and redistribution parts of the jBAY model were not observed to yield the expected reduction in mesh dependency of the model. Our results indicated that the effect of this addition on the generated flow field is limited, and manifests mainly as a small decrease in overall vorticity level.

Analysis of factors that can be used to define a source term, indicated that the total resultant source-term forcing dominates both the strength and shape of the created streamwise vortex. The distribution of the forcing over the source-term region seems to have a lesser influence on the characteristics of the created vortex. The magnitude of the resultant forcing was found to be the main driver in this respect, governing directly the energy that is added to the flow and the strength and size of the created vortex. Also the shape of the boundary-layer profile is influenced most by the source term's magnitude, as for the same position a stronger vortex yields a stronger interaction with the boundary layer. Small variations in the direction of the resultant forcing (in the order of the difference between the BAY model's forcing and the exact VG reaction force), however, were found to have only a limited effect on the created flow field.

Comparison of the resultant forcing added to the flow by the BAY and jBAY models

with the actual VG reaction force, showed that the largest deviations occur in the tangential and VG spanwise components. The former was found to cause an underestimation of the wake created behind the VG (and therefore an underestimation of the shape-factor peaks), whereas the latter yields a poor prediction for the uplifting of fluid from the wall close behind the VG.

Overall, the analysis of modified source-term formulations revealed that a simple uniformly-distributed source term with the exact total-force components is able to yield a fair representation of the VG-induced flow field in terms of the shape, location and strength of the created vortex. However, errors with respect to the shape-factor profiles were still observed.

9.1.2. GOAL-ORIENTED OPTIMIZATION OF A SOURCE-TERM REPRESENTATION OF VORTEX GENERATORS

A goal-oriented optimization framework was presented that can be used to calculate the source term that, on a low-resolution mesh, optimally reproduces a high-fidelity VG-induced velocity field. The proposed method was successfully applied for two flat-plate cases using various low-resolution meshes.

The optimized source-term simulations proved the viability of the idea to replace a physical obstacle by a local source term, for the situation of incompressible flow over a flat plate with rectangular vane-type VGs. It was shown that, even on a low-resolution mesh, a nearly perfect representation of the boundary layer can be achieved when only adding a source term to a limited number of cells in the neighborhood of the VG location.

Distinction was made between source terms added in a region surrounding the VG, thereby imposing a specific vortex profile, and source terms added at exactly the VG location that aim to introduce a suitable driving force to initiate vortex creation. Although the rationale between these approaches differs, they both prove to be effective, with the first approach showing the largest accuracy potential.The optimal source term obtained this way was characterized by a low-wavelength distribution, thus indicating that a low-resolution source term (resolvable on coarse meshes) suffices for accurate source-term simulations of VG-induced flows.

The presented optimization framework allows determination of the source term which yields the highest accuracy that can potentially be achieved with a source term method on a given (coarse) mesh for a situation of interest. It may therefore be used (i) as a tool for the development of improved VG models, (ii) in order to assess whether or not mesh refinement is required for achieving a specific objective, and (iii) to obtain the specific source term that allows achieving this highly accurate result, even for unconventional VG designs. Apart from an academic point of view, with some additional research the developed method is therefore also expected to be of use for industrial applications involving large VG arrays, as useful information can be obtained by studying the simplified sub-problem of only a single VG or VG pair.

Finally, comparison of optimized source-term simulations with flow results obtained using the jBAY model indicates that research towards an improvement of the latter model is justified and desired. Goal-oriented source-term optimization can be useful in this endeavor, as it allows to quantify the achievable improvement and to identify the deviations of the jBAY source term from the optimal one.

9.2. OUTLOOK & RECOMMENDATIONS

Although the created body of knowledge presented in this dissertation yields a useful addition to the insights already present in literature, additional research towards efficient and accurate VG-induced flow simulations remains desired. In this view, the following recommendations originate from the current work:

- The choice to use a RANS simulation method inevitably introduces an error in the boundary-layer development, and therefore in both the initial condition for the vortex-development process, and the downstream evolution of the created vortices. These errors due to the choice of turbulence model were outside the scope of this dissertation, but are expected to have a considerable effect on the resulting flow field. Further research towards the effectiveness of different turbulence models for VG-induced flows is therefore desired, if necessary followed by the development of improved turbulence models that feature enhanced capabilities to capture the interaction between the turbulent eddies and the streamwise vortex.

  Moreover, the current study focused on the accuracy with which a source-term model can reproduce the vortex created by a VG, such as to contribute to improved flow-separation predictions. Further research is however required to determine how the ability of different turbulence models to predict separation is affected by the upstream velocity field introduced by VGs.

- In this work, reproduction of the shape-factor profile was identified as the key performance parameter when assessing the accuracy of a VG model. Especially close downstream of the VG large deviations from the BFM result were observed. However, as the vortex dissipates the shape-factor error was found to decrease. Further research is therefore desired to quantify the effect of this error on the prediction of boundary-layer separation, i.e. to define the region in which it is important to keep the shape-factor error ϵ_H low.

- The presented study towards the effectiveness of the BAY and jBAY models, and source-term models in general, to simulate VG-induced flows was performed for a small set of cases, all featuring rectangular vane-type VGs and incompressible flow. It would be interesting to extent the considered test matrix in oder to verify our findings for a larger spectrum of configurations and flow conditions, including, for example, triangular VGs and compressible flows.

- In chapter 6 it was found that a uniformly-distributed source term that features a total forcing equal to the exact VG reaction force yields fair flow-field results. This observation can serve as stimulation for research towards improved prediction methods for the total force acting on a VG in a wall-bounded flow. The availability of such predictions would allow for an alternative and simple source-term VG model. In this light, a detailed analysis of the model proposed in [79] would be interesting.

- The goal-oriented source-term optimization framework in chapter 7 was developed with the objective of obtaining a minimal deviation in the velocity field, with respect to a high-fidelity reference solution. Enhancement of the objective functional with the additional requirement of maximizing pressure-field similarity (on

the surface of application) is expected to allow for even more accurate solutions. In particular, this can be expected to yield more reliable predictions regarding the effect of VGs on the aerodynamic forces.

Moreover, the derivation and implementation of a compressible equivalent for the adjoint equations, which are now derived using the assumption of incompressible flow, is required for application to compressible flow cases.

The accuracy of the source-term optimization can be further improved by removing the frozen-turbulence assumption in the derivation of the adjoint equations. This would result in an additional set of adjoint turbulence equations. Given the good results obtained with the current optimization framework, however, we expect the related accuracy gain to be limited if the considered conditions are similar to those used in this work.

- In chapter 8, some preliminary observations with respect to optimal source-term distributions were discussed, based on two flat-plate cases. The formulation of general conclusions in this respect requires more VG-induced flow situations to be studied. In this light, it is also interesting to investigate how optimal source-terms change with varying flow and geometric input parameters, i.e. to study the case dependency of optimal source-term fields.
- The number of degrees of freedom related to the source-term optimization framework could potentially be reduced by parametrization of the source term, for example by means of modal decomposition, thereby shifting from a fully-discrete towards a continuous source-term description. Apart from optimization purposes, this approach can be further extended for the purpose of developing a reduced-order model. Application of the optimization procedure presented in this work to a wide range of cases is, however, required in order to develop a successful parametrization.
- As an alternative to the construction of (reduced-order) VG models, it is envisioned that goal-oriented source-term optimization may be of use in a multi-fidelity framework for the simulation of complex cases involving multiple VGs. When extracting the local flow conditions, BFM simulations of isolated VGs could be used to calculate the optimal source term for reproduction of the VG effect in the global simulation. Especially when only considering a limited domain around the VG (or VG pair) of interest, the cost related to the BFM simulation and subsequent source-term optimization is expected to be limited, compared to a global high-fidelity simulation. It may be interesting to study the feasibility of such an approach.

A

ADDITIONAL RESULTS RELATED TO THE INFLUENCE OF THE SOURCE-TERM DOMAIN

In this appendix some additional results related to the influence of the source-term domain on the BAY-model result are contained. The presented figures belong to the discussion in section 5.2.

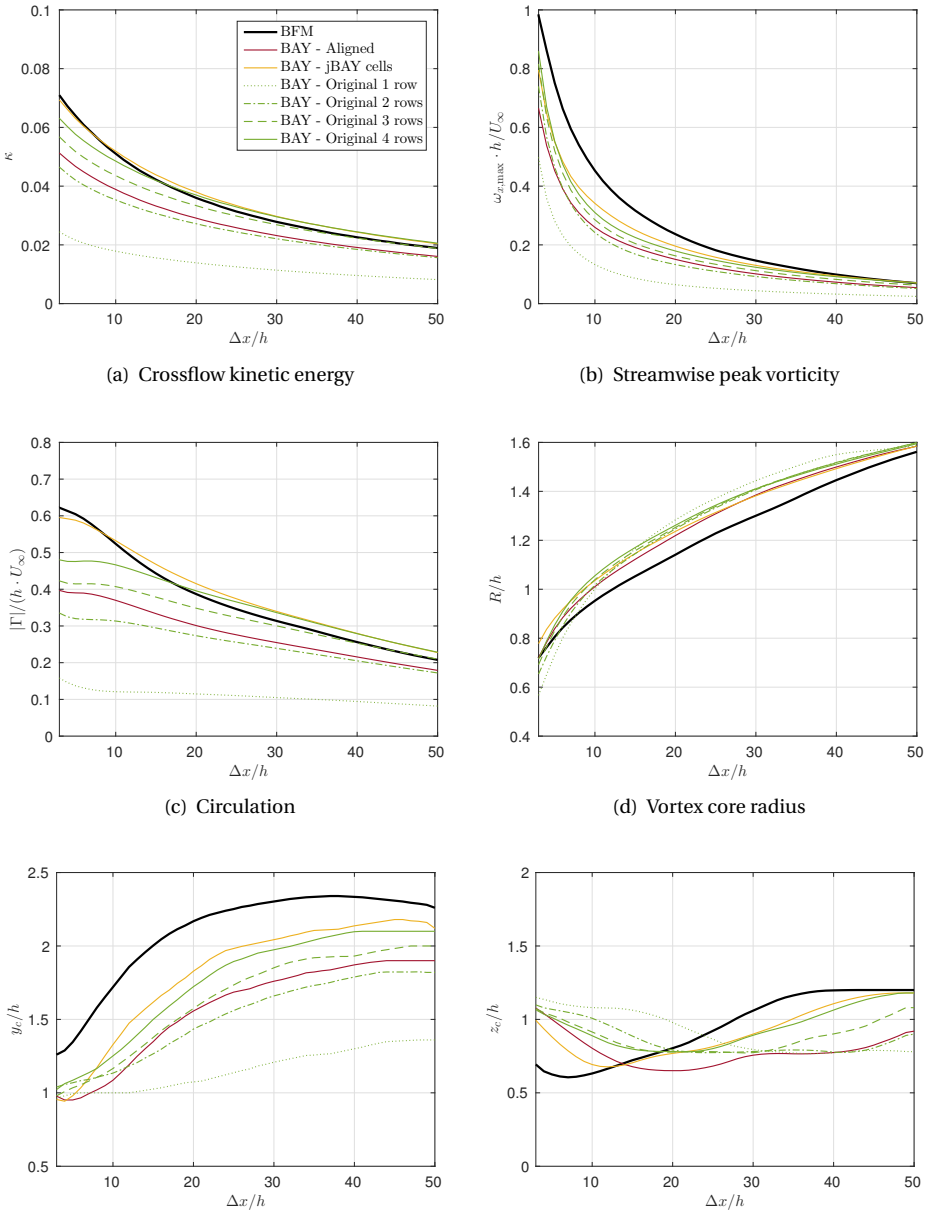

(a) Crossflow kinetic energy

(b) Streamwise peak vorticity

(c) Circulation

(d) Vortex core radius

(e) Vortex center in crossflow direction

(f) Vortex center in wall-normal direction

Figure A.1: Non-dimensionalized vortex descriptors for the flat plate with a counter-rotating VG pair test case, using the fine mesh M2, comparing the effect of different cell-selection approaches.

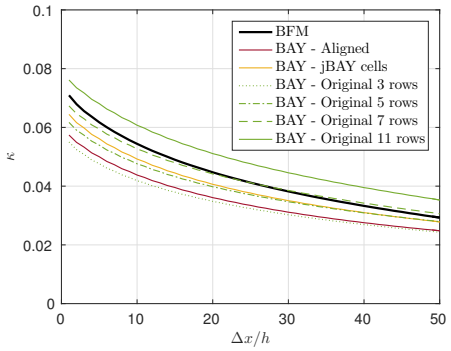

(a) Crossflow kinetic energy

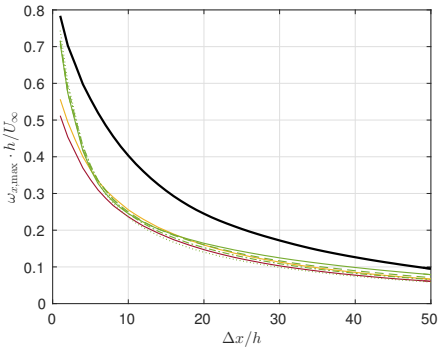

(b) Streamwise peak vorticity

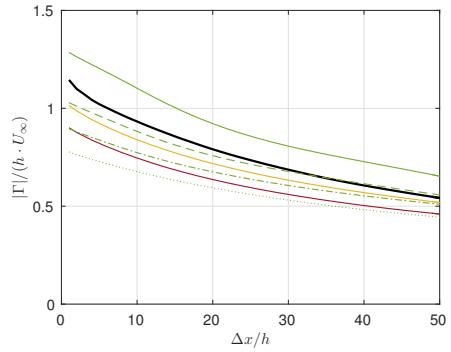

(c) Circulation

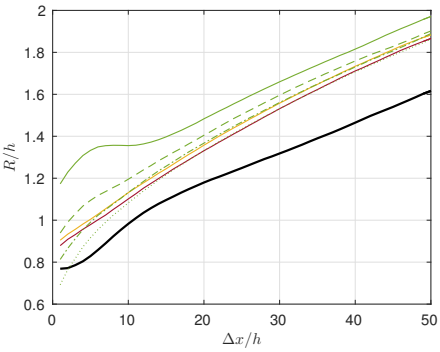

(d) Vortex core radius

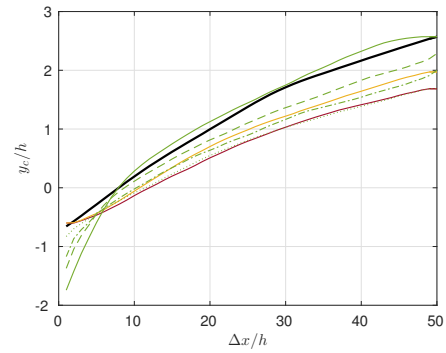

(e) Vortex center in crossflow direction

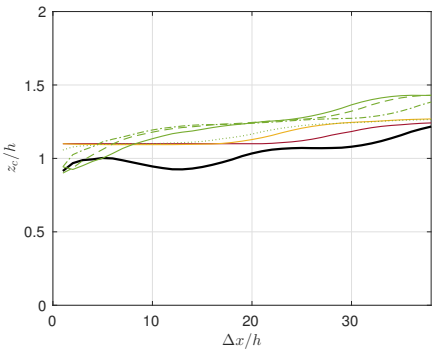

(f) Vortex center in wall-normal direction

Figure A.2: Non-dimensionalized vortex descriptors for the flat plate with a single submerged VG test case, using the medium mesh M2, comparing the effect of different cell-selection approaches.

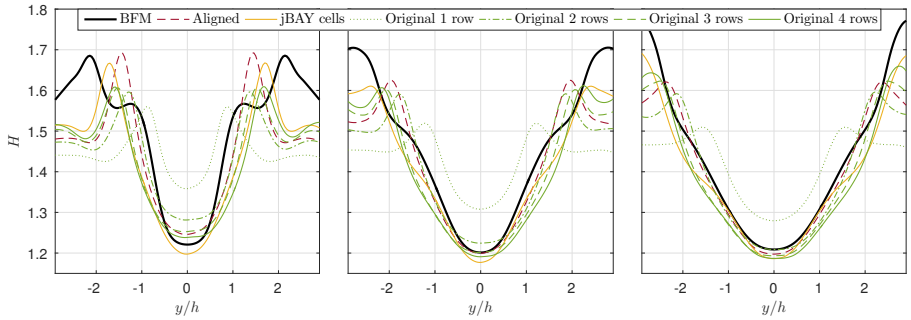

(a) Flat plate with counter-rotating VG pair, mesh M2.

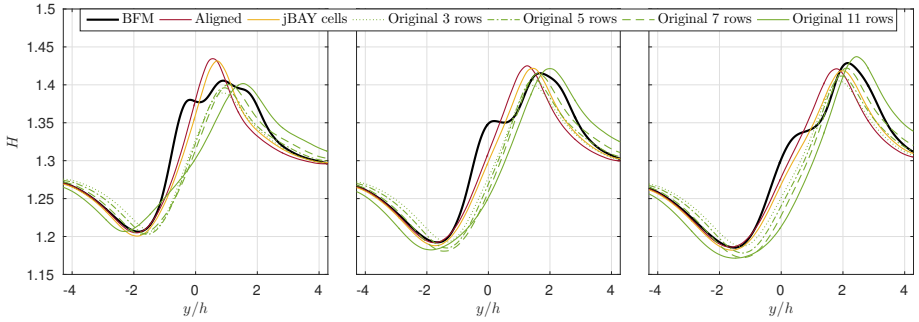

(b) Flat plate with single VG, mesh M2.

Figure A.3: Shape-factor profiles for different source-term regions, at $\Delta x = 5h$ (left), $\Delta x = 10h$ (middle) and $\Delta x = 15h$ (right) downstream of the VGs.

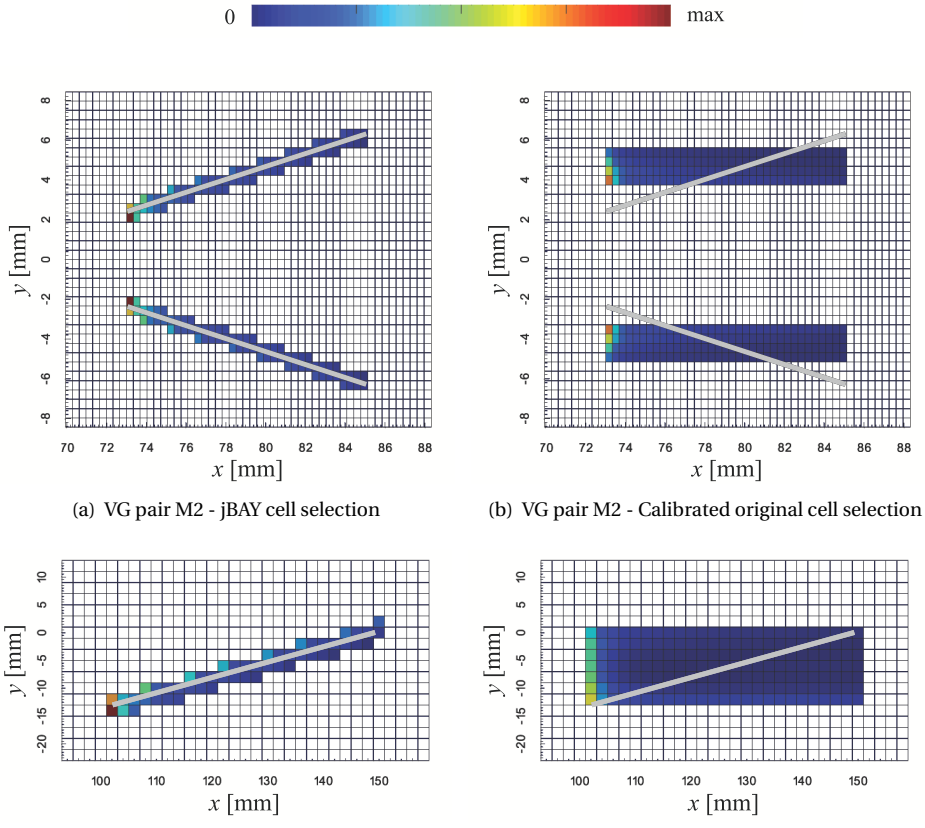

(a) VG pair M2 - jBAY cell selection

(b) VG pair M2 - Calibrated original cell selection

(c) Single VG - jBAY cell selection

(d) Single VG - Calibrated original cell selection

Figure A.4: Snapshots showing the domain Ω_{VG} at a cutting plane at $z = 0.6h$, colored according to source-term magnitude.

REFERENCES

[1] B. G. Allan, C.-s. Yao, and J. C. Lin. Numerical Simulations of Vortex Generator Vanes and Jets on a Flat Plate. (June):1–14, 2002.

[2] M. Amitay, D. R. Smith, V. Kibens, D. E. Parekh, and A. Glezer. Aerodynamic Flow Control over an Unconventional Airfoil Using Synthetic Jet Actuators. *AIAA J.*, 39(3):361–370, mar 2001.

[3] J. D. Anderson. *A History of Aerodynamics*. Cambridge University Press, 1 edition, 1997.

[4] J. D. Anderson. *Fundamentals of Aerodynamics*. McGraw-Hill Education, 4 edition, 2006.

[5] K. P. Angele and B. Muhammad-Klingmann. The effect of streamwise vortices on the turbulence structure of a separating boundary layer. *Eur. J. Mech. B/Fluids*, 24(5):539–554, 2005.

[6] P. Ashill, J. Fulker, and K. Hackett. Research at DERA on Sub Boundary Layer Vortex Generators (SBVGs). Technical Report January, 2001.

[7] P. Ashill, J. L. Fulker, and K. C. Hackett. Studies of flows induced by Sub Boundary layer Vortex Generators (SBVGs). *40th AIAA Aerosp. Sci. Meet. Exhib.*, (January):13, 2002.

[8] D. Baldacchino, M. Manolesos, C. Simao Ferreira, Á. González Salcedo, M. Aparicio, T. Chaviaropoulos, K. Diakakis, L. Florentie, N. R. García, G. Papadakis, N. N. Sørensen, N. Timmer, N. Troldborg, S. G. Voutsinas, and A. H. van Zuijlen. Experimental benchmark and code validation for airfoils equipped with passive vortex generators. *J. Phys. Conf. Ser.*, 753:022002, sep 2016.

[9] D. Baldacchino, D. Ragni, C. Simao Ferreira, and G. van Bussel. Towards integral boundary layer modelling of vane-type vortex generators. In *45th AIAA Fluid Dyn. Conf.*, Reston, Virginia, jun 2015. American Institute of Aeronautics and Astronautics.

[10] G. Batchelor. Batchelor, G. K. 1964 Axial flow in trailing line vortices. J. Fluid Mech. 20, 645658. *J. Fluid Mech.1*, 20:645–658, 1964.

[11] E. E. Bender, B. H. Anderson, and P. J. Yagle. Vortex Generator Modeling for Navier-Stokes Codes. In *3rd Jt. ASME/JSME Fluids Eng. Conf.*, pages 1–7, San Francisco, CA, 1999.

[12] M. J. Bhagwat and J. G. Leishman. Generalized viscous vortex model for application to free-vortex wake and aeroacoustic calculations. *Annu. forum proceedings-American helicopter Soc.*, 58(2):2042–2057, 2002.

[13] T. P. Bray. *A parametric study of vane and air-jet vortex generators*. Engineering doctorate (engd), Cranfield University, 1998.

[14] V. Brunet, C. Francois, E. Garnier, and M. Pruvost. Experimental and Numerical Investigations of Vortex Generators Effects. In *3rd AIAA Flow Control Conf.*, number June, pages 1–12, Reston, Virigina, jun 2006. American Institute of Aeronautics and Astronautics.

[15] C. Burg and T. Erwin. Application of Richardson extrapolation to the numerical solution of partial differential equations. *Numer. Methods Partial Differ. Equ.*, 25(4):810–832, jul 2009.

[16] A. Celic and E. H. Hirschel. Comparison of Eddy-Viscosity Turbulence Models in Flows with Adverse Pressure Gradient. *AIAA J.*, 44(10):2156–2169, 2006.

[17] T. Craft, B. Launder, and K. Suga. Development and application of a cubic eddy-viscosity model of turbulence. *Int. J. Heat Fluid Flow*, 17(2):108–115, apr 1996.

[18] A. Cutler and P. Bradshaw. Strong vortex/boundary layer interactions - Part I: Vortices High. *Exp. Fluids*, 14(5):321–332, apr 1993.

[19] A. Cutler and P. Bradshaw. Strong vortex/boundary layer interactions - Part II: Vortices Low. *Exp. Fluids*, 14(6):393–401, may 1993.

[20] J. C. Dudek. An Empirical Model for Vane-Type Vortex Generators in a Navier-Stokes Code. pages 1–24, 2005.

[21] J. C. Dudek. Modeling Vortex Generators in a Navier-Stokes Code. *AIAA J.*, 49(4):748–759, 2011.

[22] P. Durbin. Near-wall turbulence closure modeling without damping functions. *Theor. Comput. Fluid Dyn.*, 3(1):1–13, 1991.

[23] R. P. Dwight and J. Brezillon. Effect of Approximations of the Discrete Adjoint on Gradient-Based Optimization. *AIAA J.*, 44(12):3022–3031, 2006.

[24] U. Fernandez, C. M. Velte, P.-E. Réthoré, and N. N. Sørensen. Self-similarity and helical symmetry in vortex generator flow simulations. *Proc. Torque 2012, Sci. Mak. torque from Wind*, 2012.

[25] C. Ferreira, A. Gonzalez, D. Baldacchino, M. Aparicio, S. Gomez-Iradi, X. Munduate, A. Barlas, N. Garcia, N. N. Sorensen, N. Troldborg, G. N. Barakos, E. Jost, S. Knecht, T. Lutz, P. Chassapoyiannis, K. Diakakis, M. Manolesos, S. G. Voutsinas, J. Prospathopoulos, T. Gillebaart, L. Florentie, A. H. van Zuijlen, and M. Reijerkerk. AVATAR Task 3.2 : Development of aerodynamic codes for modelling of flow devices on aerofoils and rotors. Technical Report November, AVATAR project, FP7-ENERGY-2013-1/ n 608396, 2015.

[26] L. Florentie, A. H. van Zuijlen, S. J. Hulshoff, and H. Bijl. Effectiveness of Side Force Models for Flow Simulations Downstream of Vortex Generators. *AIAA J.*, 55(4):1373–1384, apr 2017.

[27] M. Gad-el Hak. *Flow Control: Passive, Active, and Reactive Flow Management*. Cambridge University Press, 2000.

[28] T. B. Gatski and T. Jongen. Nonlinear eddy viscosity and algebraic stress models for solving complex turbulent flows. *Prog. Aerosp. Sci.*, 36(8):655–682, 2000.

[29] S. Ghosh, J.-I. Choi, and J. R. Edwards. Numerical Simulations of Effects of Micro Vortex Generators Using Immersed-Boundary Methods. *AIAA J.*, 48(1):92–103, 2010.

[30] T. Gillen, M. Rybalko, and E. Loth. Vortex Generators for Diffuser of Axisymmetric Supersonic Inlets. In *5th Flow Control Conf.*, pages 1–18, Chicago, Illionois, jul 2010. American Institute of Aeronautics and Astronautics.

[31] G. Godard and M. Stanislas. Control of a decelerating boundary layer. Part 1: Optimization of passive vortex generators. *Aerosp. Sci. Technol.*, 10(3):181–191, apr 2006.

[32] D. A. Griffin. Investigation of Vortex Generators for Augmentation of Wind Turbine Power Performance. Technical Report NREL/SR-440-21399, National Renewable Energy Laboratory, 1996.

[33] M. Hansen, C. M. Velte, S. Øye, R. Hansen, N. N. Sørensen, J. Madsen, and R. Mikkelsen. Aerodynamically shaped vortex generators. *Wind Energy*, 17(April 2013):n/a–n/a, mar 2015.

[34] M. O. Hansen and C. Westergaard. Phenomenological Model of Vortex Generators. In B. Maribo Pedersen, editor, *9th Int. Energy Agency Symp. Aerodyn. Wind Turbines*, pages 1–7, 1995.

[35] J. K. Harvey and F. J. Perry. Flowfield produced by trailing vortices in the vicinity of the ground. *AIAA J.*, 9(8):1659–1660, aug 1971.

[36] J. Hoffman. Adaptive simulation of the subcritical flow past a sphere. *J. Fluid Mech.*, 568:77, 2006.

[37] D. D. Holm. Taylor's Hypothesis , Hamilton's Principle , and the LANS-a Model for Computing Turbulence. *Los Alamos Sci.*, (29):172–180, 2005.

[38] K. Ito and K. Kunisch. *Lagrange Multiplier Approach to Variational Problems and Applications*. Society for Industrial and Applied Mathematics, jan 2008.

[39] H. Jasak. *Error analysis and estimation for the finite volume method with applications to fluid flows*. Ph.d. thesis, Imperial College, London, 1996.

[40] J. Jeong and F. Hussain. On the identification of a vortex. *J. Fluid Mech.*, 285(-1):69, feb 1995.

[41] A. Jirasek. Vortex-Generator Model and Its Application to Flow Control. *J. Aircr.*, 42(6):1486–1491, 2005.

[42] J. Johansen, N. N. Sørensen, F. Zahle, S. Kang, I. Nikolaou, E. Politis, P. Chaviaropoulos, and J. Ekaterinaris. KNOW-BLADE Task-2 report ; Aerodynamic Accessories. Technical Report October, Risø-R-1482(EN), 2004.

[43] John D Anderson. Ludwig Prandtl ' s Boundary Layer. *Phys. Today*, (December):7, 2005.

[44] R. W. Johnson. *The Handbook of Fluid Dynamics*. Crc. Pr. Inc., 1998.

[45] J. Jones. The calculation of the paths of vortices from a system of vortex generators and a comparison with experiment. Technical report, Aeronautical Research Council, 1957.

[46] W. Jones and B. Launder. The prediction of laminarization with a two-equation model of turbulence. *Int. J. Heat Mass Transf.*, 15(2):301–314, feb 1972.

[47] G. Joubert, A. Le Pape, and S. Huberson. Numerical study of flow separation control over a OA209 Airfoil using Deployable Vortex Generator. *49th AIAA Aerosp. Sci. Meet. Incl. New Horizons Forum Aerosp. Expo.*, (January):1–20, 2011.

[48] M. Kerho and B. Kramer. Enhanced Airfoil Design Incorporating Boundary-Layer Mixing Devices. In *41st Aerosp. Sci. Meet. Exhib.*, Reston, Virigina, jan 2003. American Institute of Aeronautics and Astronautics.

[49] W. G. Kunik. Application of a computational model for vortex generators in subsonic internal flows. *AIAA/ASME/SAE/ASEE 22nd Jt. Propuls. Conf.*, pages 0–6, 1986.

[50] H. Lamb. *Hydrodynamics*. Cambridge University Press, Cambridg, 6th ed. edition, 1932.

[51] B. Launder, G. Reece, and W. Rodi. Progress in the Development of a Reynolds-Stress Turbulent Closure. *J. Fluid Mech.*, 68(3):537–566, 1975.

[52] B. Launder and B. Sharma. Application of the energy-dissipation model of turbulence to the calculation of flow near a spinning disc. *Lett. Heat Mass Transf.*, 1(2):131–137, nov 1974.

[53] M. Leschziner. *Statistical Turbulence Modelling for Fluid Dynamics - Demystified*. Imperial College Press, 2016.

[54] J. Liandrat, B. Aupoix, and J. Cousteix. Calculation of Longitudinal Vortices Imbedded in a Turbulent Boundary Layer. In *Turbul. Shear Flows 5*, pages 253–265. Springer Berlin Heidelberg, Berlin, Heidelberg, 1987.

[55] J. Lin, F. Howard, D. Bushnell, and G. Selby. Investigation of several passive and active methods for turbulent flow separation control. In *21st Fluid Dyn. Plasma Dyn. Lasers Conf.*, Reston, Virigina, jun 1990. American Institute of Aeronautics and Astronautics.

[56] J. C. Lin. Review of research on low-profile vortex generators to control boundary-layer separation. *Prog. Aerosp. Sci.*, 38(4-5):389–420, 2002.

[57] J. C. Lin, S. K. Robinson, R. J. McGhee, and W. O. Valarezo. Separation control on high-lift airfoils via micro-vortex generators. *J. Aircr.*, 31(6):1317–1323, nov 1994.

[58] J. Liu, U. Piomelli, and P. R. Spalart. Interaction between a spatially growing turbulent boundary layer and embedded streamwise vortices. *J. Fluid Mech.*, 326:151, nov 1996.

[59] O. Lögdberg, J. H. M. Fransson, and P. H. Alfredsson. Streamwise evolution of longitudinal vortices in a turbulent boundary layer. *J. Fluid Mech.*, 623:27, 2009.

[60] L. Maestrello and L. Ting. Analysis of active control by surface heating. *AIAA J.*, 23(7):1038–1045, jul 1985.

[61] M. Manolesos, G. Papadakis, and S. G. Voutsinas. Assessment of the CFD capabilities to predict aerodynamic flows in presence of VG arrays. *J. Phys. Conf. Ser.*, 524:012029, 2014.

[62] M. Manolesos and S. G. Voutsinas. Experimental investigation of the flow past passive vortex generators on an airfoil experiencing three-dimensional separation. *J. Wind Eng. Ind. Aerodyn.*, 142:130–148, 2015.

[63] N. May. A new vortex generator model for use in complex configuration CFD solvers. In *19th AIAA Appl. Aerodyn. Conf.*, Reston, Virigina, jun 2001. American Institute of Aeronautics and Astronautics.

[64] F. R. Menter. Zonal Two Equation k-w Turbulence Models for Aerodynamic Flows. In *24th Fluid Dyn. Conf.*, Orlando, Florida, 1993.

[65] R. Mittal and G. Iaccarino. Immersed Boundary Methods. *Annu. Rev. Fluid Mech.*, 37(1):239–261, jan 2005.

[66] D. J. Moreau and C. J. Doolan. Noise-Reduction Mechanism of a Flat-Plate Serrated Trailing Edge. *AIAA J.*, 51(10):2513–2522, 2013.

[67] A. S. Moreira Ribeiro. *Implementation and Analysis of an Empirical Vortex Generator Model in OpenFOAM*. M.sc. thesis, Delft University of Technology, 2017.

[68] A. Nemili and E. Ozkaya. Optimal Control of Unsteady Flows Using Discrete Adjoints. (June):1–14, 2011.

[69] G. Neretti. Active Flow Control by Using Plasma Actuators. In R. K. Agerwal, editor, *Recent Prog. Some Aircr. Technol.* InTech, sep 2016.

[70] I. G. Nikolaou, E. S. Politis, and P. K. Chaviaropoulos. Modelling the Flow Around Airfoils Equipped with Vortex Generators Using a Modified 2D Navier-Stokes Solver. *J. Sol. Energy Eng.*, 127(2):223, 2005.

[71] C. Nita, S. Vandewalle, and J. Meyers. On the efficiency of gradient based optimization algorithms for DNS-based optimal control in a turbulent channel flow. *Comput. Fluids*, 125:11–24, 2016.

[72] B. R. Noack, M. Morzyński, and G. Tadmor, editors. *Reduced-Order Modelling for Flow Control*, volume 528 of *CISM International Centre for Mechanical Sciences*. Springer Vienna, Vienna, 2011.

[73] J. Nocedal and S. J. Wright. *Numerical Optimization*. 2 edition, 2006.

[74] C. Oseen. Uber Wirbelbewegung in Einer Reiben- den Flussigkeit. *Ark. J. Mat. Astrom. Fys.*, 7:14–21, 1912.

[75] C. Othmer. A continuous adjoint formulation for the computation of topological and surface sensitivities of ducted flows. *Int. J. Numer. Methods Fluids*, 58(8):861–877, nov 2008.

[76] S. Patankar. The SIMPLE Algorithm. In *Numer. heat Transf. fluid flow*, chapter 6, pages 126–131. Hemisphere Publishing Corporation, 1980.

[77] W. R. Pauley and J. K. Eaton. Experimental study of the development of longitudinal vortex pairs embedded in a turbulent boundary layer. *AIAA J.*, 26(7):816–823, jul 1988.

[78] H. Pearcey. *Introduction To Shock-Induced Separation and Its Prevention By Design and Boundary Layer Control*. PERGAMON PRESS LTD, 1961.

[79] D. Poole, R. Bevan, C. Allen, and T. Rendall. An Aerodynamic Model for Vane-Type Vortex Generators. *34th AIAA Appl. Aerodyn. Conf.*, (June):1–18, 2016.

[80] S. B. Pope. *Turbulent Flows*. Cambridge University Press, 2000.

[81] L. Prandtl. Über Flüssigkeitsbewegung bei sehr kleiner Reibung. In *Verhandlungen des III Int. Math. Heidelberg, 1904*, pages 484–491, 1905.

[82] W. Rankine. *Manual of Applied Mechanics*. C. Griffen Co., London, 1858.

[83] D. Rao and T. Kariya. Boundary-layer submerged vortex generators for separation control - An exploratory study. In *1st Natl. Fluid Dyn. Conf.*, volume 3546, page 1988, Reston, Virigina, jul 1988. American Institute of Aeronautics and Astronautics.

[84] W. Rodi. A new algebraic relation for calculating the Reynolds stresses. *Gesellschaft Angew. Math. und Mech. Work. Paris Fr.*, 56, 1976.

[85] C. Roy. Review of Discretization Error Estimators in Scientific Computing. In *48th AIAA Aerosp. Sci. Meet. Incl. New Horizons Forum Aerosp. Expo.*, Reston, Virigina, jan 2010. American Institute of Aeronautics and Astronautics.

[86] G. Schubauer and W. Spangenberg. Forced mixing in boundary layers. *J. Fluid Mech.*, 8:10–32, 1960.

[87] V. Schulz and I. Gherman. One-Shot Methods for Aerodynamic Shape Optimization. In *Notes Numer. Fluid Mech. Multidiscip. Des.*, pages 207–220. Springer, Berlin, Heidelberg, 2009.

[88] I. M. M. A. Shabaka, R. D. Mehta, and P. Bradshaw. Longitudinal vortices imbedded in turbulent boundary layers. Part 1. Single vortex. *J. Fluid Mech.*, 155(-1):37, jun 1985.

[89] H. Shan, L. Jiang, C. Liu, M. Love, and B. Maines. Numerical study of passive and active flow separation control over a NACA0012 airfoil. *Comput. Fluids*, 37(8):975–992, 2008.

[90] P. E. Smirnov and F. R. Menter. Sensitization of the SST Turbulence Model to Rotation and Curvature by Applying the SpalartShur Correction Term. *J. Turbomach.*, 131(4):041010, 2009.

[91] F. T. Smith. Theoretical prediction and design for vortex generators in turbulent boundary layers. *J. Fluid Mech.*, 270:91, 1994.

[92] P. Spalart and S. Allmaras. A one-equation turbulence model for aerodynamic flows. In *30th Aerosp. Sci. Meet. Exhib.*, Reston, Virigina, jan 1992. American Institute of Aeronautics and Astronautics.

[93] P. Spalart and M. Shur. On the sensitization of turbulence models to rotation and curvature. *Aerosp. Sci. Technol.*, 1(5):297–302, jul 1997.

[94] P. Spalart, M. L. Shur, M. K. Strelets, and A. K. Travin. Direct Simulation and RANS Modelling of a Vortex Generator Flow. *Flow, Turbul. Combust.*, 95(2-3):335–350, 2015.

[95] C. G. Speziale. On nonlinear K-l and K -ϵ models of turbulence. *J. Fluid Mech.*, 178(1):459, may 1987.

[96] C. G. Speziale, S. Sarkar, and T. B. Gatski. Modelling the pressurestrain correlation of turbulence: an invariant dynamical systems approach. *J. Fluid Mech.*, 227:245–272, jun 1991.

[97] H. Squire. The Growth of a Vortex in Turbulent Flow. *Aeronaut. Q.*, 16(3):302–306, 1965.

[98] D. N. Srinath and S. Mittal. An adjoint method for shape optimization in unsteady viscous flows. *J. Comput. Phys.*, 229(6):1994–2008, 2010.

[99] T. Steihaug. The Conjugate Gradient Method and Trust Regions in Large Scale Optimization. *SIAM J. Numer. Anal.*, 20(3):626–637, jun 1983.

[100] F. V. Stillfried. *Computational fluid-dynamics investigations of vortex generators for flow-separation control.* PhD thesis, Royal Institute of Technology, Stockholm, 2012.

[101] F. V. Stillfried, S. Wallin, and A. V. Johansson. An improved passive vortex generator model for flow separation control. *5th Flow Control Conf.*, (July):1–14, 2010.

[102] H. Taylor. Application of Vortex Generator Mixing Principles to Diffusers. Technical report, United Aircraft Corporation, East Hartford, Connecticut, 1948.

[103] O. Törnblom and A. V. Johansson. A Reynolds stress closure description of separation control with vortex generators in a plane asymmetric diffuser. *Phys. Fluids*, 19(11), 2007.

[104] N. Troldborg, F. Zahle, and N. N. Sørensen. Simulation of a MW rotor equipped with vortex generators using CFD and an actuator shape model. *53rd AIAA Aerosp. Sci. Meet.*, (January):1–10, 2015.

[105] C. P. van Dam, B. J. Holmes, and C. Pitts. Effect of Winglets on Performance and Handling Qualities of General Aviation Aircraft. *J. Aircr.*, 18(7):587–591, jul 1981.

[106] C. Velte, M. Hansen, and D. Cavar. Flow analysis of vortex generators on wing sections by stereoscopic particle image velocimetry measurements. *Environ. Res. Lett.*, 3:015006, 2008.

[107] C. M. Velte, C. Braud, S. Coudert, and J.-m. Foucaut. Vortex Generator Induced Flow in a High Re Boundary Layer. *Sci. Mak. Torque from Wind 2012*, (Umr 8107), 2012.

[108] C. M. Velte, M. O. Hansen, and V. L. Okulov. Helical structure of longitudinal vortices embedded in turbulent wall-bounded flow. *J. Fluid Mech.*, 619:167, 2009.

[109] C. M. Velte, V. L. Okulov, and I. V. Naumov. Regimes of flow past a vortex generator. *Tech. Phys. Lett.*, 38(4):379–382, 2012.

[110] F. von Stillfried, S. Wallin, and A. V. Johansson. Vortex-Generator Models for Zero- and Adverse-Pressure-Gradient Flows. *AIAA J.*, 50(4):855–866, 2012.

[111] K. Waithe. Source Term Model for Vortex Generator Vanes in a Navier-Stokes Computer Code. In *42nd AIAA Aerosp. Sci. Meet. Exhib.*, pages 1–11, Reston, Virigina, jan 2004. American Institute of Aeronautics and Astronautics.

[112] F. Wallin and L.-E. Eriksson. A Tuning-free Body-Force Vortex Generator Model. In

44th AIAA Aerosp. Sci. Meet. Exhib., pages 1–12, Reston, Virigina, jan 2006. American Institute of Aeronautics and Astronautics.

[113] B. J. Wendt. The Modelling of Symmetric Vortex Generators Airfoil Vortex Generators. *Aerosp. Sci. Meet. Exhib. 34th, Reno, NV*, pages 15–18, 1996.

[114] B. J. Wendt. Initial Circulation and Peak Vorticity Behavior of Vortices Shed from Airfoil Vortex Generators. Technical Report August, NASA, 2001.

[115] B. J. Wendt. Parametric Study of Vortices Shed from Airfoil Vortex Generators. *AIAA J.*, 42(11):2185–2195, nov 2004.

[116] R. V. Westphal, W. R. Pauley, and J. K. Eaton. Interaction between a vortex and a turbulent boundary layer. Part 1: Mean flow evolution and turbulence properties. (January), 1987.

[117] E. Wik and S. Shaw. Numerical Simulation of Micro Vortex Generators. In *2nd AIAA Flow Control Conf.*, Reston, Virigina, jun 2004. American Institute of Aeronautics and Astronautics.

[118] D. C. Wilcox. Reassessment of the scale-determining equation for advanced turbulence models. *AIAA J.*, 26(11):1299–1310, nov 1988.

[119] C. Yao, J. Lin, and B. Allan. Flow-field measurement of device-induced embedded streamwise vortex on a flat plate. In *NASA STI/Recon Tech. Rep. ...*, number June, page 16, 2002.

[120] D. You, M. Wang, R. Mittal, and P. Moin. Large-Eddy Simulations of Longitudinal Vortices Embedded in a Turbulent Boundary Layer. *AIAA J.*, 44(12):3032–3039, 2006.

[121] A. S. Zymaris, D. I. Papadimitriou, K. C. Giannakoglou, and C. Othmer. Continuous adjoint approach to the Spalart-Allmaras turbulence model for incompressible flows. *Comput. Fluids*, 38(8):1528–1538, 2009.

ACKNOWLEDGEMENTS

Almost 5 years after getting excited to start my Ph.D. research, it is now time to get excited about finishing it and starting a new adventure. Looking back on those years, I can honestly say that what people have been telling me is true: it was definitely a path with many ups and downs, but also, I never regretted starting it! All along my way I found people supporting and encouraging me. So now that I am writing these last words of this book, feeling proud of my work and already forgetting the challenges and frustrations along the way, I would like to express my gratitude to all of you.

To my supervisors from the start, Hester Bijl and Alexander van Zuijlen, thank you for believing in me and for giving me the opportunity to perform this research entirely to my own ideas. Hester, your contagious enthusiasm and optimism have been heartwarming, and Sander, thank you for being there to help me whenever I asked.

Finishing this Ph.D. would not have been possible without the help of my copromotor. Steve, even before being an official member of the team you managed to steer me into the right direction by some casual, yet straight to the point, comments. With just one question during the department's presentation days you fueled my inspiration for almost half my research. And you did the same a year later for the other half. I am extremely grateful that you believed in me and that you took on the role as my copromotor at a time when I felt I was stuck. Your eye for detail has been key to raising the quality of my work. Thank you for your kindness and for our inspiring and motivating discussions!

I also want to thank Daniel Baldacchino and Carlos Simao Ferreira for our pleasant collaboration on the AVATAR project. Daniel, thank you also a lot for sharing your experimental data with me, they have been of great value to this work.

Over the past years I have had the pleasure of sharing an office with a large group of great fellow Ph.D. students. Thijs, Rogier, Wouter, David, Iliass, Koen, Jan, Paul, Jacopo, Mirja, Theo, Giuseppe, Rakesh, Shaafi, and many others, thank you for the good times during lunch, breaks and at conferences! Moreover, I am very grateful to Thijs for helping me find my way in the OpenFOAM maze. And of course I cannot forget Colette, who solves any problem related to vague procedures before you can even ask, thank you!

Another group of colleagues that cannot go unmentioned are the people of our faculty's student and education department. I am very grateful that I had the opportunity to work with you aside of my Ph.D. project. Thank you for the great atmosphere and for your honest interest and support! Especially Sander, thank you for always being there for me, I owe you a lot! These last two years you have been a constant source of support and tranquility, calming me down when I was stressed but also putting me to work when I was pushing forward work on my dissertation. You have been a great colleague and friend. I will miss working with you, but let's hope that moving away from Delft does not mean having to miss our chats.

And as 4 heroes once sang, I get by with a little help from my friends. Indeed, what would I be without the love and support from my friends and family? Rui, Eveline,

Inge, Nanda, Emma, the Stomwijzer, Victor, thank you for the good times, the chats, the drinks, the laughs. We should definitely increase their frequency! Vake, moeke, grootmoe, grootva, Pieter, Ellen, Pär, it is heartwarming to have such a loving and caring family like you! I will always be there for you, just as I know that you are for me.

Finally, to Mirko, my perfect boyfriend, thank you for bringing an endless stream of happiness to my life! I am who I am because of you. You inspire me to be ambitious and to chase my dreams, while at the same time making our home a relaxed place where I can always refuel. Everything feels easier and better with you at my side. Finishing this dissertation is a milestone which I would never have been able to achieve without your love, help and support. I love you and I look forward to the following adventures we will embark on together!

LIST OF PUBLICATIONS

- **L. Florentie**, S.J. Hulshoff, and A.H. van Zuijlen. *Adjoint-Based Optimization of a Source-Term Representation of Vortex Generators.* Computers and Fluids, 162: 139-151, 2018.
- **L. Florentie**, A.H. van Zuijlen, S.J. Hulshoff, and H. Bijl. *Effectiveness of Side Force Models for Flow Simulations Downstream of Vortex Generators.* AIAA Journal, 55(4): 1373-1384, 2017.
- M. Manolesos, N.N. Sørensen, N. Troldberg, **L. Florentie**, G. Papadakis, and S.G. Voutsinas. *Computing the flow past Vortex Generators: Comparison between RANS Simulations and Experiments.* Journal of Physics: Conference Series, 753: 022014, 2016.
- D. Baldacchino, M. Manolesos, C.J. Simão Ferreira, A. González Salcedo, M. Aparicio, T. Chaviaropoulos, K. Diakakis, **L. Florentie**, N.R. García, G. Papadakis, N.N. Sørensen, N. Timmer, N. Troldborg, S.G. Voutsinas, and A.H. van Zuijlen. *Experimental benchmark and code validation for airfoils equipped with passive vortex generators.* Journal of Physics: Conference Series, 753: 022002, 2016.
- **L. Florentie**, D.S. Blom, T.P. Scholcz, A.H. van Zuijlen, and H. Bijl. *Analysis of Space Mapping Algorithms for Application to Partitioned Fluid-Structure Interaction Problems.* International Journal for Numerical Methods in Engineering, 105(2): 138-160, 2016.
- **L. Florentie**, A.H. van Zuijlen, and H. Bijl. *Towards a multi-fidelity approach for CFD simulations of vortex generator arrays.* 11th World Congress on Computational Mechanics, WCCM 2014, 5th European Conference on Computational Mechanics, ECCM 2014 and 6th European Conference on Computational Fluid Dynamics, ECFD 2014, 7187-7198, 2014.

CURRICULUM VITÆ

Liesbeth Florentie was born on August 30, 1988 in Bonheiden, Belgium. Her entire childhood she lived in Haacht, where she attended the Don Bosco secondary school from 2000 to 2006.

Following her passion for mathematics and space exploration, Liesbeth moved to Delft to study Aerospace Engineering at Delft University of Technology in September 2006. She obtained her Bachelor of Science degree cum laude in 2009. By that time Liesbeth had become intrigued by the beautiful complexity of fluid dynamics, motivating her to combine a master programme in aerodynamics with an honours programme in mathematics. After a research internship at Cardiff Univerisity, Liesbeth completed her Master of Science in Aerospace Engineering at Delft University of Technology in 2012, cum laude, with a thesis on multi-fidelity coupling algorithms for fluid-structure-interaction simulations.

After graduation, Liesbeth spent one year working as an engineering consultant for Dynaflow Research Group. She returned to Delft University of Technology in 2013 to start her Ph.D. research on simulation methods for vortex-generator effects in wall-bounded flows. She performed this research as part of the European project AVATAR, which had as goal the investigation of simulation methods for application to a next generation of large wind turbines. From 2016 on, Liesbeth combined her Ph.D. research with a part-time job at the faculty's student and education office where she worked on getting a selection procedure for incoming bachelor students on track.

With the completion of this dissertation comes an end to Liesbeth's time in Delft. In April 2018 Liesbeth will start as a researcher at Wageningen University, hoping to contribute to a better understanding of (human-produced) greenhouse-gas flows in the atmosphere.